University of Illinois at Urbana-Champaign

ACRC

Air Conditioning and Refrigeration Center A National Science Foundation/University Cooperative Research Center

Vortex Generation as an Air-Side Enhancement Method for Frosted-Surface Heat Exchanger Performance

A. D. Sommers and A. M. Jacobi

ACRC TR-219 December 2003

For additional information:

Air Conditioning and Refrigeration Center
University of Illinois
Mechanical & Industrial Engineering Dept.
1206 West Green Street
Urbana, IL 61801

(217) 333-3115

Prepared as part of ACRC Project #121
A Study of the Application of Vortex Generators to Enhance the Air-Side Thermal Performance of Heat Exchangers
A. M. Jacobi, Principal Investigator

The Air Conditioning and Refrigeration Center was founded in 1988 with a grant from the estate of Richard W. Kritzer, the founder of Peerless of America Inc. A State of Illinois Technology Challenge Grant helped build the laboratory facilities. The ACRC receives continuing support from the Richard W. Kritzer Endowment and the National Science Foundation. The following organizations have also become sponsors of the Center.

Alcan Aluminum Corporation
Amana Refrigeration, Inc.
Arçelik A. S.
Carrier Corporation
Copeland Corporation
Daikin Industries, Ltd.
Delphi Harrison Thermal Systems
Embraco S. A.
General Motors Corporation
Hill PHOENIX
Honeywell, Inc.
Hydro Aluminum Adrian, Inc.
Ingersoll-Rand Company
Lennox International, Inc.
LG Electronics, Inc.
Modine Manufacturing Co.
Parker Hannifin Corporation
Peerless of America, Inc.
Samsung Electronics Co., Ltd.
Sanyo Electric Co., Ltd.
Tecumseh Products Company
The Trane Company
Visteon Automotive Systems
Wieland-Werke, AG
Wolverine Tube, Inc.

For additional information:

Air Conditioning & Refrigeration Center
Mechanical & Industrial Engineering Dept.
University of Illinois
1206 West Green Street
Urbana, IL 61801

217 333 3115

Abstract

Longitudinal vortex generation is a technique for enhancing heat transfer and can be accomplished by placing small flow manipulators on the fin surface of a heat exchanger. This technique is of particular benefit in plain-fin-and-tube heat exchangers where the fin pitch is large (5-10mm) and the air-side convective coefficient is small.

In this study, a single row of delta-wing vortex generators is applied to a refrigerator evaporator with a fin spacing of 8.5 mm both along the leading edge and at a location halfway along the flow length for a total of 108 vortex generators. Heat transfer and pressure drop performance are measured before and after to determine the effectiveness of the vortex generator under frosting conditions. Under lightly frosted conditions, reductions in air-side thermal resistance of 3.5% to 22.8% are achieved for face velocities of 0.45 m/s to 1.1 m/s. This heat transfer enhancement monotonically increases with air velocity and results in a small pressure drop penalty that is incommensurate with the achieved enhancement. Maximum frost accumulation in the enhanced heat exchanger is also examined for a single row of leading edge delta wings. Under these conditions, a reduction in the air-side thermal resistance is observed that falls within the uncertainty of the experiment.

Finally, a second, denser array of 324 vortex generators is examined for the same evaporator where the delta wings are attached along four rows in an alternating single row, double row arrangement at core depth intervals of 50.8 mm (2 in). For Reynolds numbers between 500 and 1200, a reduction of 35.0% to 42.1% is observed in the air-side thermal resistance. Correspondingly, the heat transfer coefficient is observed to lie between 26-51 W/m^2-K for the enhanced evaporator and between 16-26 W/m^2-K for the baseline evaporator. Two different performance evaluation criteria are calculated and both show that the enhanced evaporator outperforms the baseline specimen for Reynolds numbers greater than approximately 700-750. Tests conducted under maximum frosting conditions reveal a diminished but statistically significant heat transfer enhancement.

Table of Contents

List of Figures

Page

List of Tables

Page

Nomenclature

Roman Symbols:		**Units:**
a	finned length of the evaporator tubes	*m*
A	heat transfer surface area	m^2
A_{min}	minimum free flow area between fins	m^2
b	total width of the evaporator; delta-wing span	*m*
c	test section height; delta-wing chord	*m*
C	heat-rate capacity, $\dot{m}\, c_p$	*W/K*
c_p	constant pressure specific heat	*J/kgK*
D_h	hydraulic diameter	*m*
f	Fanning friction factor, $((2\cdot\Delta P_{core}\cdot\rho_a)/G^2)(A_{min}/A_{tot})$	-
F_p	fin pitch, channel height	*m*
G	mass velocity, $G = \dot{m}_a/A_{min,}$	kg/m^2s
h	heat transfer coefficient	W/m^2K
h	total enthalpy	*J/kg*
h_{sg}	ablimation energy of the frost layer	*J/kg*
j	Colburn *j*-factor, $Nu/Re_{Dh}Pr^{1/3}$	-
k	thermal conductivity	*W/mK*
L	tube length	*m*
Le	Lewis number thermal/mass diffusivity	-
$\dot{m}$	mass flow rate	*kg/s*
$\dot{m}_f$	frost deposition rate	*kg/s*
mf	water vapor mass fraction	*kg/kg*
N	number of tubes, fins, etc.	-
NTU	number of transfer units, UA_{tot}/C_{min}	-
Nu_R	tube-side Nusselt number, h_rD_o/k_r	-
Pr	Prandtl number, $c_p\,\mu\,/k$	-
P_{core}	air-side core pressure measurement	*Pa*
Q	rate of heat transfer	*W*
r_o	outside tube radius	*m*
R_{as}	air-side thermal resistance	*K/W*
R_C	ratio of minimum to maximum heat rate capacity, $R_C = C_a/C_r$	-
Re_{dh}	air-side Reynolds number, VD_h/ν	-
RH	relative humidity	-
t	fin thickness; time	*m; sec*
T	temperature	*K*
UA_{tot}	overall thermal conductance	*W/K*
U	overall heat transfer coefficient	W/m^2K
V	heat exchanger core volume; velocity	m^3; *m/s*
V_{max}	air velocity based on minimum free-flow area, $V_{max} = \dot{m}_a/\rho_a A_{min}$	*m/s*
W_a	uncertainty in variable a	-
x	streamwise coordinate direction	*m*

y	coordinate direction normal to the bottom surface of the test section	*m*
z	spanwise coordinate direction	*m*

Greek Symbols:		**Units:**
α	angle of attack for the delta-wing	°
b	diameter ratio for the orifice plate	-
Δ	change in quantity	-
δ	frost thickness	*m*
e	heat exchanger effectiveness, q/q_{max}	-
h	fin efficiency	-
n	kinematic viscosity	m^2/s
Θ	modified volume-goodness factor, $Q_{air}/(V_{core} \cdot \Delta h_{lm})$	$kg/m^3 s$
Λ	delta-wing aspect ratio, 2b/c	-
r	density	kg/m^3
w	humidity ratio	*kg/kg*

Subscripts:

a	air
a1,a2	air stream in partition 1 or partition 2
ai, ao	air at the exchanger inlet and outlet
alum	aluminum
cond	conduction thermal resistance
conv	convection thermal resistance
contact	tube-to-fin contact resistance
f	frost
fin	of the fin
i	inlet or inner
lm	log-mean difference
max	maximum
min	minimum
o	outlet or outer
r	refrigerant
ri, ro	tube-side flow at the inlet and outlet of the evaporator
rm	for the coolant between the partitions
s	frost surface
t	tube
ti	inner tube surface
to	outer tube surface
tot	total
sat	saturated condition
VG	vortex generator
w	wall
∞	free stream

Chapter 1- Introduction

1.1 Background

In many refrigeration applications, the evaporator is a plain-fin-and-tube heat exchanger, with a fin spacing of 5-10 mm. These heat exchangers are widely used because they are reliable, inexpensive, and relatively tolerant to frost accumulation. Unfortunately, this heat exchanger geometry does not provide a very high air-side heat transfer coefficient. Enhancing the air-side thermal-hydraulic performance of plain-fin-and-tube heat exchangers can lead to smaller, lighter, and more energy efficient refrigeration systems. In this research we examine the use of vortex generators as an air-side enhancement technique for refrigeration evaporators.

In essence, streamwise vortex enhancement works by imparting a secondary flow to the mainstream, which brings a highly rotational flow in contact with the boundary layer on the surface as shown in Figure 1.1. The downwash region of the vortex thins the thermal boundary layer; whereas, the upwash region thickens it. These surface-normal inflow and outflow regions occupy nearly the same heat transfer surface area, but the response of the convective heat transfer coefficient is nonlinear and thus allows the heat transfer enhancement associated with the inflow to exceed the heat transfer degradation of the outflow. In this way, vortex enhancement is qualitatively similar to the effect of blowing and suction on heat transfer from a flat plate. This enhancement, however, comes at the cost of an increased pressure drop, due to the shear forces along the fin surface and the form drag of the vortex generators. Because of the linear relationship between shear stress and the velocity gradient, the inflow and the outflow associated with streamwise vortex generation produce nearly equal regions of increased and decreased shear. As a result, the drag on the vortex generator is the main contributor to the pressure drop penalty and is rather small for a plain fin-and-tube heat exchanger where the major source of drag is the tubes.

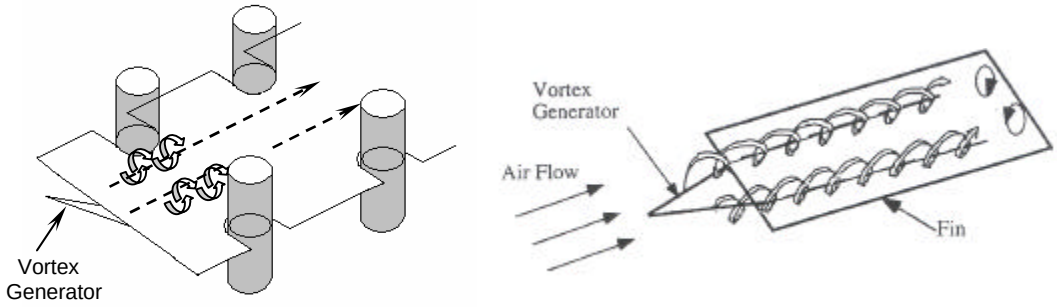

Figure 1.1- Schematic of a vortex generator showing the surface-normal inflow and outflow regions on a fin

The major focus of this research is the impact of accumulating frost on the effectiveness of the vortex generator where the deposition of a frost layer can change the geometry of the vortex generator and affect the flow of the air stream as shown below in Figures 1.2 and 1.3. The major difficulty in studying frost growth on a heat exchanger is the sensitivity of frost growth to environmental parameters (i.e. moisture content, interfacial substrate temperature, surface material, surface roughness, etc.). On an evaporator where the tube wall temperature is continuously changing over the length of the exchanger, it is a real challenge to predict frost properties such as density and thermal conductivity based on interfacial temperature alone. Furthermore, in most evaporators, coolant flow is partitioned into parallel flow and counter flow sections relative to the air stream. This fact, coupled with the

observation that frost deposition diminishes with increasing core depth due to a natural reduction in the enthalpy driving potential, makes the use of standard correlations found in the literature very difficult.

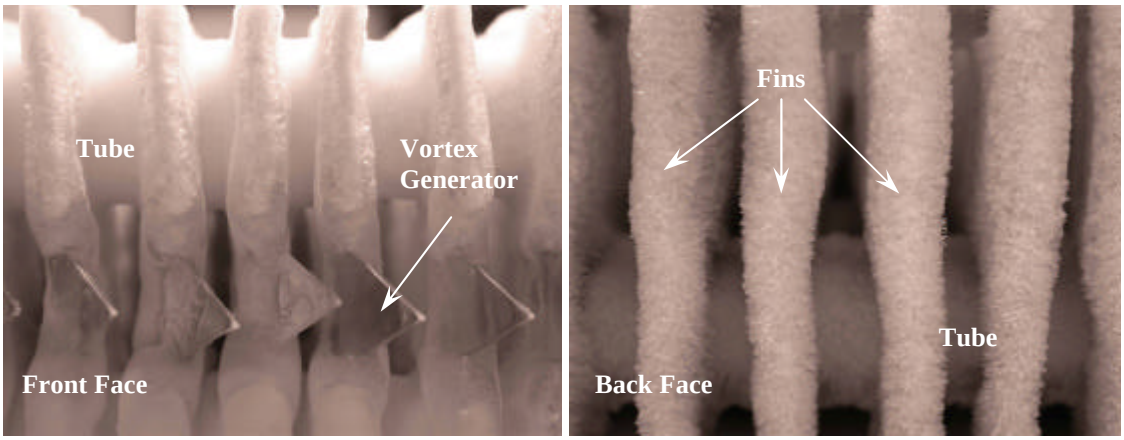

Figure 1.2- Frost deposition on a heat exchanger is known to increase the core pressure drop and degrade thermal performance.

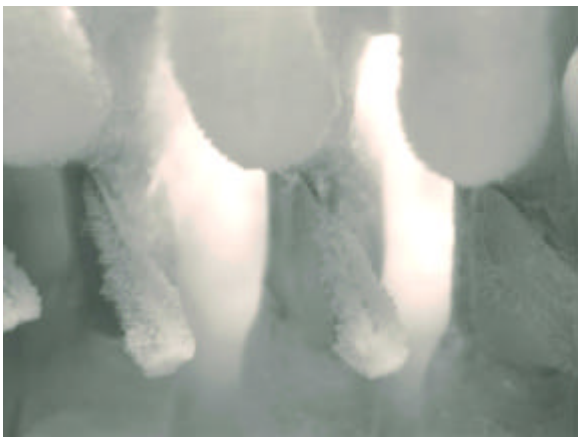

Figure 1.3- Frost growing on a vortex generator can affect the flow geometry.

1.2 Literature Review

1.2.1 Vortex Generator Studies

Several individuals have shown the promise of vortex generation as a means of heat transfer augmentation for flat-plate flows, channel flows, and channel flows with tubes. For example, using unsteady liquid crystal thermography (LCT) to study delta wings in pure channel flow, Fiebig *et al*. [1991] reported average heat transfer enhancements exceeding 50% with an accompanying 45% increase in the drag coefficient. Using naphthalene sublimation in channel flow for 400< Re <2000, Gentry and Jacobi [1998] found similar enhancements of 20–50% and pressure drop penalties of 50-110% for the delta wing. In a computational study by Brockmeier *et al*. [1993], the thermal-hydraulic performance of delta-wing vortex generators was found to be superior to conventional heat enhancement methods including plain fins, offset strips, and louvered fins. Experiments conducted on channel flows with tubes have also produced promising results. Fiebig *et al*. [1994] investigated heat exchangers with 3 tube rows and a delta-winglet pair downstream of each tube. For an inline arrangement, they reported average increases in heat transfer of 55-65% with a pressure penalty of only 20-45%.

Some of the earliest known testing of flow manipulators was performed by Schubauer and Spangenberg in 1959. They studied the effect of forced mixing on boundary layer development in a wind tunnel with slatted wall sections that could be adjusted to generate various back pressures. By using dust injection to demarcate the location of flow separation, they concluded that the general effect of the flow manipulators was equivalent to a decrease in the adverse pressure gradient. Various types of flow mixers were tested, one of which resembled a delta wing that was appropriately identified as a "triangular plow." The E-3 triangular plow, which had an aspect ratio, $\Lambda = 1.33$ and an angle of attack, $\alpha = 19.5°$, was observed to increase the pressure-recovery coefficient at separation from 0.50 to 0.75 as well as extend the point of separation from 4.83 ft to 7.92 ft. The price of this accomplishment was a 78% increase in the momentum thickness.

Critical Reynolds Number

Fiebig [1998] in a technical summary of the literature concluded that for a single vortex generator, heat transfer enhancement increases with the angle of attack reaching a maximum around 45°. He also argued that heat transfer enhancement increases with vortex generator area and decreases with the transverse spacing of the generators. Local heat transfer enhancements of 100% and overall enhancements of 50% were possible, which equates to more than 100 times the area of the vortex generator. These conclusions were primarily deduced from work conducted using delta winglet pairs and rectangular winglet pairs. Fiebig [1998] also reported that vortex generators inserted into channel flow might reduce the critical Reynolds number necessary for onset of turbulence to as low as 350.

Performance Evaluation Criterion Results

In a more recent experimental study of the application of delta winglets to three-row tube bundles, K.M. Kwak *et al*. [2002] observed heat transfer improvements of 10-25% with a corresponding pressure loss increase of 20-35%. Using performance evaluation criterion (PEC) analysis, they also reported that performance enhancements were higher in the inline arrangement than the staggered arrangement due to the large pressure drop penalty associated with the staggered arrangement. These results spanned a range of Reynolds numbers from 300 to 2700. It should be noted that Kwak *et al*. [2002] defined the characteristic length used in the Reynolds number as twice the channel height- not the hydraulic diameter.

Optimal Delta-Wing Dimensions

Very few studies have been conducted to optimize the dimensions and construction of the vortex generator. Gentry and Jacobi [1998] performed a parametric study of a single delta-wing vortex generator under developing channel flow using naphthalene sublimation by examining such effects as aspect ratio, angle of attack, and Reynolds numbers common to the HVAC&R industry (i.e. Re_{dh} = 400-2000). In this study, Gentry varied the aspect ratio, Λ, between 0.5 and 2.0 while fixing the angle of attack, α, at 15°, 35°, or 55°. At low Re_{dh}, which is of particular interest for domestic refrigeration research, the Sherwood enhancement ratio was relatively small over the majority of the parameter space. The peak value of approximately 1.25 occurred for $\Lambda = 2.0$ and $\alpha = 55°$. In fact, Gentry found the greatest enhancement occurred with $\Lambda = 2.0$ and $\alpha = 55°$ for all three Re_{dh} in the channel flow.

Effect of Vortex Generator Stamping

Biswas and Chattopadhyay [1992] presented a numerical study on the effect of a punched/stamped hole beneath the delta wing on the spanwise average Nusselt number, friction factor, and vortex strength. In their study,

they assumed perfectly aligned holes and imposed spacewise-periodic boundary conditions at the location of the punched holes. Grid refinement was performed to ensure nearly grid-independent results. For the case of stamping, fluid entrainment through the upper hole was observed, and fluid was lost through the hole underneath the wing. The consequence was a decrease in the magnitude of the velocity vectors behind the wing and a decayed circulatory flow pattern for the same axial location. As a result, the enhancement in heat transfer at the channel exit due to the delta wing was 34% in the absence of stamping as compared to only approximately 10% when stamping is used. However, the spanwise averaged friction factor, (f x Re), for the case of the delta wing with stamping was 31% lower than that for the case of the attached delta wing without stamping.

Vortex Breakdown

Using naphthalene sublimation and the heat and mass transfer analogy, Gentry and Jacobi [1997] demonstrated the possibility for a 50% to 60% enhancement in the average heat transfer using delta-wing vortex generators for flow over a flat plate at low Reynolds numbers (Re = 600-1000). Gentry and Jacobi also showed that vortex breakdown occurs approximately four chord lengths downstream of the wing.

Core Pressure Drop

Fiebig *et al.* [1990] examined small, punched-out delta-winglet pairs in a wind tunnel with a vertical test section. These winglets, which had a winglet-to-fin area ratio of 0.003, were placed in simple channel flow and angled relative to tubes inside the test section. For Reynolds numbers between 2000 and 5300, the winglet pair exhibited an overall heat transfer enhancement of 20% under optimal geometrical conditions. More interesting, however, was the corresponding 7% reduction in drag. This research shows the possibility for a winglet pair in a fin-and-tube geometry to simultaneously increase heat transfer while decreasing flow losses.

Full-Scale Testing

Full-scale implementation and testing of vortex generators in heat exchangers is only sparsely reported in the literature. One of two known tests was performed by Russell *et al.* [1982] as part of a project for CE-Lummus. Their experiments relied on a transient melt-line method to gauge the effectiveness of various vortex generator configurations in full-scale flat tube heat exchangers. As a result of their work, the rectangular winglet placed in two staggered rows with a 20° angle of attack was identified as the most promising configuration. For a Reynolds number of 500 based on hydraulic diameter, the j factor was enhanced by 47% while the f friction factor increased by 30%. The results were even more encouraging for Reynolds numbers 1500 to 2200 where the j/f ratio was observed to exceed 0.5. The main weakness of their work, however, was their reliance on existing plain-tube correlations as the basis for their comparison. Full-scale tests on unenhanced but otherwise identical coils were never performed.

A more recent full-scale test of delta-wing vortex generators on a plain-fin-and-tube heat exchanger showed considerable heat transfer augmentation with little to no associated pressure drop penalty [El Sherbini and Jacobi, 2000]. For this study, two different delta wing sizes were tested on a plain-fin heat exchanger common to refrigerator applications. The result of using the smaller wings was a 14% to 18.3% increase in the Colburn j-factor whereas the larger wings produced a 24.7% to 31.3% increase in the j-factor with a maximum uncertainty of ±9%. In both cases, the wing-to-fin area ratio was less than 1.5% and thus constituted a negligible addition to the fin material. The most surprising result of this study, however, was the negligible change in the friction factor

associated with these heat transfer improvements. Previous research by others has suggested that passive enhancement by vortex generation would almost certainly incur a drag penalty. So, this negligible penalty in pressure was very interesting and attributed to the dominating pressure drop across the tubes in the heat exchanger.

1.2.2 Frost Growth Studies

Because of the breadth of encompassing literature, this topic will be subdivided for ease and convenience into frost properties, growth rate models, and the holistic testing of evaporator coils under frosting conditions. Many more studies on frost growth exist in the literature (White and Cremers 1981; Ogawa, Tanaka, and Takeshita 1993; Schneider 1978; Tao *et al*. 1993; Gall and Grillot 1997; and Inaba and Imai 1996), and the reader is encouraged to consult these sources as well. What follows is the author's attempt to emphasize those findings deemed especially relevant to this study.

Frost Properties

Ö stin and Andersson [1991] concluded that the plate surface temperature and the relative humidity of the air stream both affect frost thickness; whereas, the density of the frost largely depends on the air velocity and to a lesser extent on the relative humidity. Density, however, was independent of surface temperature. Similarly, the mass deposition rate of the frost was shown to have considerable dependence upon the relative humidity and air velocity. The mass rate was 3.6 times greater at 72% relative humidity than it was at 31%. The mass rate increased by a factor of 2.4 during tests conducted with an air velocity of 5.7 m/s compared to 2.6 m/s. A transient one-strip method was used to measure the frost properties. A weighing plate was used to measure frost accumulation, and a micrometer fitted with a fiber optic endoscope was used to measure the frost thickness. By taking the partial derivative of frost mass with respect to time, Ö stin and Andersson also examined the contribution of the mass flux of condensed vapor to frost density and frost thickness. They found that for times greater than 60 minutes, the contribution of the mass flux that went towards increasing the frost thickness varied between 0.41 and 0.65 with an average value of 0.49. This fact suggests that under quasi-steady conditions, the condensing water vapor contributes nearly equally to the increase of frost density and frost thickness. For their work, Ö stin and Andersson used a polynomial-based correlation for the thermal conductivity ($k = -8.71x10^{-3} + 4.39x10^{-4}\cdot\rho + 1.05x10^{-6}\cdot\rho^2$) that yielded conductivities in the range of 0.05-0.2 W/m-K for frost densities in the range of 75-275 kg/m^3.

Rite and Crawford [1991] also looked at the impact that various environmental parameters have on the frost rate. The evaporator tested was a top-mount, automatic defrost mechanically fit model with a fin spacing of 5 fpi that employed a parallel-cross/counter-cross flow arrangement. Relative humidity was controlled using a heated, evaporative-pan humidifier. In this study, a maximum discrepancy of 15% existed between calculating the frosting rate by direct measurement of the water level in the pan and the weighing of the frosted coil. This discrepancy suggests that a theoretical frost deposition rate based on experimentally collected upstream and downstream relative humidities should be acceptable. Rite and Crawford also observed that the accumulation of frost on the coil did not significantly influence the frosting rate flux. The average frosting rate flux was essentially the same after 10 hours as it was after 5 hours. Rite and Crawford also explained a discrepancy found in the literature concerning the effect that velocity has on the frosting rate. Earlier work by Senshu [1990] had suggested that the frosting rate decreases with increasing air velocity. Other researchers, however, observed the opposite trend. Rite and Crawford explained this

apparent contradiction by examining four parameters linked to the airflow rate that affect the frosting rate. These parameters are the mass transfer coefficient, surface temperature, air temperature, and moisture capacity of the air. Rite and Crawford showed that the mass transfer coefficient, air temperature, and moisture capacity of the air all increase with the airflow rate which tends to promote the mass driving potential. The surface temperature, on the other hand, also increases with the airflow rate, but this effect serves to decrease the driving potential. The net effect of the airflow rate on the frosting rate then is the sum of the relative contributions from these influences.

Theoretical Growth Rate Models

Cheng and Cheng [2001] proposed a theoretical model for predicting the frost growth rate on a flat plate. The Hayashi [1977] correlation was used to calculate the frost density, and the correlation by Brian *et al*. [1970] based on the mean frost surface temperature and the average frost density was used to calculate the effective thermal conductivity of the frost layer. Assumptions inherent to their model included uniform frost density throughout the frost layer at any instant, orthogonal growth of the frost layer relative to the plate surface, uniform frost thickness, and constant heat and mass transfer coefficients (h and h_m) on the frost surface. The derived expression for frost thickness using these forth stated assumptions and correlations is

$$\frac{dd_f}{dt} = \frac{h_m\left(w_a - w_s\right)}{147.55 \cdot d_f \exp[0.277(T_s - 273.15)](dT_s/dd_f) + r_f},$$

where the first term in the denominator accounts for the water vapor that goes to increase the frost density and is equal to dr_f/dt. Their model, however, assumes a Lewis number of unity and a driving potential based on a linear difference (instead of a log-mean difference) of the humidity ratios between the air and the frost surface. Comparisons were made with other existing theoretical models by Jones and Parker [1975] and Sherif, *et al*. [1993].

Cheng and Wu [2003] examined frost formation on a flat plate subjected to atmospheric air flow in a suction-type, open-loop wind tunnel using a CCD camera and a PCI frame grabber at an image-sampling rate of 5 seconds. Cheng and Wu distinguished between three different time periods in the formation of frost as was done previously by Hayashi [1977] and called them the crystal growth period, frost layer growth period, and full growth period, respectively. According to Cheng and Wu, in this last period a multiple-step ascending frost growth pattern emerges, which periodically results in a slight decrease in the frost thickness due to the melting of frost crystals on the surface, the collapse of the frost layer, and the penetration of melted water. The range of the examined environmental parameters were $2 \le V \le 13$m/s, $20° \le T_a \le 35$°C, $40\% \le \phi \le 80\%$, and $-13 \le T_w \le -2$ °C. Cheng and Wu also offered several reasons for the disparity of results in the literature concerning the effects of air temperature on frost thickness. One explanation they put forward was that when warmer air arrives at the frost surface, it may not be cooled immediately to below the freezing point but may enter the frost layer and aid in densification instead of surface-level deposition. A second explanation offered by Cheng and Wu was that the higher temperature air raises the frost surface temperature and in this way promotes the melting of the frost columns and branches at the surface. It was also noted, however, that higher temperature air usually can hold more moisture, a phenomenon known to increase the driving potential. Cheng also checked these experimental results against his model described above. The data agreed reasonably well with the model, especially during the frost layer growth period.

Evaporator Performance with Frost

In a separate paper, Rite and Crawford [1991] also extensively and systematically studied the effects of various parameters (i.e. RH, air flow rate, and air temperature) on the UA-value of a mechanically fit, domestic refrigerator evaporator under frosting conditions. They found that while holding the air flow rate constant, the UA-value steadily increased as frost was deposited on the coil. This result differed from earlier studies, which reported an initial increase in UA followed by a decrease in UA with continuing frost deposition. To further substantiate this claim, Rite and Crawford conducted a single 24-hour experiment over which the UA-value eventually leveled off but never showed evidence of decreasing. They also claimed that the thermal conductivity of the frost layer had only a small to modest influence on the heat transfer of the evaporator (contrary to the insulating effect suggested by other researchers) since the UA-value increased for the duration of their testing. Finally, by attaching type-T thermocouples to the fin, Rite and Crawford showed that although the surface resistance decreased by 10% during the test period, the contact resistance only decreased by approximately 2%, suggesting that the filling of the gaps between the tube and fin was negligible.

Mago and Sherif [2002] modeled the process path of an industrial evaporator coil under frosted conditions. The motivation for the study was to determine the thermo- physical properties of the air stream leaving a given row of an *n*-row coil with the hope of identifying the location where the moist air stream reaches a supersaturated state on the psychrometric chart. Supersaturated conditions lead to the generation of airborne ice crystals, which produce snow-like frost on the heat exchanger surface and degrade the capacity of the coil. In this paper, Mago and Sherif used a log- mean enthalpy difference method that was based on a fictitious saturated air enthalpy evaluated at the refrigerant temperature. Their work confirmed that as the relative humidity of the entering air is increased, the transition to supersaturated air occurs earlier in the coil.

1.2.2 Studies of Vortex Generation Under Frosting Conditions

Aside from early work by Storey and Jacobi [1999] for a channel flow, no research on the use of vortex generators under frosting conditions has been reported where the accumulating frost can change the geometry of the flow. Moreover, although this research in channel flow qualitatively suggested that the vortex generator should function properly under frosting conditions and should not affect frost thickness, this hypothesis was not tested on a full-scale heat exchanger.

1.3 Project Objectives

The specific objective of this study is to examine the performance of delta-wing vortex generators under low airflow rates typical to domestic refrigeration, their efficacy downstream from the leading edge, and their frost tolerance under maximum frost accumulation. Geometrical placement of the vortex generators inside an evaporator for maximum thermal enhancement is also explored, since previous full-scale testing of vortex generators has focused almost exclusively on placing the VG at the leading edge of the fin material. Despite some known benefits, several questions remained unanswered about vortex generation in a frosting environment. Can vortices be restarted? Are vortex generators equally effective when placed at distances L/2 and L/4 downstream from the leading edge? How do they perform under maximum frost blockage conditions? Will frost growth adversely affect the enhancement effect of the generator? A key question to be answered is the efficacy of a midstream generator

throughout a full operational cycle (from defrost to frost). To answer these questions, full-scale testing of a brazed refrigerator evaporator with and without delta wings under frosting conditions is conducted in a closed loop wind tunnel. The two parameters used in this evaluation are airside thermal resistance and core pressure drop.

Chapter 2- Experimental Methodology

2.1 Wind Tunnel Configuration

2.1.1 Air Side Loop

The experiments were conducted in a closed-loop wind tunnel comprised of 5 major sections: a thermal-conditioning chamber, flow-conditioning chamber, contraction, test section, and return loop as shown in Figure 2.1. The temperature and humidity of the air were established inside the thermal-conditioning chamber prior to each experiment using an upstream cooling coil and a controlled steam injection system. In order to ensure a thoroughly mixed flow of uniform temperature and humidity, a static mixer at the fan outlet and a centrifugal mixer were used. The flow then passed through a series of honeycombs and screens per the recommendations of Scheiman [1981] to achieve a uniform velocity distribution. A 12-to-1 contraction was used to provide a smooth transition between the flow-conditioning chamber and the test section and reduce turbulence intensity. The test section was made of 12.7-mm thick transparent acrylic and had a height of 50.8 mm and a maximum span of 610 mm. Interior contractions were used to reduce the tunnel span to the testing width of the heat exchanger. The core pressure drop across the heat exchanger was measured using four pressure taps (two upstream and two downstream) and a 250 Pa pressure transducer with an uncertainty of 0.073% full-scale. Air inlet and outlet temperatures were measured by 7 thermopiles placed upstream and downstream of the exchanger. These thermopiles were inserted from both the top and the bottom surface of the test section with an average spanwise interval of 75 mm between them. Each thermopile consisted of five 0.25-mm-diameter, type-T thermocouples calibrated against NIST-certified ASTM thermometers. The resulting uncertainty in the average air temperature was ±0.08°C.

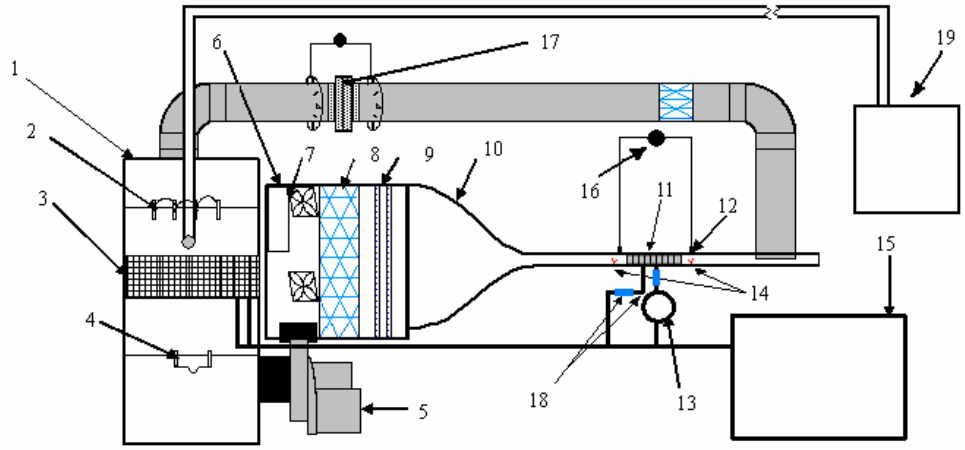

1	Thermal conditioning	11	Test section
2	Pre-heaters	12	Pressure taps
3	Cooling coils	13	Coolant flow meter
4	After heaters	14	Thermocouples
5	Blower	15	Chiller
6	Flow conditioning	16	Pressure
7	Mixers	17	Orifice Plate
8	Honeycomb	18	Mixing Cups
9	Screens	19	Boiler
10	Contraction		

Figure 2.1- Wind tunnel schematic with descriptors

A 152-mm-diameter PVC return pipe insulated with 12.7-mm thick Armaflex® sheet insulation (k=0.27 W/m-K) closed the air circuit. The flow rate was measured using an ASME Standard orifice plate with 53.3 mm bore diameter (β=0.34). In keeping with ASME recommendations, the flow was conditioned before reaching the orifice plate. This conditioning was accomplished using turning vanes in the 90° elbow, a honeycomb downstream of the elbow, and a straight length of 6*D* upstream from the orifice plate. The pressure drop across the orifice plate was measured using a pressure transducer calibrated to an accuracy of ±0.3% of the full-scale.

2.1.2 Coolant Side Loop

The coolant used in these experiments was a single-phase ethylene glycol aqueous solution with a concentration of 41.1% by volume. The inlet and outlet fluid temperatures were measured using platinum RTDs with an uncertainty of ± 0.017°C. Mixing cups (as shown in Figure 2.2) and 90° elbows were incorporated into the piping network upstream and downstream of the RTDs to ensure a uniformly mixed, bulk fluid temperature. A Coriolis-effect flow meter was installed just downstream from the heat exchanger to measure the coolant mass flow rate with an uncertainty of ± 0.15%.

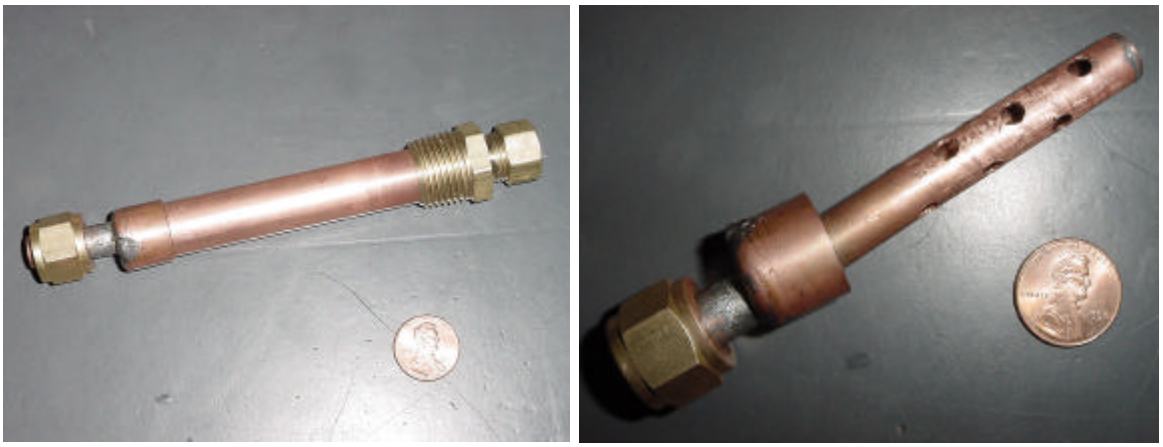

Figure 2.2- Mixing cups were used to ensure uniformity of the bulk fluid temperature.

2.2 Evaporator Geometry

The heat exchanger used for conducting this comparison was a plain-fin-and-tube construction with fin spacing of 8.47 mm. The testing length and height of the heat exchanger were 451 mm and 51 mm respectively, and the fin length was 203 mm as indicated in Figure 2.3. The fins were brazed to the tube in order to eliminate thermal contact resistance as shown in Figure 2.4. There were 8 tube rows each with 2 columns. The outside tube diameter was 9.53 mm, and the hydraulic diameter of the exchanger was 10.2 mm.

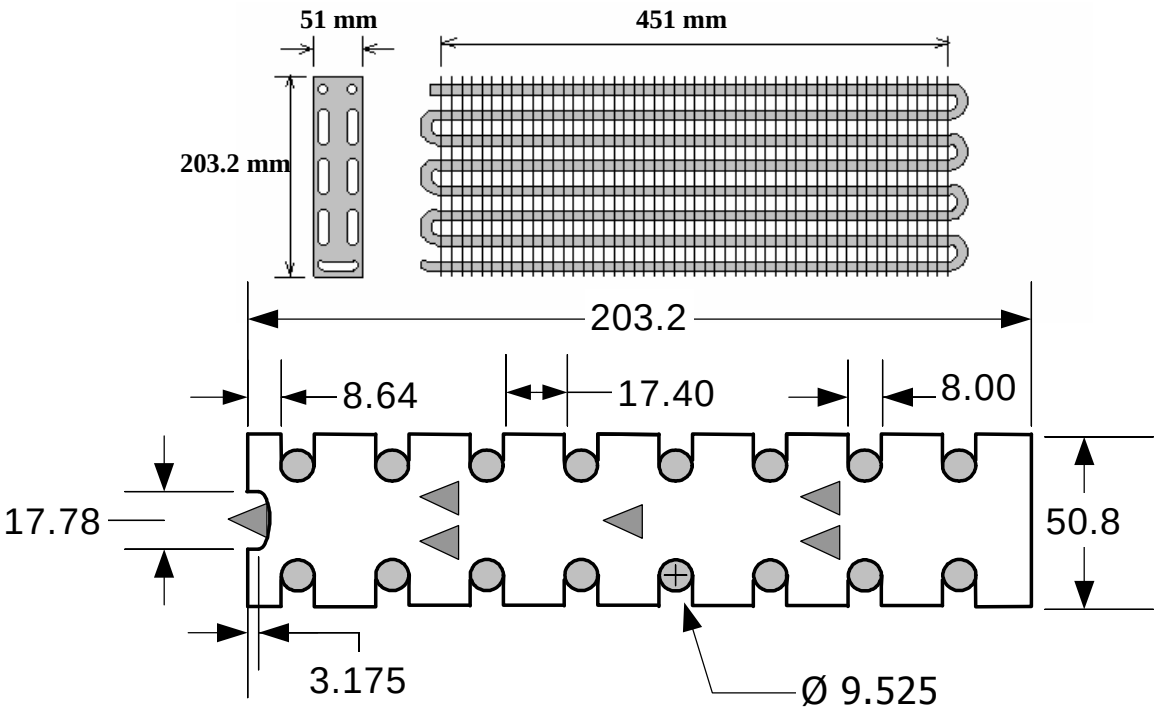

Figure 2.3- A schematic of the evaporator with dimensions

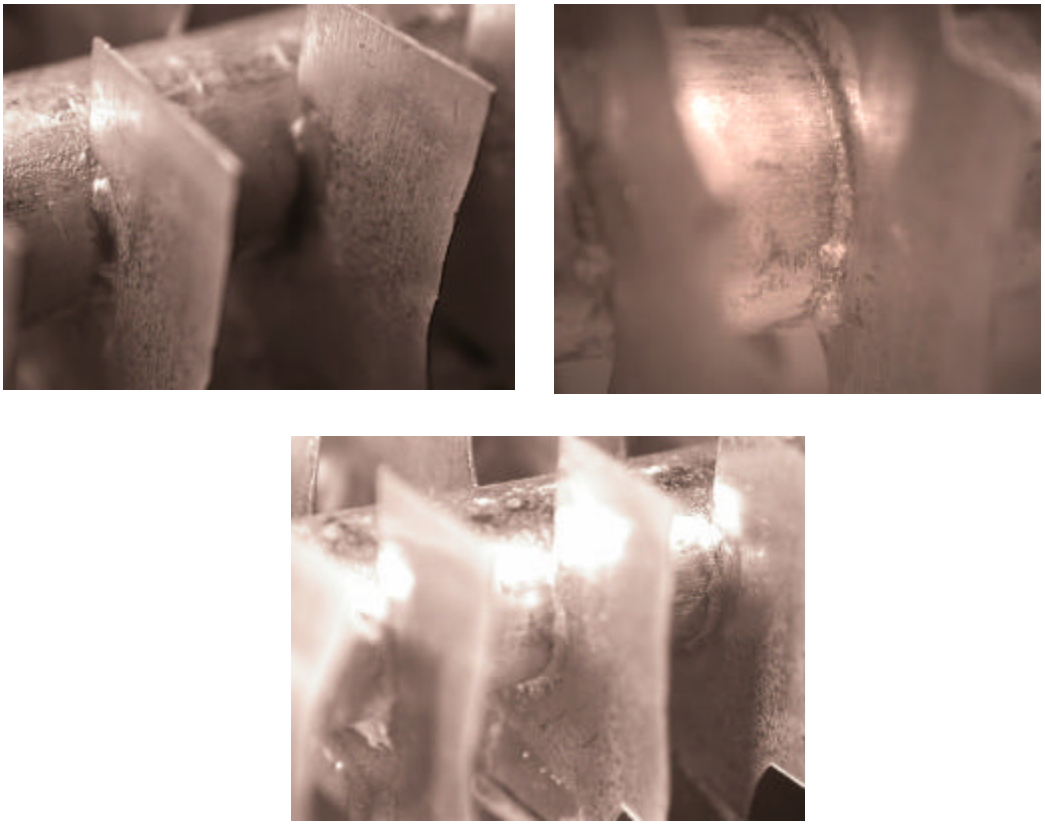

Figure 2.4- The tested evaporator had brazed fin and tube joints to eliminate contact resistance.

2.3 Vortex Generator Geometry

The delta wing vortex generators selected for testing were "nearly optimal" per the recommendations of Gentry and Jacobi [1998] for low Re_{dh} channel flows. The vortex generators were cut from standard 0.254-mm aluminum shim stock using wire electrical discharge machining (EDM) and possessed an aspect ratio, Λ, of 2.0 and an angle of attack, α, of approximately 55°. They were attached to the heat exchanger at the leading edge and at various locations downstream using non-conducting tape to ensure that the delta wings did not contribute additional heat transfer surface area. Nevertheless, the addition of the vortex generators to the evaporator only accounted for 1.1% – 3.1% of the total possible surface area. In this way, any heat transfer enhancement observed was due to the generated longitudinal vortex, and this attachment technique more closely mimics the presumably desired way of manufacturing vortex generators, which is punching them out of the existing fin material. All relevant wing dimensions are detailed below in Figure 2.5.

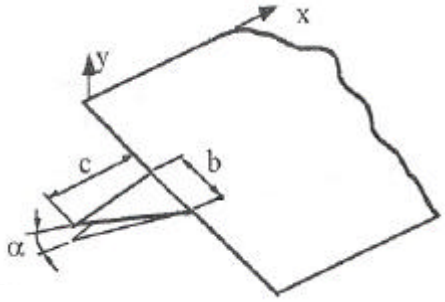

Wing base, b (mm)	10.5
Wing chord, c (mm)	10.5
Chord to hydraulic dia. (c/D_h)	1.027
Aspect ratio, Λ=2b/c	2.0
Angle of attack, α	55°

Figure 2.5- Schematic of a vortex generator with relevant dimensions

Three different vortex generator configurations were examined for the purposes of identifying a promising configuration and determining whether thermal enhancement is linked more specifically to vortex generator placement or merely the vortex coverage area. Although somewhat arbitrary in choice, the delta wing rows in Configurations B and C were separated by a distance approximately equal to 4.8 chord lengths, or 50.8 mm. Earlier work by Gentry and Jacobi [1997] had showed that for a delta wing with an aspect ratio of 1.25 and an angle of attack of 35° in developing channel flow at Re_{dh} =400 that a streamwise-length ratio, x/L, of approximately 0.50 (*Ref. Figure 5.32, p. 103*) corresponded to the location of diminishing local Sherwood number. Although the vortex was still coherent at this point, the impact of the vortex had weakened due to viscous diffusion and core lift-off. Because the tested channel-length-to-chord-length ratio, L/c, for Gentry's local Sherwood plot was 11.43, an equivalent streamwise spacing-to-chord-length ratio, x/c, could be found for my geometry by multiplying these two ratios together. The resulting spacing ratio, x/c, was 5.715, which corresponded to a suggested streamwise spacing of 60mm for the delta wing geometry of this study. This simple calculation was the reason that the delta wings were applied to the fin material every other tube pass, a distance of 50.8mm. Configuration A was comprised of only 2

rows of vortex generators (n=108) attached both at the leading edge and again halfway downstream. Configuration B, on the other hand, consisted of 6 rows of vortex generators (n = 324) in a staggered arrangement that followed this "optimal" spacing outlined above. In this arrangement, single rows of centered delta wings were followed by two rows of delta wings attached to the adjoining fin across the passage. This 2-1 staggered pattern was then repeated for the length of the coil. Configuration C also consisted of 6 rows of delta wings (n = 324) but followed a 2-1 inline arrangement where all the delta wings were attached in the same direction on the same fin. All three of these configurations are depicted in Figure 2.6.

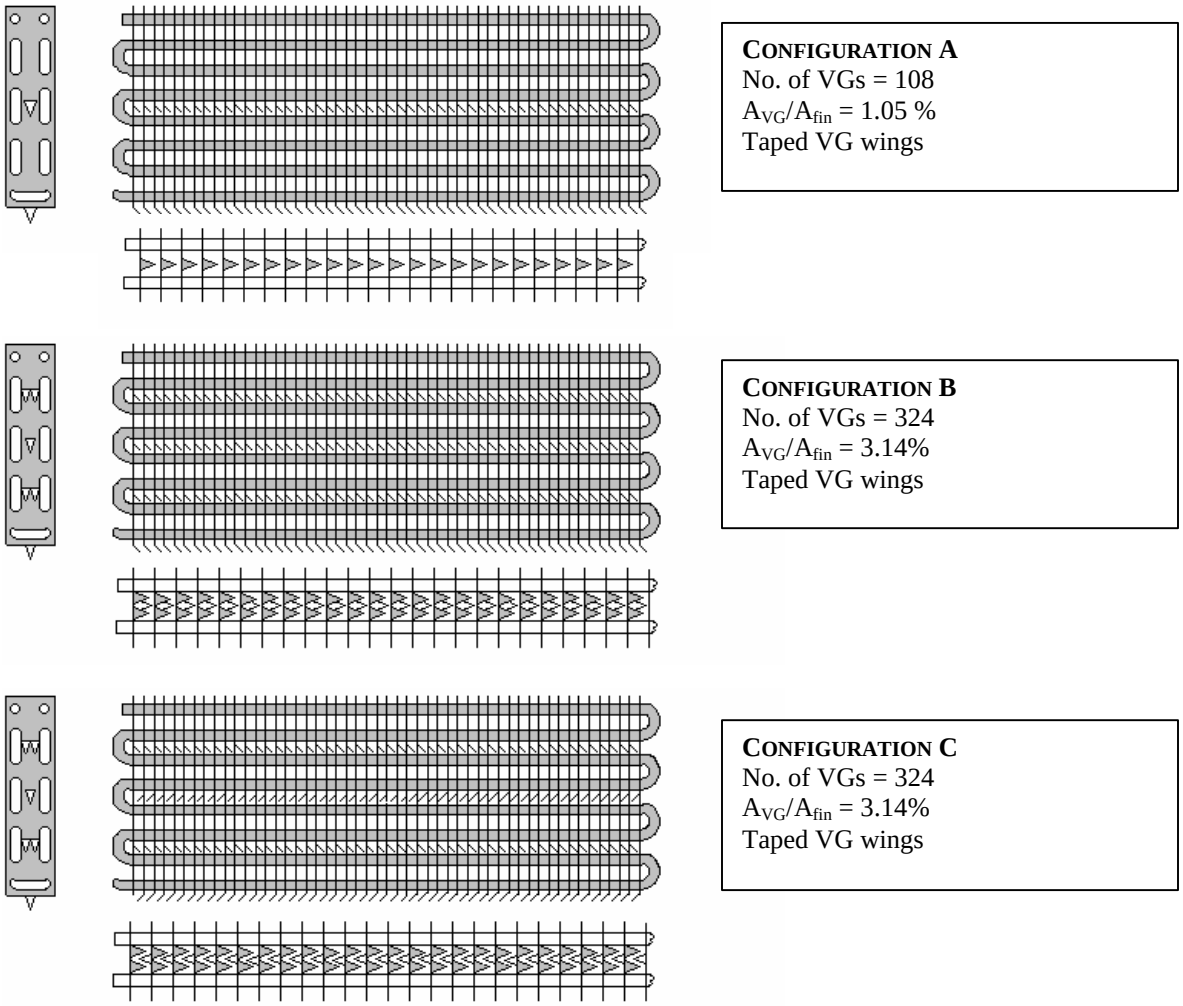

Figure 2.6 - Three different vortex generator arrays were tested under frosting conditions.

2.4 Uniform Test Conditions

Because vortex generation at low airflow rates was the focus of study, it was necessary to check the air approach velocity profile inside the test section just upstream of the evaporator to ensure uniformity and negligible turbulence in the flow. In this way, any observed thermal enhancement could be directly attributed to the vortex generator instead of inherent unsteadiness in the flow. To measure the velocity of the approach air, a hot-ball anemometer was inserted into seventeen, evenly spaced locations in the test section- each separated by a distance of 2.54 cm. These measurement sites were located immediately upstream of an evaporator with a fin spacing of 5.08

mm. At each of these locations, three different depth measurements were recorded corresponding to heights of 15.9 mm, 28.6 mm, and 41.3 mm as measured from the base of the test section. Using this approach, the velocity profiles were shown to be flat within ±4.3% for the lowest test velocity (0.46 m/s) and ±5.7% for the highest test velocity (2.0 m/s) as seen in Figure 2.7. The lowest air velocities were observed near the top of the test section and were attributed to the close proximity of thermopiles in this region.

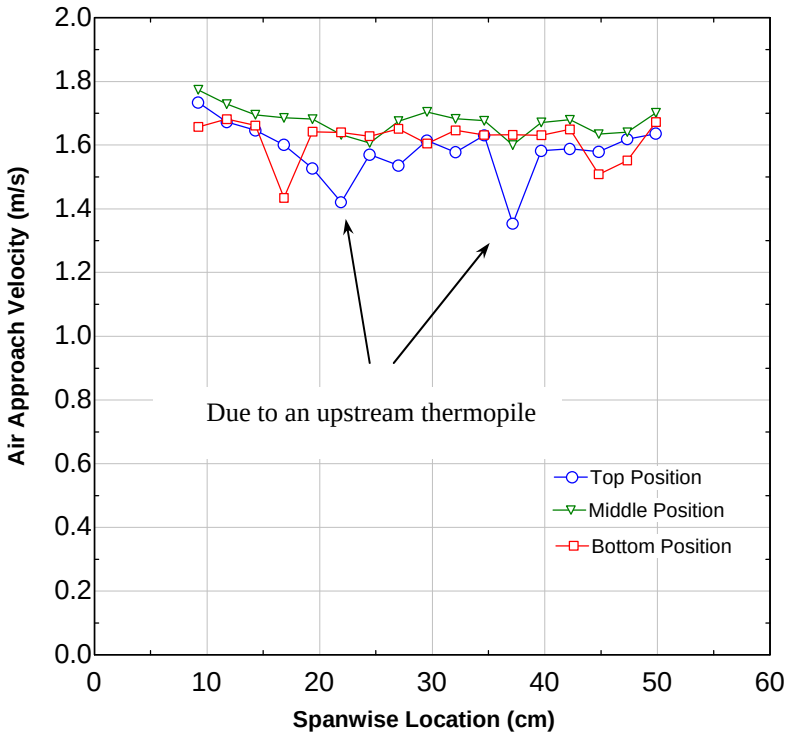

Figure 2.7- A typical velocity profile of the approaching air stream

The turbulence intensity was also approximated inside the wind tunnel using the definition

$$I \equiv \frac{\sqrt{\overline{(u')^2}}}{\bar{u}} = \frac{\left[\frac{1}{T}\int_{t_O}^{t_O+T}(u')^2\,dt\right]^{1/2}}{\bar{u}}, \qquad [1]$$

where T is the time interval, u′ is the fluctuating velocity component, and u is the mean velocity. Assuming the velocity to be quasi 1-D flow, this task is accomplished by continuously recording the velocity at a given location over a 10-second interval and then taking the root-mean-square of these values and dividing by the arithmetic mean. Despite the large data scatter and uncertainty in these measurements, these tests showed that over the range of tested air velocities, the turbulence intensity never exceeded 2.25%. In fact, for 92% of all tested locations, the turbulence intensity was less than 1% as shown below in Figure 2.8.

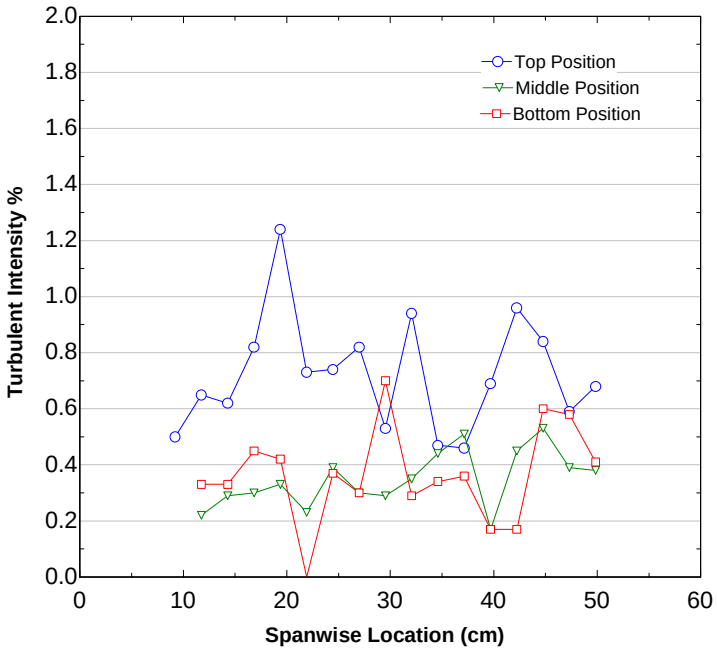

Figure 2.8- The turbulence intensity of the air stream never exceeded 2.25%.

2.5 Data Reduction and Interpretation

2.5.1 ε -NTU / Ablimation Energy Method

Energy balances were monitored to ensure fidelity of all measured data. For 80% of the data points shown below, the maximum energy transfer rate difference was 3.4% while the remaining 20% of the data had energy balances between 5-9%. An ε-NTU method was then utilized to measure the performance of the heat exchanger. For the geometry studied, the exchanger can be divided into two halves along an adiabat, as shown in Figure 2.9, with each partition containing 8 passes in cross-flow. The upper partition has an overall counter flow arrangement while the lower partition has an overall parallel flow arrangement.

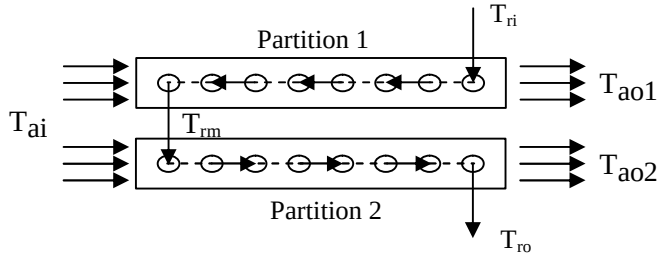

Figure 2.9- The evaporator was divided into parallel flow and counter flow partitions.

On the basis of an energy balance for each stream, the following expressions were then written:

$$q_1 = C_{a1}\left(T_{ai} - T_{ao1}\right) + 0.5\dot{m}_{frost} h_{sg} \quad [2]$$

$$q_1 = C_r\left(T_{rm} - T_{ri}\right) \quad [3]$$

$$q_2 = C_{a2}\left(T_{ai} - T_{ao2}\right) + 0.5\dot{m}_{frost} h_{sg} \quad [4]$$

$$q_2 = C_r\left(T_{ro} - T_{rm}\right) \quad [5]$$

where C_r is the heat capacity of the refrigerant, $\dot{m}_{frost}$ is the frost deposition rate, h_{sg} is the ablimation energy of the frost, and C_{a1} and C_{a2} are the heat capacities of the moist air for the upper and lower partitions respectively. In these equations, q_1, q_2, $T_{rm,}$ T_{ao1}, and T_{ao2} are all unknowns. In this analysis, equal moist air heat capacities and frost loading are assumed for both partitions. This assumption is based on symmetry arguments and is supported by the data. For example, air velocity measurements recorded immediately upstream of the heat exchanger reveal that velocity differences between the top and bottom of the test section are always less than 10%. Furthermore, the temperature difference between the inlet and the outlet coolant streams will never exceed 1.2°C which corresponds to a maximum air-side enthalpy driving potential difference of 5.6% between the two partitions. This fact supports the idea of uniform and nearly identical thermophysical properties of the developing frost layer in both partitions.

By measuring the humidity ratio, the frost deposition rate is calculated using the equation,

$$\dot{m}_{frost} = \dot{m}_{air,up} mf_{w,up} - \dot{m}_{air,down} mf_{w,down} \quad [6]$$

where $mf_{w,up}$ and $mf_{w,down}$ represent the mass fractions of the water in the air upstream and downstream, respectively, and $\dot{m}_{air,up}$ and $\dot{m}_{air,down}$ represent the mass flow rates of the moist air upstream and downstream, respectively. The ablimation energy h_{sg} is found using a correlation to account for variations in the latent energy with ambient temperature [Wexler *et al.*, 1983]. The ε-NTU equations used to complete the system of equations are then written as follows:

$$q_1 = e_1 C_{a1}\left(T_{ai} - T_{ri}\right) + 0.5\dot{m}_{frost} h_{sg} \quad [7]$$

$$q_2 = e_2 C_{a2}\left(T_{ai} - T_{rm}\right) + 0.5\dot{m}_{frost} h_{sg} \quad [8]$$

where C_{a1} and C_{a2} equal C_{min} because $C_a < C_{r.}$ Appropriate relations for the counter-flow partition effectiveness ε_1 and the parallel flow partition effectiveness ε_2 given in Rohsenow *et al.* [1985] are used to relate the pass effectiveness ε_p to the partition effectiveness ε_1 and ε_2 as shown

$$e_1 = \frac{\left(\frac{1 - e_p R_C}{1 - e_p}\right)^{N_{passes}} - 1}{\left(\frac{1 - e_p R_C}{1 - e_p}\right)^{N_{passes}} - R_C} \quad [9]$$

$$e_2 = \frac{1 - \left(1 - e_p\left(1 + R_C\right)\right)^{N_{passes}}}{1 + R_C} \quad [10]$$

The airflow was unmixed due to finning, but the coolant flow was mixed. For such a configuration, the effectiveness of an individual tube pass can be expressed as:

$$e_p = \left\{1 - \exp\left[-R_C\left(1 - \exp\left(-NTU_P\right)\right)\right]\right\} / R_C \quad [11]$$

where R_c is the heat capacity ratio $R_c = C_{a1}/C_r = C_{a2}/C_r$. In this analysis, the effectiveness of each tube pass ε_p in a partition is considered equal since the coolant-side convective heat transfer coefficient in each pass is assumed to be equal. The number of transfer units per pass is then related to the thermal conductance per pass using the equation,

$$NTU_P = UA_P / R_C \quad [12]$$

From this information, the total thermal conductance, UA_{tot}, is found by summing over all passes.

The total thermal resistance, R_T, which equals $1/UA_{tot}$, can in turn be represented as a series of individual resistances as shown in Figure 2.10. It is, therefore, equivalent to the sum of the refrigerant convection resistance ($R_{r\text{-}conv}$), tube wall conduction resistance ($R_{t\text{-}cond}$), frost conduction resistance (R_{frost}), and air-side convection resistance, (R_{as}), where the frost resistance and air-side resistance are each independently comprised of parallel resistances due to the tube and fin. The tube-side convection resistance is found using the Gnielenski correlation and the Colebrook correlation because the tube-side Reynolds number, Re_{Do}, was always greater than 2300, and these correlations were shown to be more suitable for lower Reynolds number flows [Bhatti and Shah, 1987]. Because the fin-to-tube contact resistance $R_{contact}$ is zero, the frost conduction resistance is approximated using the following equations and correlations:

$$\frac{1}{R_{frost}} \approx \frac{k_f \cdot A_{fin}}{d_f} + \frac{2pLN_{tubes}k_f}{\ln((r_o + d_f)/r_o)} \quad [13]$$

$$d_f = \int_0^t \dot{m}_{frost} / (A_{tot} \cdot r_f) dt \quad [14]$$

$$r_f = 650 \exp(0.277 \cdot T_f) \quad \text{[Hayashi, 1977]} \quad [15]$$

$$k_f = 0.132 + 3.13e^{-4} r_f + 1.6e^{-7} r_f^2 \quad \text{[Lee } et\ al.\text{, 1997]} \quad [16]$$

where δ_f represents the frost thickness and T_f represents the average interfacial frost surface temperature of the frost surface. The frost surface temperature, T_f, is extracted from the heat-and-mass transfer analogy by relating the frost mass deposition rate to the log-mean humidity ratio difference between the air and the frost surface. In this way, the humidity ratio, ω_s, (and hence temperature T_s) at the frost surface can be calculated using the following relationship

$$\dot{m}_{frost} = \frac{h}{c_{p,air}} A_{tot} Le^{-2/3} \Delta w_{lm} \quad , \quad [17]$$

where

$$\Delta w_{lm} = \frac{(w_{in} - w_s) - (w_{out} - w_s)}{\ln[(w_{in} - w_s)/(w_{out} - w_s)]} \quad [18]$$

and *Le* is the Lewis number and A_{tot} is the total heat transfer surface area. From this information, the reciprocal of the refrigerant Nusselt number is plotted along the abscissa, and the total thermal resistance R_T is plotted along the ordinate to form a so-called Wilson plot. The air-side resistance of the heat exchanger, R_{as}, defined as

$$\frac{1}{R_{as}} = \frac{1}{R_{a,\,fin}} + \frac{1}{R_{a,\,tube}} = h \cdot \left(h \cdot A_{fin} + A_{tube}\right), \quad [19]$$

is inferred from a Wilson plot by extrapolating to the ordinate intercept. Here the tube-side refrigerant Nusselt number is infinite (i.e. $1/Nu_R = 0$), and the tube-side convection resistance equals zero. As a result, the intercept

equals the air-side resistance plus the contribution of the resistance due to the frost and tube wall- both known quantities. The fin efficiency, *h*, in the air-side resistance is calculated using the sector method proposed by Carrier and Anderson [1944]. The Wilson plot was chosen as the primary basis of comparison for these tests.

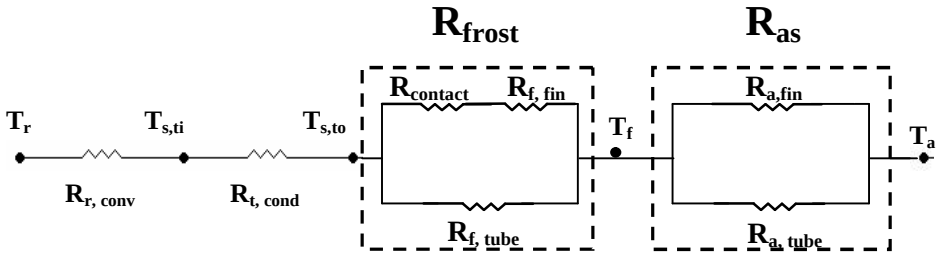

Figure 2.10- Thermal resistance network

2.5.2 Enthalpy Driving Potential Method

In this method, the heat exchanger is analyzed by partitions in the same way as the log-mean temperature difference method. The energy balances are now written, however, in terms of enthalpies and are not broken up into sensible and latent heat portions. Using this approach, the energy balances used to calculate the overall heat transfer coefficient, UA_{tot}, are written as:

$$q_1 = \dot{m}_{air}\left(h_{ai} - h_{ao1}\right) \quad [20]$$

$$q_1 = C_r\left(T_{rm} - T_{ri}\right) \quad [21]$$

$$q_2 = \dot{m}_{air}\left(h_{ai} - h_{ao2}\right) \quad [22]$$

$$q_2 = C_r\left(T_{ro} - T_{rm}\right) \quad [23]$$

where q_1, q_2, T_{rm}, h_{ao1} and h_{ao2} are unknowns and h_{ai} represents the enthalpy of the inlet at the measured temperature, T_{ai}, and relative humidity, RH_{up}. Because the effectiveness values associated with parallel flow and counter flow heat exchange are different as shown earlier, the enthalpy of the air exiting these partitions (i.e. h_{ao1} and $h_{ao2)}$ are different and thus constitute two separate unknowns. The ε-NTU equations used to complete the system of equations are then written as follows:

$$q_1 = e_1 \cdot \dot{m}_{air} \cdot \left(h_{ai} - h_{ri}\right) \quad [24]$$

$$q_2 = e_2 \cdot \dot{m}_{air} \cdot \left(h_{ai} - h_{rm}\right) \quad [25]$$

where h_{ri} is the maximum possible enthalpy for the counter flow section corresponding to a coolant inlet temperature, T_{ri} and a relative humidity value of unity, and h_{rm} is the maximum possible enthalpy for the parallel flow section corresponding to a calculated midstream coolant temperature, T_{rm} and a relative humidity value of unity. The values for effectiveness are found as before using the same relations described in the log-mean temperature difference method. Both of these methods, the log-mean temperature difference method with the extra term to account for latent effects and the log-mean enthalpy difference method, are shown to yield results similar to within 4.8%.

Chapter 3- Results and Discussion

3.1 Vortex Enhanced Area Predictions

Prior to testing, expected heat transfer enhancement was estimated using results from a parametric study conducted by Gentry and Jacobi [1998]. For $\Lambda = 2.0$ and $\alpha = 55°$, Gentry and Jacobi measured enhancement ratios of 1.2, 1.4, and 1.5 for $Re_{dh} = 400$, 1200, and 2000, respectively. These Sherwood number enhancement ratios were measured experimentally using naphthalene sublimation and were found to correspond directly to heat transfer coefficient enhancement via the heat and mass transfer analogy by the following relationship:

$$\frac{\overline{Sh}_E}{\overline{Sh}_O} = \frac{Nu_E \left(\mathrm{Pr}/Sc\right)^n}{Nu_O \left(\mathrm{Pr}/Sc\right)^n} = \frac{\bar{h}_E \left(L/k\right)}{\bar{h}_O \left(L/k\right)} = \frac{\bar{h}_E}{\bar{h}_O} \qquad [26]$$

The percentage of the total area affected by the vortex generators is approximated by a rectangle two and a half times the wing base times the streamwise distance to the next vortex generator. (This characteristic streamwise length assumes a coherent vortex structure from one delta wing to the next as depicted in Figure 3.1.) These assumptions are supported by Gentry and Jacobi's flow visualization work where the spanwise distance between flow lines was more than 2.5 times the wing base at its largest span and vortex breakdown was not observed over the entire test space (11.43 chord lengths). It is also assumed that the generated vortices will affect both sides of the channel. This assumption is reasonable since the bulk vertical velocity in the channel flow tends to lift the vortices away from the channel surface and cause them to travel along the centerline, thereby influencing both sides of the channel. Gentry and Jacobi [1998] also observed vortices traveling along the channel centerline a short distance downstream of the delta wing.

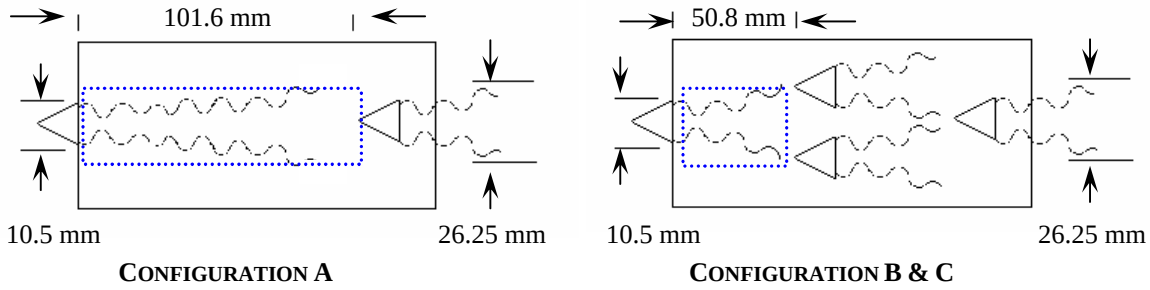

Figure 3.1- Schematic showing the vortex-affected areas (represented in blue) for the three tested configurations

Table 3.1: Predicted Heat Transfer Enhancement for Configuration A ($\Lambda = 2.0$ and $\alpha = 55°$)

Reynolds #, Re_{dh}	400	1200	2000
Gentry's Enhancement Ratio	1.2	1.4	1.5
% Enhanced Area	50.7	50.7	50.7
% Predicted Heat Transfer Enhancement	10.1	20.3	25.4

Table 3.2: Predicted Heat Transfer Enhancement for Configuration B,C (Λ = 2.0 and α = 55°)

Reynolds #, Re_{dh}	**400**	**1200**	**2000**
Gentry's Enhancement Ratio	1.2	1.4	1.5
% Enhanced Area	76.1	76.1	76.1
% Predicted Heat Transfer Enhancement	15.2	30.4	38.0

3.2 Configuration A (Brazed Evaporator)

3.2.1 Core Pressure Drop Summary

The thermal hydraulic performance of the evaporator was measured before and after the addition of the delta-wing vortex generators. In order to assess the pressure drop penalty associated with the enhanced geometry, delta wings were attached both along the leading edge and halfway downstream as prescribed by configuration A and tested over several air flow rates under dry conditions to mitigate the transient effects and sensitivity of the exchanger to frost growth. The results in Figure 3.2 reveal a small pressure penalty associated with the delta wings. The pressure penalty varies between 0.62 and 1.98 Pa with an uncertainty in the measurements of ± 0.182 Pa. This change in core pressure is small compared to the overall pressure drop observed in a completely frosted evaporator (i.e. ~250 Pa). It should be noted that incremental fan power in a typical refrigerator application is always less than 0.05 W when using this enhanced geometry. These trends are also reflected in the air-side friction factor shown in Figure 3.3.

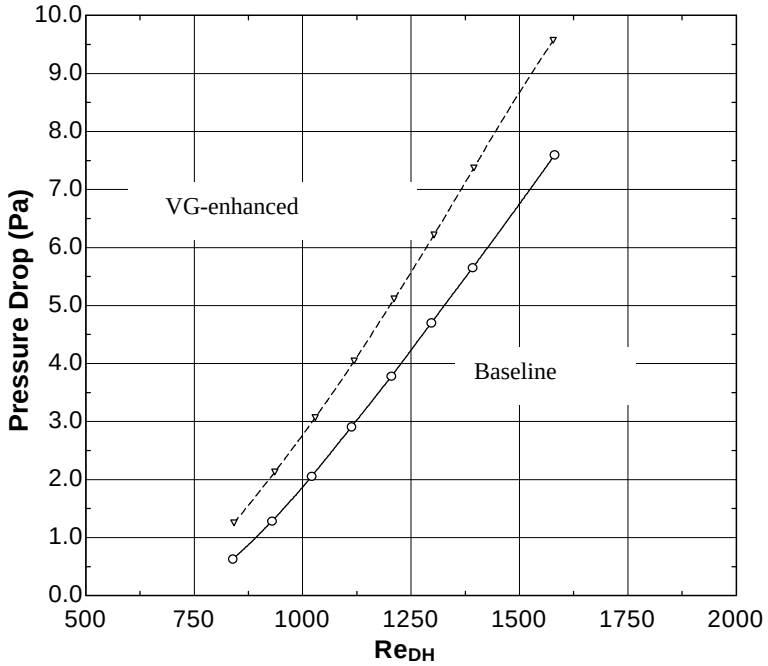

Figure 3.2- Pressure drop for two rows of vortex generators under dry conditions

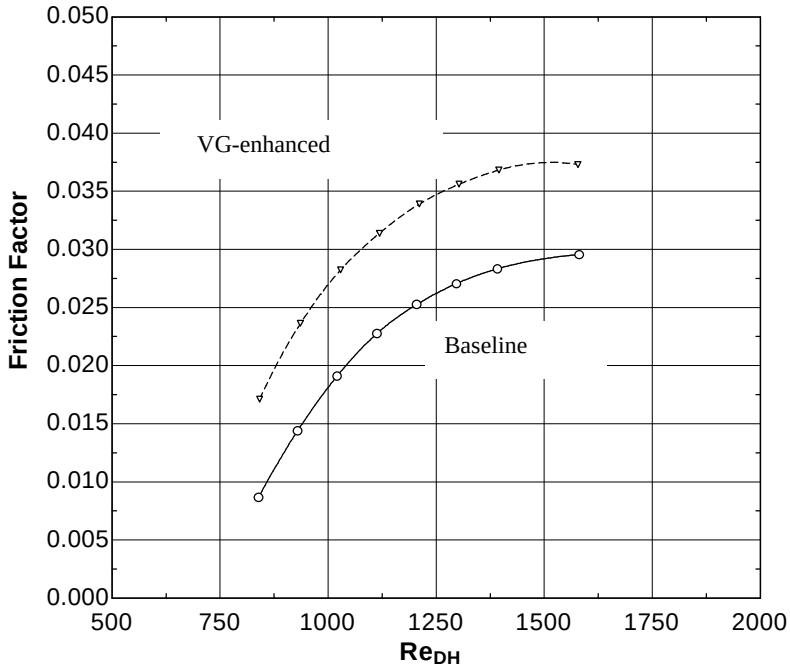

Figure 3.3-Friction factor for two rows of vortex generators under dry conditions

3.2.2 Wilson Plot Results

Heat transfer data from the evaporator were acquired every 5 minutes following an initial frost growth period of 20 minutes. The delta wings reduced the total thermal resistance of the evaporator by 3.5 to 22.8% as shown in Figures 3.4 and 3.5. Because the additional resistance contributed by the tube wall and frost layer was small (i.e. ~10%), this reduction could be largely ascribed to the fact that the air-side resistance was lowered due to increased convection and flow mixing in the finned channels. This enhancement was reflected in the behavior of the convective heat transfer coefficient, which was observed to increase by 3.9% to 28.0% over the range of tested air velocities. Because non-conducting tape was used to attach the delta wings and the wing-to-fin area ratio was 0.53%, these enhancements could be entirely attributed to the streamwise vortices. The uncertainty in the experiment ranged from 7.7–12.8% over the range of tested air velocities, thus statistically significant enhancements were only present down to a face velocity of 0.68m/s.

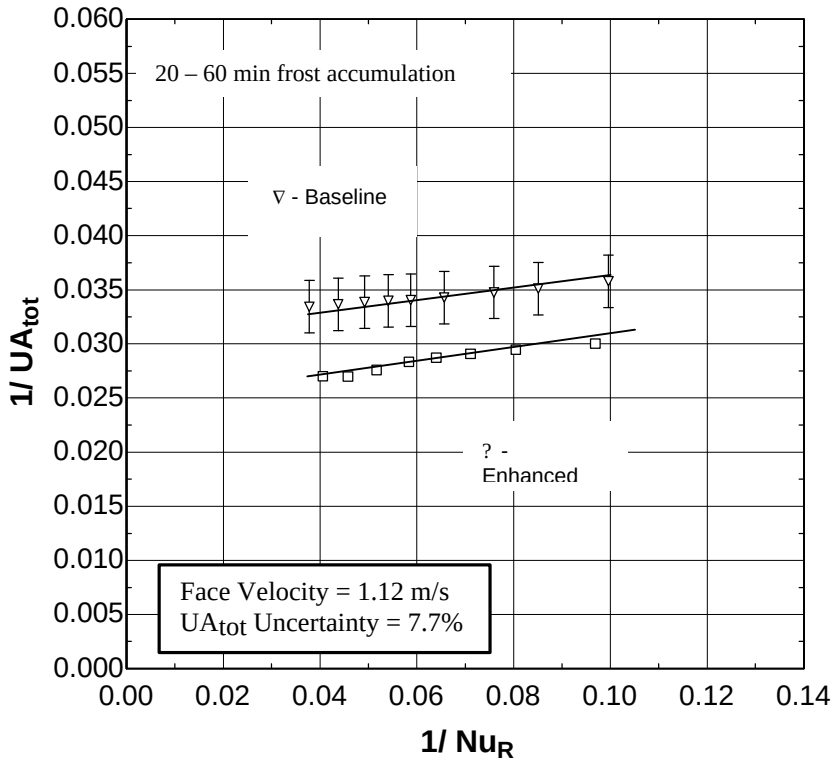

Figure 3.4- A significant decrease in the overall thermal resistance is observed on this Wilson plot for Re_{dh} = 1360.

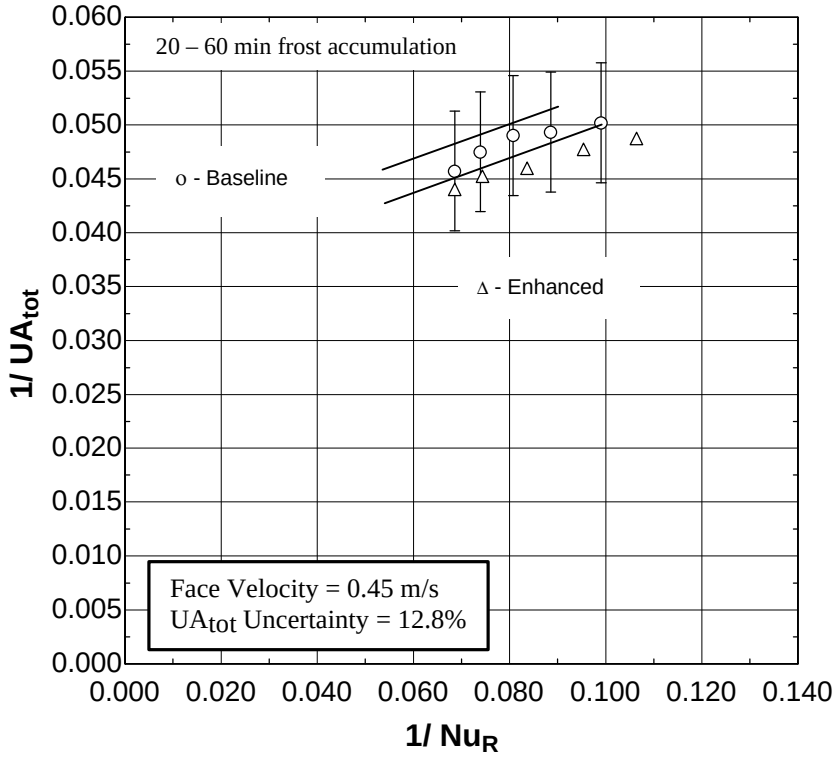

Figure 3.5- A Wilson plot indicating that a small thermal enhancement is possible using two rows of delta wings for Re_{dh} = 510.

The effect of maximum frost accumulation on delta wing performance was also examined using a single row of delta wings at the leading edge. To standardize testing conditions, maximum frost deposition was defined to correspond to frost accumulation yielding a pressure drop of 250 Pa. The observable passage clearance under these conditions was approximately 3mm. The results suggest that a thermal enhancement can be achieved with the addition of delta wings even under maximum frost accumulation. For a face velocity of 1.3 m/s, the thermal resistance was observed to decrease by 10.8% as shown in Figure 3.6, which suggests that the delta-wing enhancement may be tolerant to frost. Because the channel becomes blocked under these conditions and prevents the passage of the vortex through the exchanger, this measured enhancement is believed to be caused by higher frost density downstream of the vortex generator- a phenomenon observed in channel flow [Storey and Jacobi, 1999]. Using this explanation, the conduction resistance of the frost is reduced lowering the overall airside resistance.

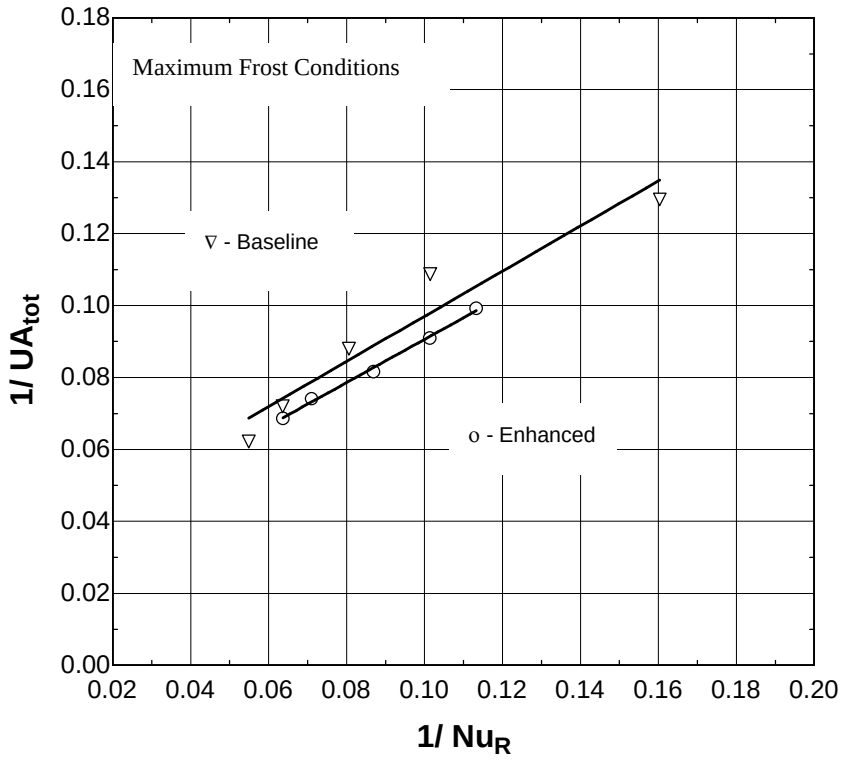

Figure 3.6- A Wilson plot showing thermal enhancement under maximum frost accumulation for Re_{dh} = 490.

3.3 Configuration B (Brazed Evaporator)

This configuration was studied more in depth than the previous one because it isolated the VG effect and promised the greatest heat transfer potential. This configuration was also more reflective of a possible punch-out configuration for a future VG/fin design. Heat transfer data from the evaporator were acquired every 5 minutes following an initial frost growth period of 30 minutes. The following results account for time variations in the hydraulic diameter, minimum free flow area, and channel velocity due to the growing frost layer except for the core pressure drop data which was collected under dry conditions (i.e. no frost). An average Reynolds number, Re_{dh}, was used in some cases to account for these time variations.

3.3.1 Core Pressure Drop Summary

The effect that the additional rows of vortex generators have on the hydraulic performance of the evaporator is shown in Figures 3.7 and 3.8 for dry testing conditions (i.e. no frost formation). The uncertainty in these core pressure drop measurements was ± 0.182 Pa. As can be seen in the figures, the penalty associated with the extra four rows of VGs is small, constituting only an additional 1.5 to 4.6 Pa over the range of Reynolds numbers examined. This penalty corresponds to a maximum increase in the fan power of 0.16W for configurations B and C over the baseline data.

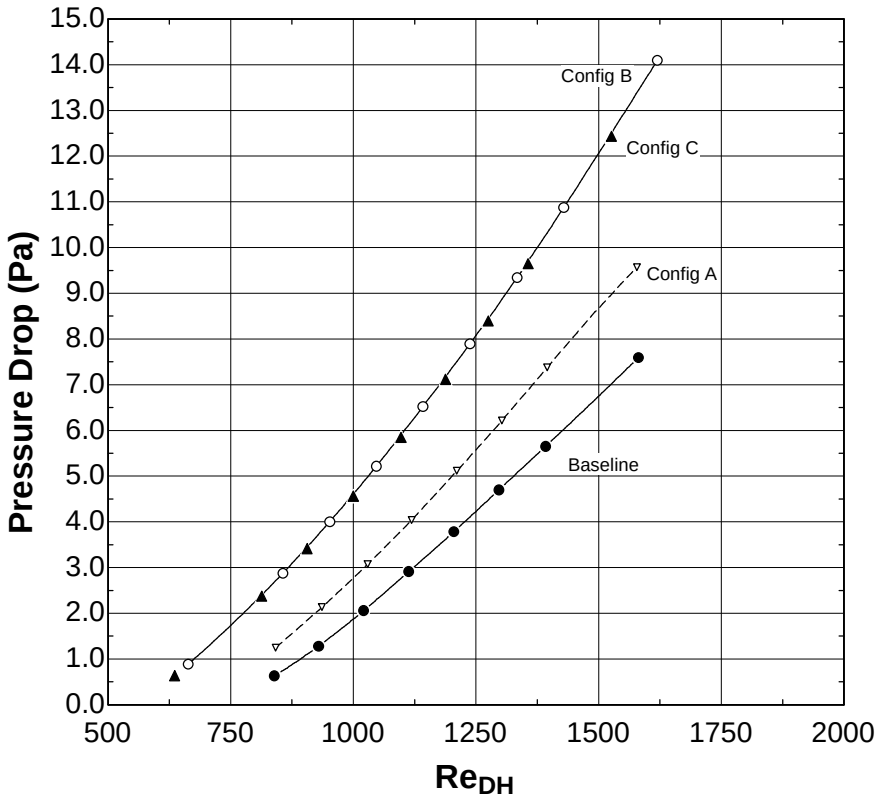

Figure 3.7- The pressure drop penalty associated with the vortex generators is less than 7 Pa over the entire range of Reynolds numbers examined under dry conditions.

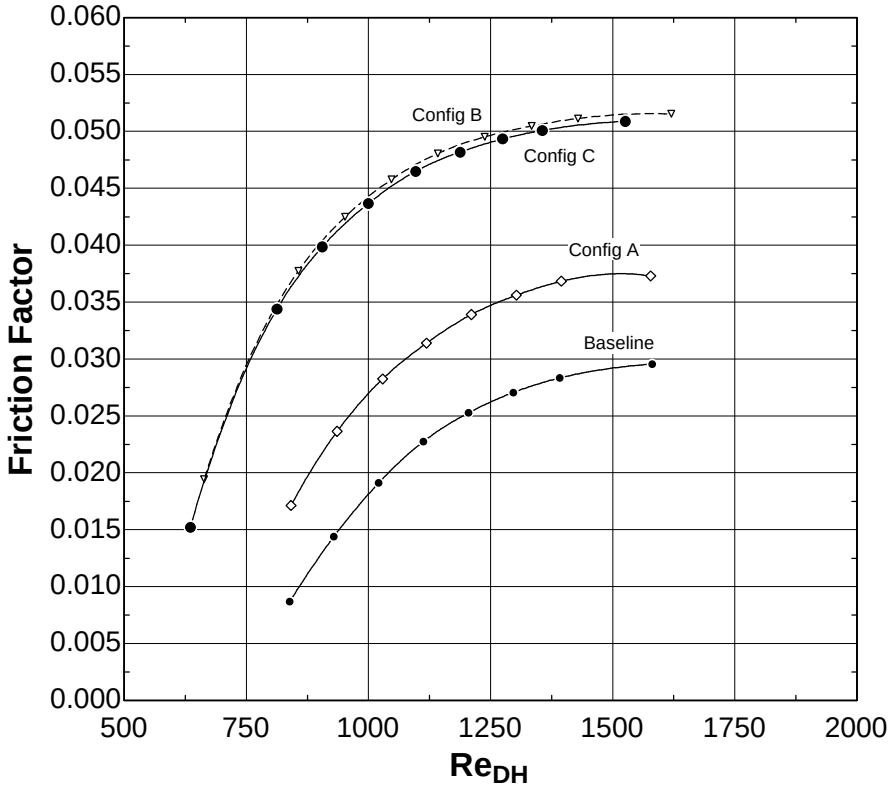

Figure 3.8- The behavior of the friction factor under dry, enhanced conditions is qualitatively similar to the baseline data but is several percentage higher.

3.3.2 Convection Heat Transfer Coefficient

The air-side heat transfer coefficient increased by 55.3 to 84.2% for Reynolds numbers between 500 and 1200 when using the vortex generator array. The value of the air-side heat transfer coefficient varied from 26-51 W/m^2-K for the enhanced configuration and from 16-26 W/m^2-K for the baseline configuration over the tested range. These values were in good agreement with values reported by Ogawa *et al.* [1993] for a plain fin-and-tube heat exchanger of similar geometry with staggered tubes under frosting conditions. Their average heat transfer coefficient varied between 20.9 and 30.7 W/m^2-K. The heat transfer coefficient was also observed to monotonically increase with time as shown in Figure 3.9. This trend was observed for both the baseline and the enhanced cases but was shown to be more pronounced in the enhanced cases where the convection coefficient increased more rapidly with time. This behavior is best explained by recognizing that the air velocity inside each channel increases with time. For the baseline cases, the heat transfer coefficient scales directly and solely with the air stream velocity. In the enhanced cases, however, it is hypothesized that the response of the heat transfer coefficient is proportional to the circulation strength of the introduced vortex, which is a function of not only the air velocity but also of the effective dimensions of the delta wing according to Pohlhamus's [1966] relation

$$\Gamma = K_p \cdot \frac{S\, V_\infty}{2b} \cdot \sin a \qquad [27]$$

for tip vortex circulation from a delta wing. In this equation, K_p is a constant of proportionality that varies with wing aspect ratio, S is the surface area of the delta wing, b is the span of the delta wing, α is the angle of attack, and V_∞ is

the free stream velocity. Because frost deposition affects the effective dimensions of the delta wing, it is conceivable that the vortex circulation strength may have a more pronounced effect on heat transfer in time than the effect of air velocity alone.

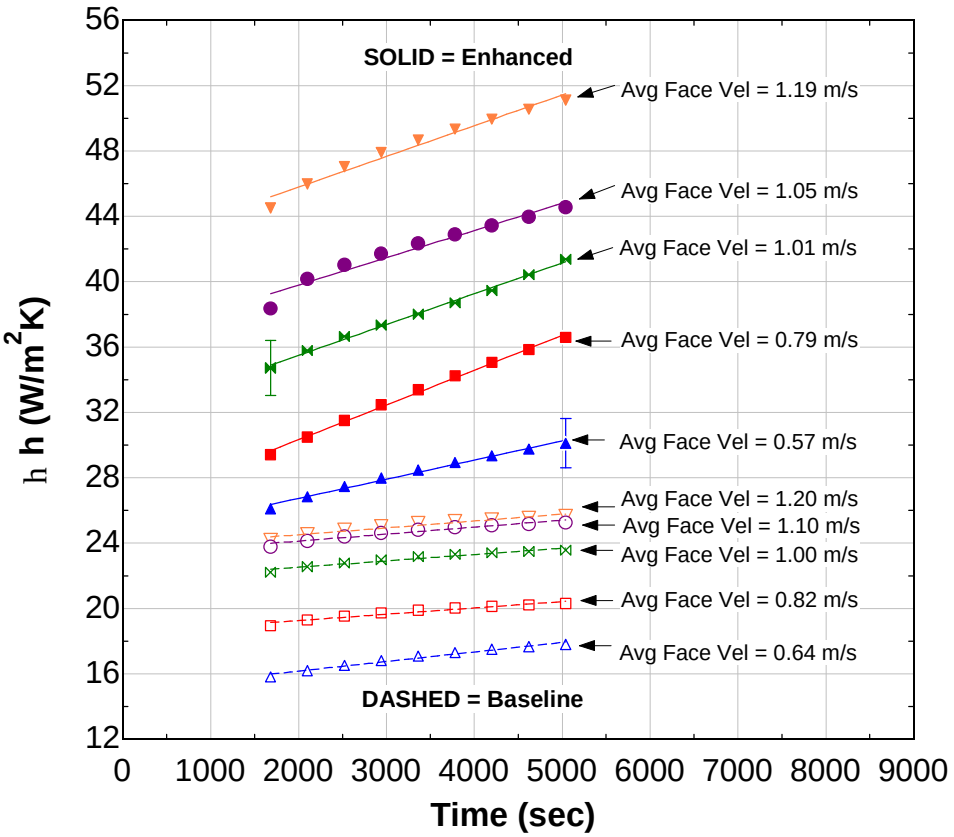

Figure 3.9- The heat transfer coefficient, which is as much as 84% higher for the vortex generator array, is observed to increase with time.

The observed increase in the air-side heat transfer coefficient is best attributed to the growing frost layer and may be explained by a few different mechanisms associated with it. First, the frost layer provides an added roughness to the evaporator, which serves to disrupt the boundary layer growing at the surface. The consequence are higher Nusselt numbers and delayed boundary layer separation from the cylindrical surface of the tube. This may be observed in Figure 3.10 where the frost demarcates the point of boundary layer separation on an evaporator of a slightly different construction. As the frost develops in time and becomes increasingly more dendritic, the location where the boundary layer transitions to turbulent flow gradually begins to shift toward the front of the coil and more of the evaporator experiences a turbulent flow regime. As this happens, the convective coefficient begins to increase. The second mechanism responsible for this overall increase in the heat transfer coefficient is the narrowing of the air passages due to frost buildup while constant total airflow is maintained through the coil as shown in Figure 3.11. The result is an increase in the local air velocity, which thins the boundary layer and causes an increase in the convective coefficient. Third, the porosity of the growing frost layer is large enough to allow the frost to behave as an additional extended surface for heat transfer. In this way, the frost increases the heat transfer surface area of the coil and can produce a small increase in the convective coefficient.

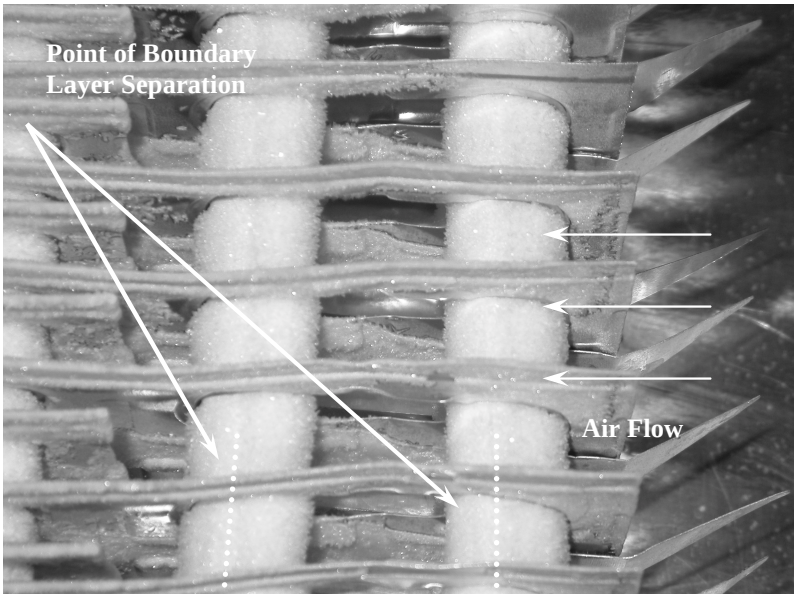

Figure 3.10- Frost growing on an evaporator shows the point of boundary layer separation for the airflow around the tube.

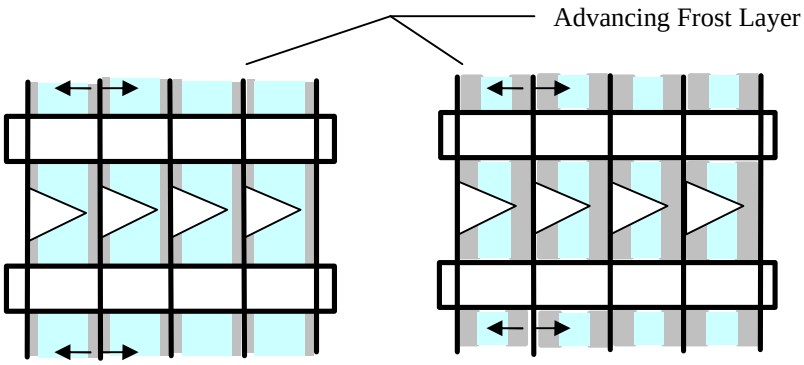

Figure 3.11- This schematic depicts the diminishing free flow area, which is accompanied by an increase in the local air velocity.

3.3.3 Wilson Plot Results

The Wilson plot, which forms the basis for extracting the airside resistance from the overall total thermal resistance, serves as a good contrast between the baseline and enhanced data. First, it is important to note the consistency of the slope of the least-squares regression lines for the plots shown in Figure 3.12 and 3.13. This consistency suggests similar tube-side behavior and therefore good experimental repeatability. This observation is further supported by examining the regression lines for Re_{dh} = 1050 and Re_{dh} = 1060 in Figure 3.13. As expected, the lines nearly coincide. An inverse relationship is also observed between the air-side Reynolds number and the total thermal resistance. As the air-side Reynolds number increases, the thermal resistance decreases, as expected. Finally, the relative compactness of the baseline regression lines should be noted in contrast to the enhanced lines, which are fairly spread out. This fact suggests that the vortex generators reduce the thermal resistance proportional to the airflow rate rather than simply introduce a fixed reduction in thermal resistance.

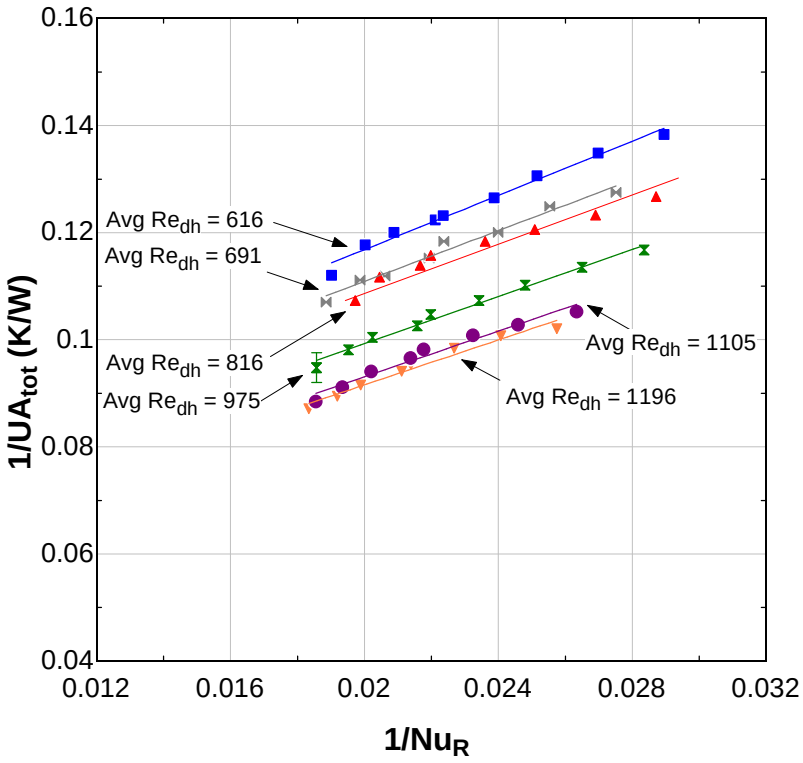

Figure 3.12- Wilson plots of the baseline data for configuration C

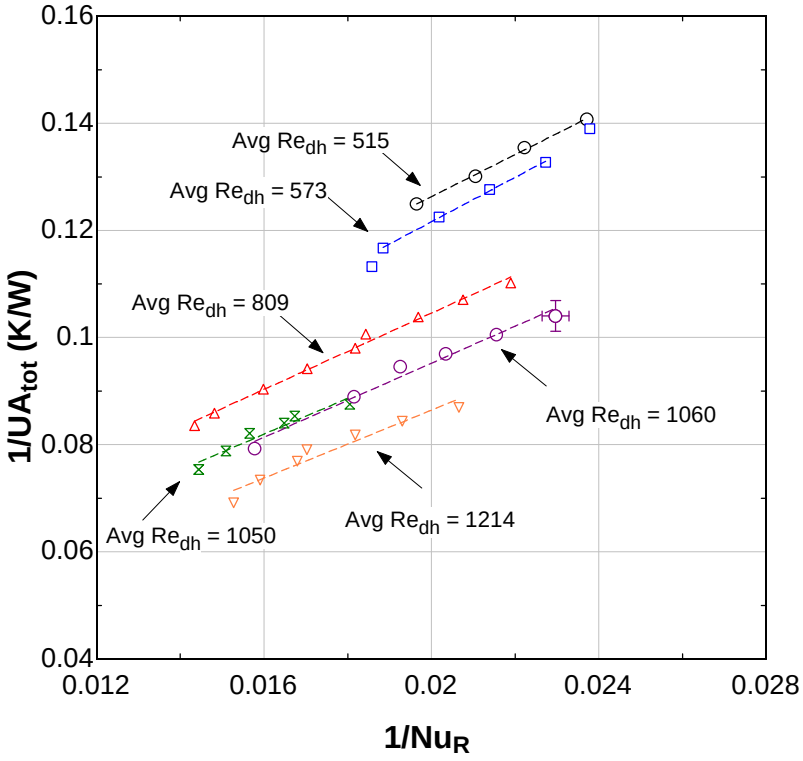

Figure 3.13- Wilson plots of the enhanced data for configuration C

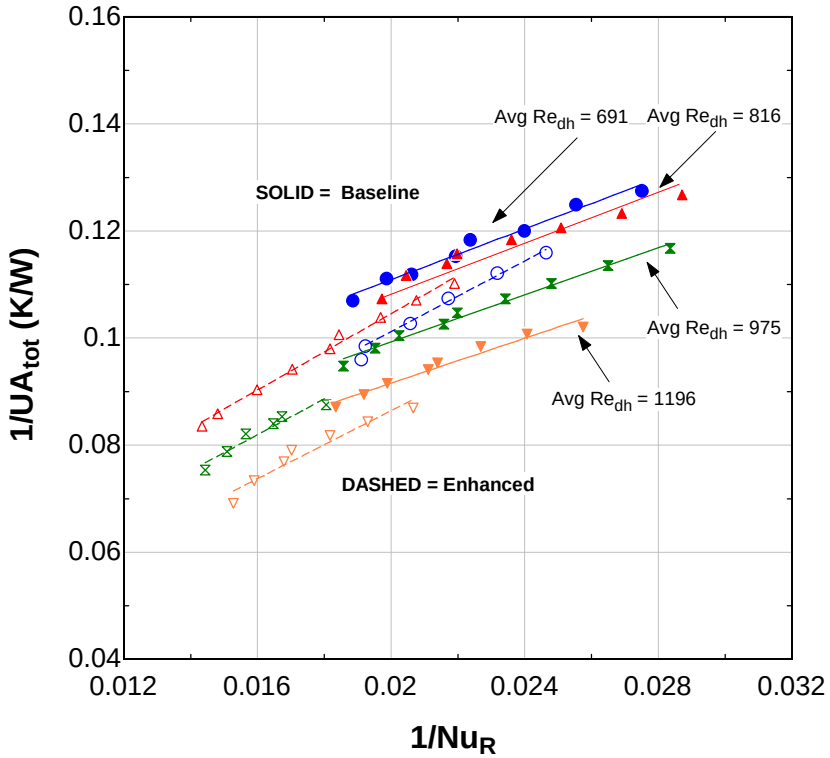

Figure 3.14- These superimposed Wilson plots reveal the benefit of enhancing an evaporator with VGs- a reduction in thermal resistance, $1/UA_{tot}$.

The reduction in the overall thermal resistance is better seen in Figure 3.14 where the baseline data and the enhanced data are plotted on the same graph. In each of the four depicted conditions, the enhanced specimen outperformed the baseline specimen. The change in the slope is probably due to thermophysical property differences in the accumulating frost. Overall, reductions in the total resistance were observed ranging from 10.5% to 27.5%.

3.3.4 Air-Side Thermal Resistance

Once the Wilson plot is generated and a least-squares regression line is fitted through the data, the sum of the air-side convective resistance and the frost conduction resistance is inferred from the y-intercept. At this location, the tube-side resistance is zero by definition, and the conduction resistance is everywhere negligibly small. To simplify the analysis, the frost resistance can be added to the convective resistance to form an overall air-side thermal resistance, which is plotted in Figure 3.15. For Re_{dh} = 500-1200, a consistent reduction of 35.0% to 42.1% was observed for the enhanced evaporator.

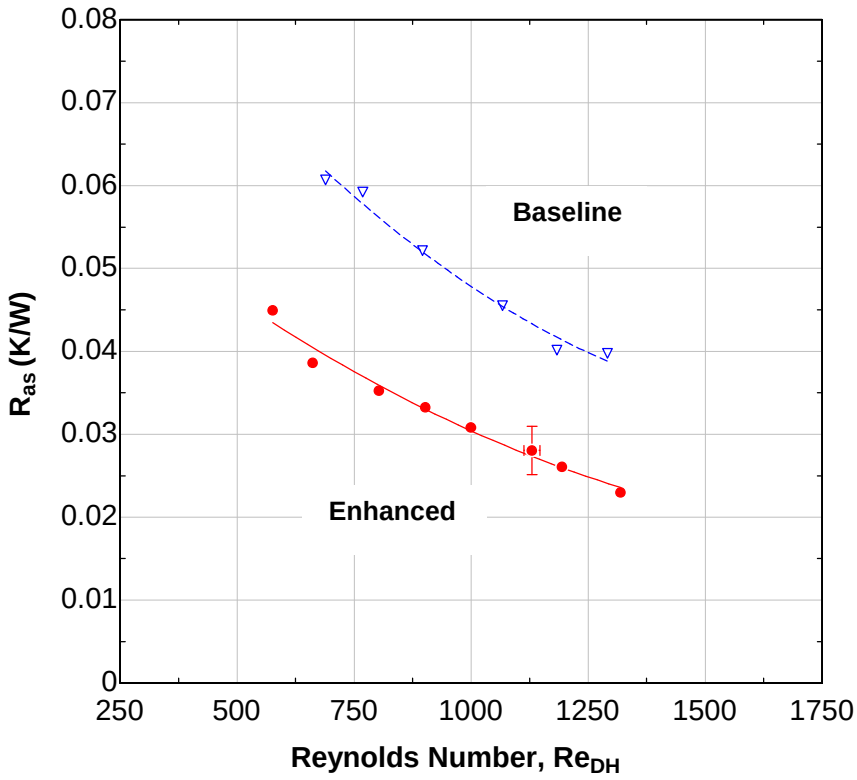

Figure 3.15- The overall air-side thermal resistance is 35% to 42% lower for the enhanced evaporator.

These resistance values are significantly higher than those reported by El Sherbini [2000] for a brazed evaporator of similar construction. The air-side resistances of his baseline data varied from 0.013–0.018 K/W over a similar range of Reynolds numbers. These discrepancies can be explained by recognizing that his fin pitch was nearly half of the current one being studied, and his tests were all conducted under dry conditions (i.e. no frost). The presence of frost on the heat exchanger has been shown to contribute a conduction resistance up to 0.012 K/W.

3.3.5 Performance Evaluation Criteria

3.3.5.1 London Area-Goodness Factor

The London area-goodness factor, which is defined as the ratio of the *j*-Colburn factor over the friction factor, is commonly used to assess the thermal hydraulic performance of a heat exchanger. Because heat transfer enhancements are often accompanied by increased frictional forces in the air flow, the *j/f* ratio is useful as a simple evaluation of the relative differences between these effects and comparing one exchanger to another. For these reasons, higher *j/f* ratios equate with better performance. As seen in Figures 3.16 and 3.17, the baseline data showed much more consistent trends than the enhanced data.[*] However, some general observations can be made about both plots. The London area-goodness factor was observed to decrease with time, agreeing with the idea that frost is a "fouling" agent that degrades the performance of an evaporator. As frost began accumulating on the exchanger, the thermal performance slowly decreased while the frictional forces increased. Although more obvious in the baseline data, the London area-goodness factor was inversely proportional to the air flow rate. At low face velocities, the

[*] The fin efficiency, η, is taken as unity for these plots but was calculated to range from 85% to 90% for the data obtained in this study.

evaporator carried a high *j/f*; where, at high face velocities, *j/f* was reduced. This fact suggests that at higher air flow rates, the rise in core pressure drop due to the delta wings was more significant than the provided benefit. One final observation can be made concerning the relative magnitude of *j/f* for the baseline data versus the enhanced data. It was observed that the enhanced data generally begin their decay at a higher initial *j/f* than the baseline data do. This observation suggests that the vortex generator array is capable of producing higher *j/f* values than the baseline. It should also be noted that *j/f* for the baseline data decays at a faster rate than that for the enhanced data and appears to asymptotically approach a final value. The baseline data reach this final value much sooner than the enhanced data do.

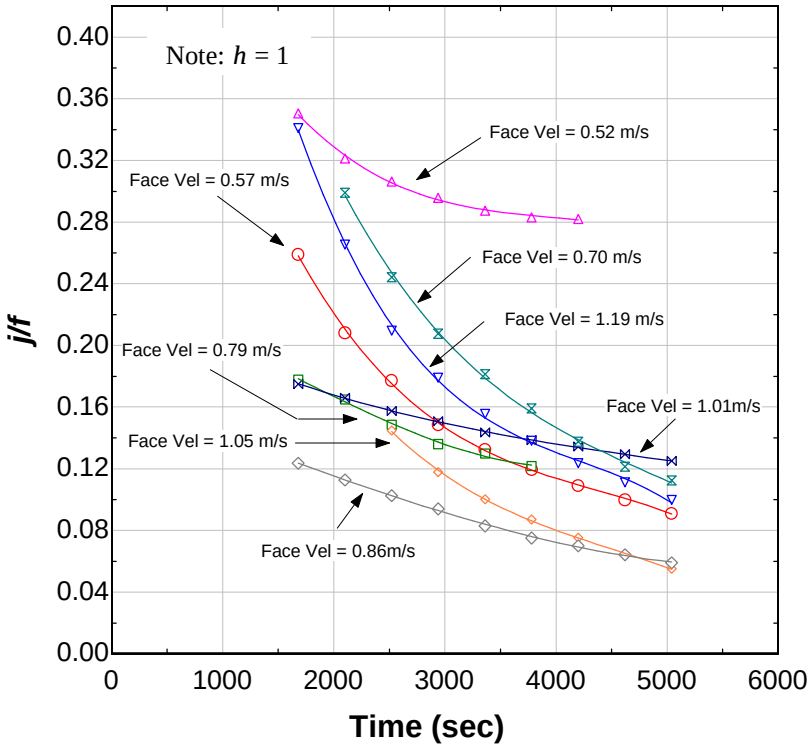

Figure 3.16-Curves of *j/f* for the enhanced data decreased in time.

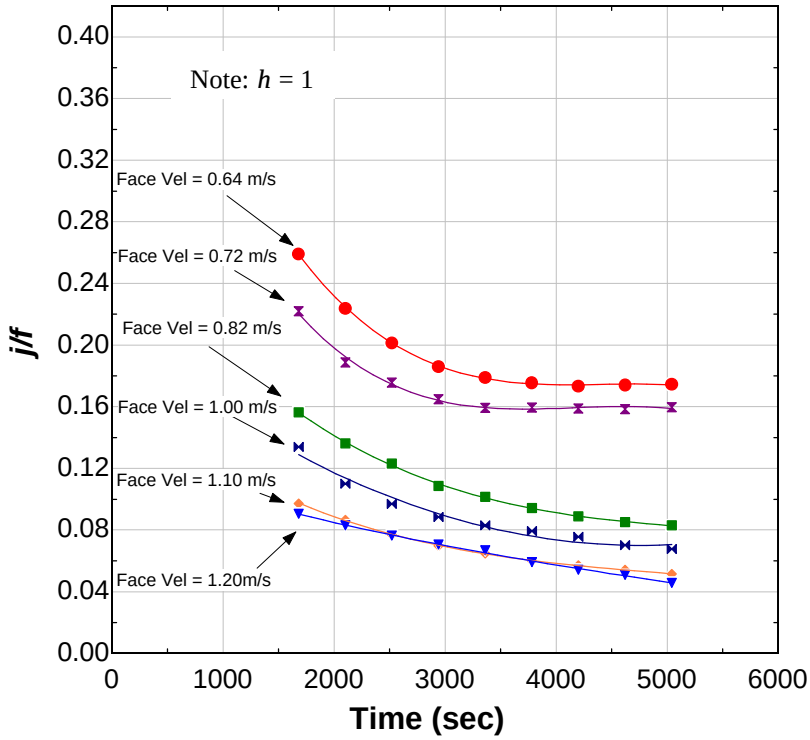

Figure 3.17-Curves of *j/f* for the baseline data also decreased in time with the highest values coming at the lowest face velocities.

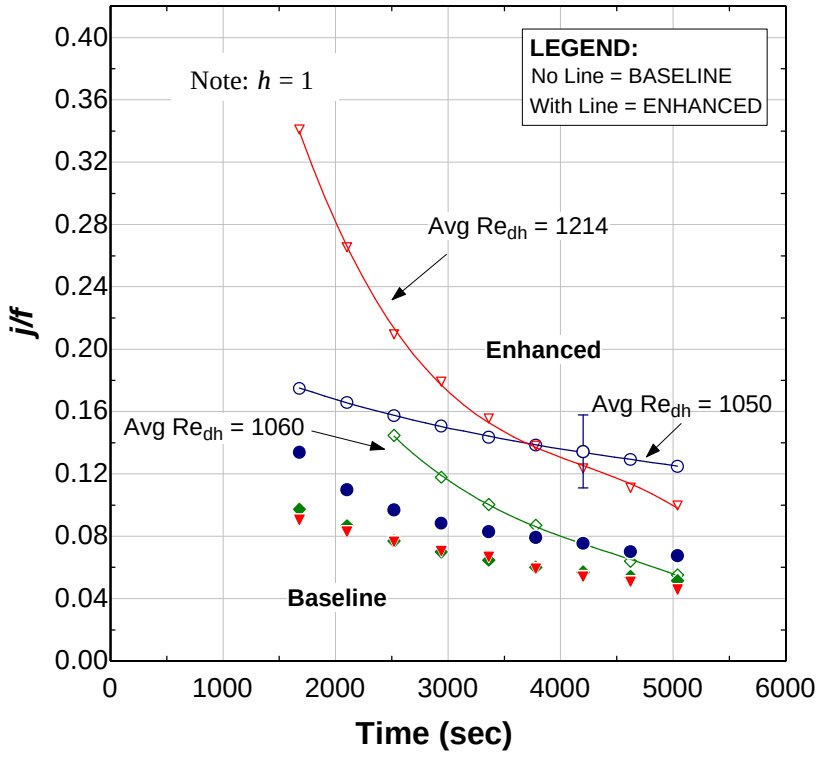

(a) High Reynolds numbers

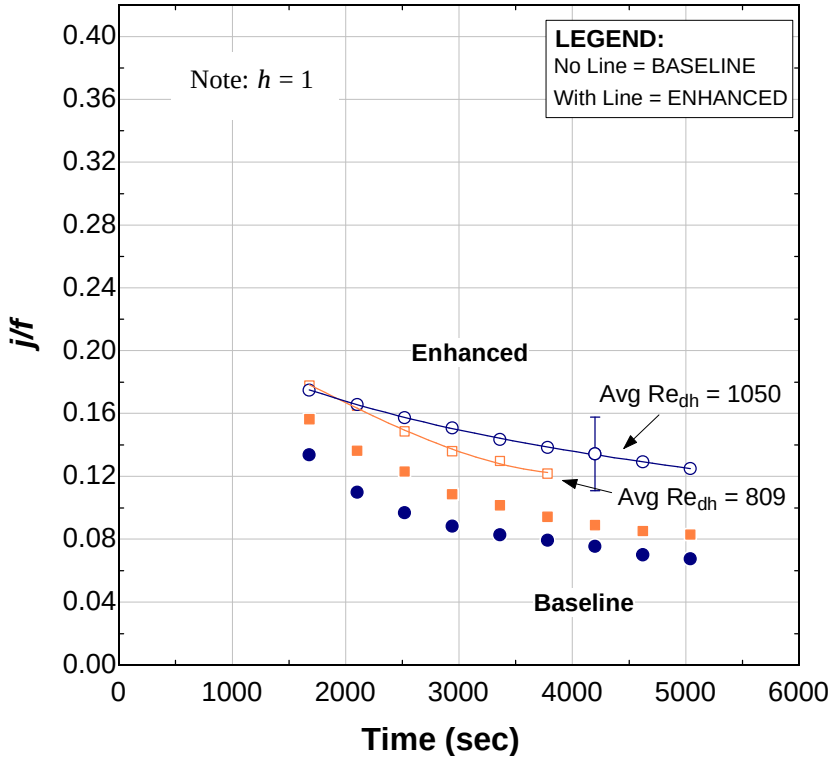

(b) Moderate Reynolds numbers

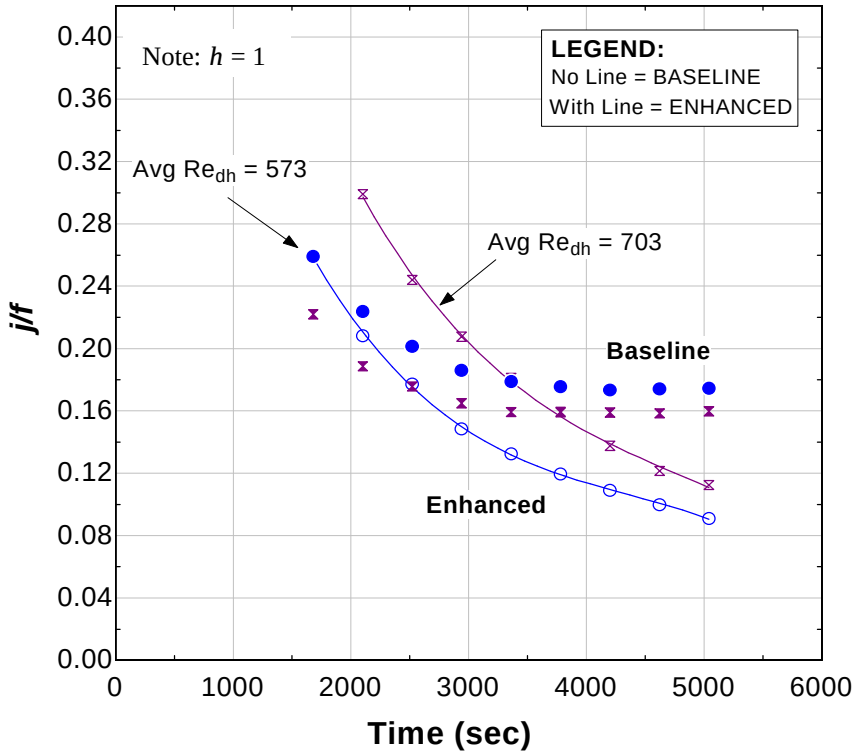

(c) Low Reynolds numbers

Figure 3.18- Superimposed London area-goodness curves suggest the presence of a critical Reynolds number for operation at approximately 700-750.

Superimposing the London area-goodness factor curves for the baseline data and the enhanced data on the same plot reveals some further interesting results as can be seen in Figure 3.18. For $Re_{dh} \geq 809$, the enhanced data consistently outperform the baseline data using this PEC. At $Re_{dh} = 703$, the baseline data start with a lower *j/f* factor than the enhanced data but end up surpassing the enhanced data to finish with a greater *j/f* factor. For $Re_{dh} = 573$, the baseline data are everywhere superior to the enhanced data. This fact suggests that an optimal Re_{dh} exists for determining when to use this particular VG array. According to this PEC, this critical Reynolds number appears to be approximately 750. The uncertainty in *j/f* was approximately ±0.023, or 17.4%.

The London area-goodness factor was also examined directly as a function of the Reynolds number at specific instances in time. In this way, the evolution of j/f can be better traced in time and a more readable comparison between the enhanced and the baseline evaporators can be made. In Figures 3.19-3.21, the j/f factor is plotted against the air-side Reynolds number after 30min, 60min, and 90min of frost growth.

The first general observation that can be made concerns the nature of the transient decays. The baseline data decay and asymptotically approach a value near zero. The enhanced data decay, reach a minimum value, and then begin to increase again. This local minimum is best understood to be the flow condition at which the enhanced evaporator begins to outperform the baseline evaporator. The evolution of this flow condition should also be noted in time. After 30 minutes of frost growth, this Reynolds number is approximately 1000. After 60 minutes of sustained frost growth, this local minimum occurs at a Reynolds number of approximately 950. And after 90 minutes of growth, it shifts yet further to a Reynolds number of about 900. This gradual shift of the local minimum is best explained by considering that the hydraulic diameter is decreasing in time. Because each experiment was maintained at a constant blower setting, as this characteristic length scale decays in time, the local channel velocity increases due to the contracting area. This increase in velocity, however, does not completely offset the decrease in hydraulic diameter. As a result, the formation of a coherent vortex structure shifts to lower Reynolds numbers with time.

A second observation that can be made is that the baseline data and the enhanced data fall nearly on top of each other until this local minimum is reached. This behavior may suggest that the additional flow mixing due to the VGs is directly offset by the added pressure penalty at these low Reynolds numbers. It is not until the vortex structure becomes coherent and well defined at a Reynolds number around 900 that the relationship between the thermal performance and the pressure drop ceases to be linear and a net thermal enhancement is realized.

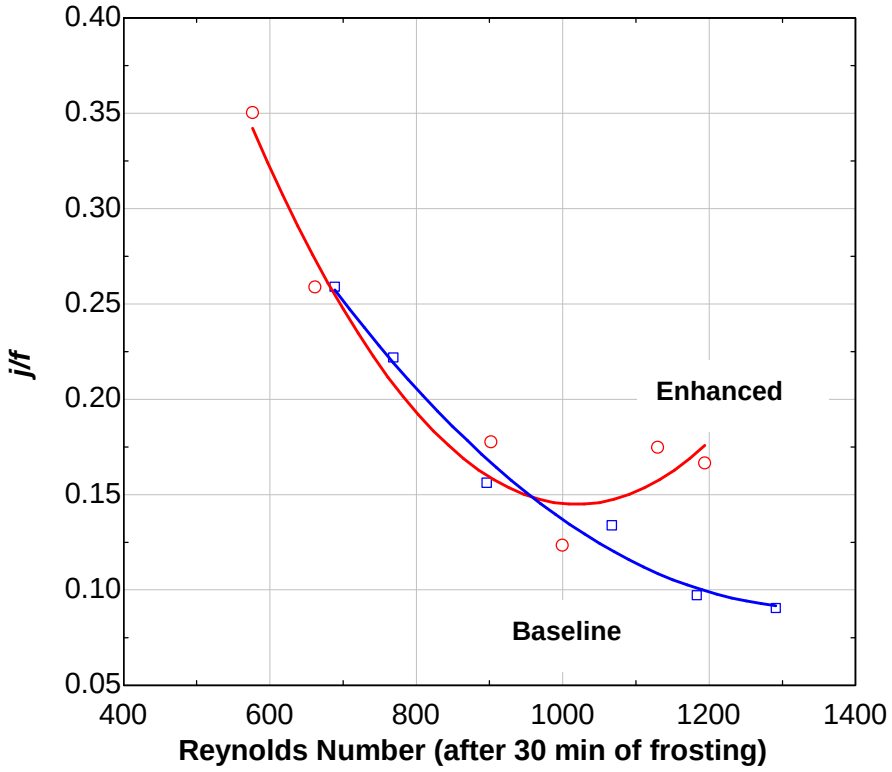

Figure 3.19-The London area-goodness factor after 30 minutes of frosting

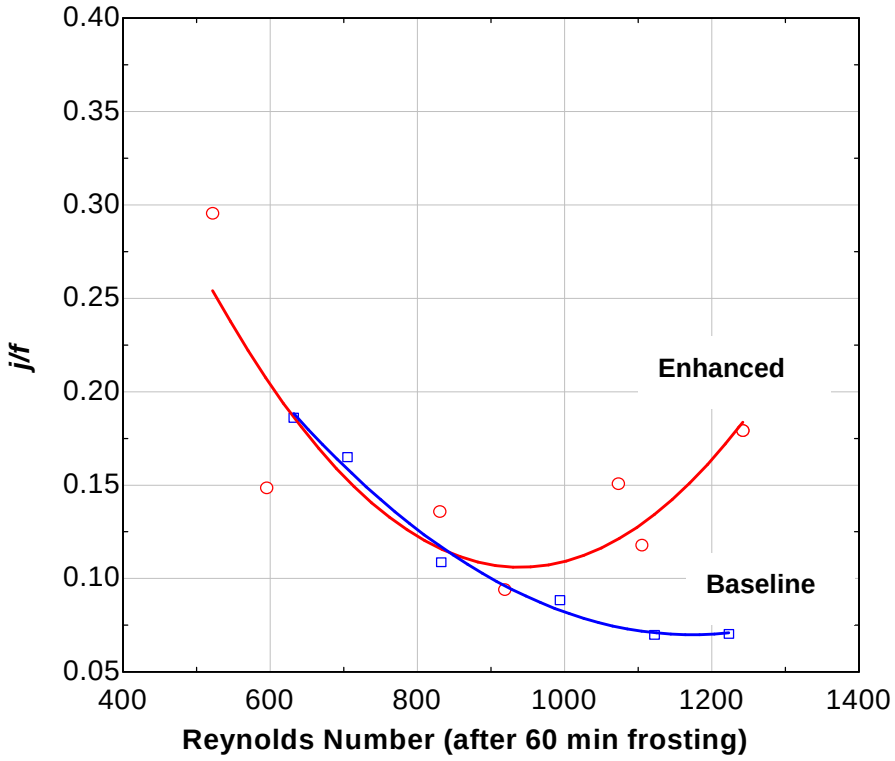

Figure 3.20-The London area-goodness factor after 60 minutes of frosting

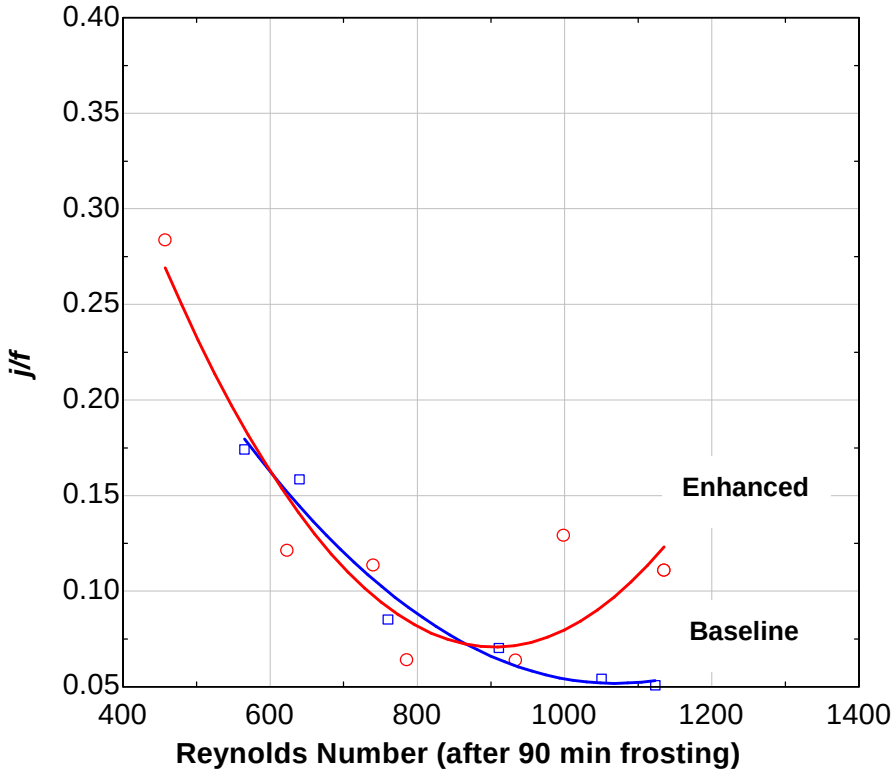

Figure 3.21- The London area-goodness factor after 90 minutes of frosting

3.3.5.2 Modified Volume-Goodness Factor

A second performance evaluation criterion, Θ, which is often used to compare different heat exchanger designs, is the ratio of heat transfer divided by core volume and the log-mean enthalpy difference. In this way, this PEC serves as a modified volume-goodness factor and is formally defined as

$$\Theta = \frac{Q_{air}}{(V \cdot \Delta h_{lm})} \ , \qquad [28]$$

where Q is the airside heat transfer, V is the heat exchanger core volume, and Δh_{lm} is the log-mean enthalpy difference. As can be seen in Figure 3.22 for the enhanced case and in Figure 3.23 for the baseline case, the data exhibit a few identifiable trends. First, the thermal hydraulic performance increases with increasing Reynolds number- an observation consistent with expectation. This simple fact confirms that heat transfer occurs in a larger quantity at higher air flow rates. Second, it is important to note that the performance decreases in time as frost accumulates on the evaporator. This degradation is also consistent with what was observed using the London area-goodness factor and emphasizes the frost layer as an additional thermal resistance. Third, the deterioration in thermal performance with time is more pronounced at lower Reynolds numbers. This fact suggests that the properties of the growing frost layer are different at lower Reynolds numbers than at higher Reynolds numbers and corroborates other data, which has suggested that the frost is more dendritic at lower air flow rates. Dendritic frost, of course, poses a greater conduction resistance than dense frost and might degrade the thermal performance more rapidly, which would explain this trend.

In Figure 3.24, the baseline data and the enhanced data are superimposed on each other for direct comparison and easier readability. It is immediately observable that, unlike the London area-goodness factor comparison, this comparison shows the VG array appears to be beneficial over the entire range of face velocities examined. The net enhancement in the volume-goodness factor was 16.7% to 32.9% over the range of face velocities tested. It is also apparent that at low face velocities the magnitude of the difference between the baseline and enhanced data is diminished suggesting a gradual coalescence of the two data sets as the face velocity approaches zero. The maximum uncertainty in the modified volume-goodness factor was approximately 1.8%

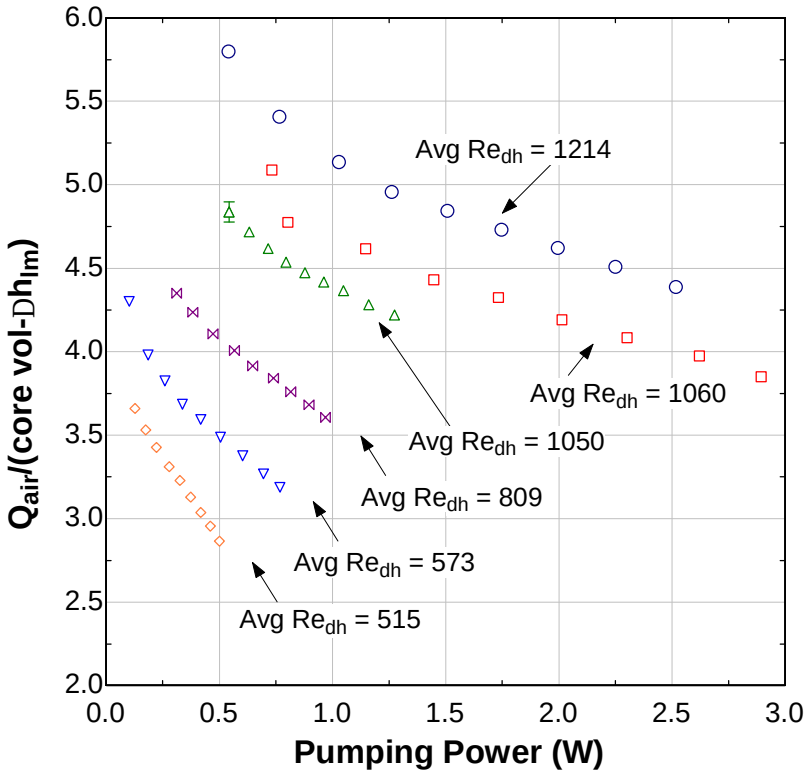

Figure 3.22- The modified volume-goodness factor for the enhanced data

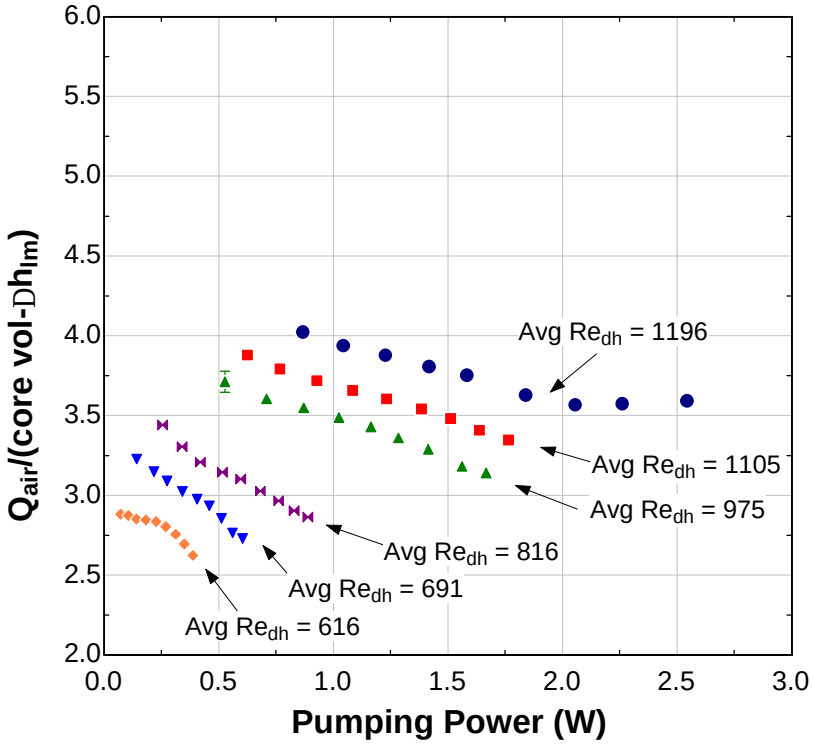

Figure 3.23- The modified volume-goodness factor for the baseline data

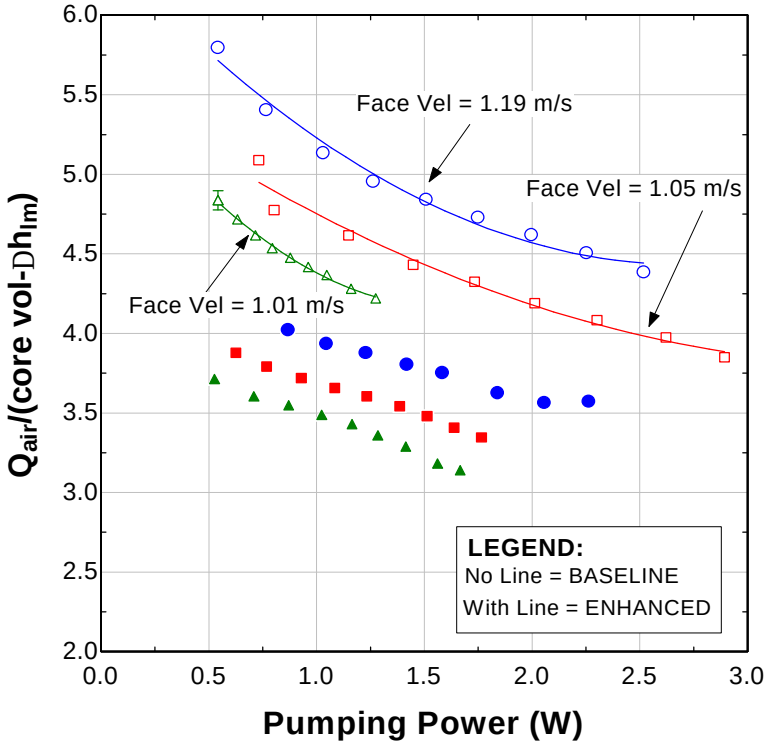

(a) High face velocities

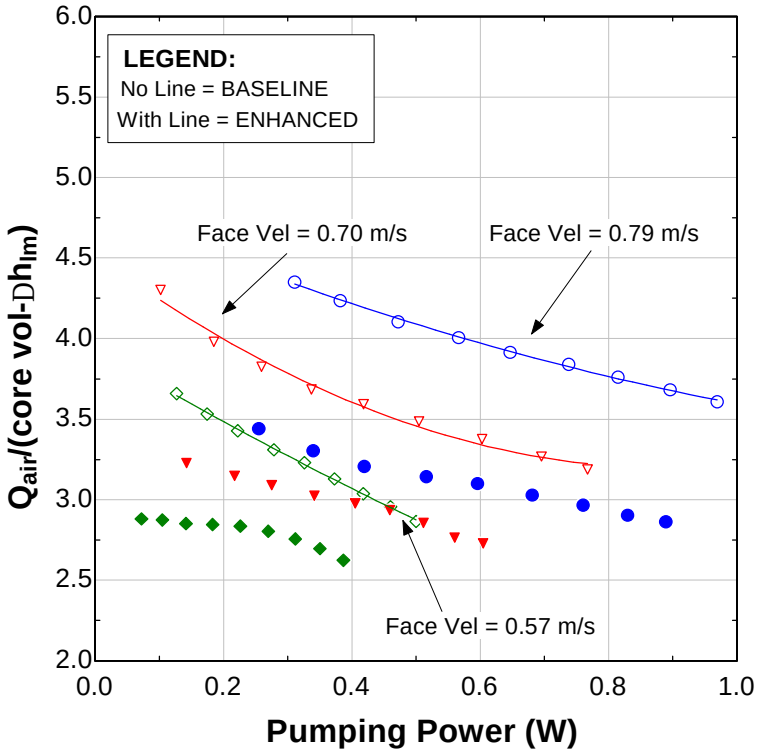

(b) Low face velocities

Figure 3.24- Superimposed volume-goodness curves show that the enhanced data are everywhere superior to the baseline data.

3.3.6 Stanton Number

The Stanton number, another dimensionless parameter that is sometimes used because of its role in the mass and heat transfer analogy, is defined as

$$St = \frac{\mathrm{Nu}_{Dh}}{\mathrm{Re}_{Dh}\,\mathrm{Pr}} = \frac{h}{r\,Vc_p}\ , \qquad [29]$$

where ρ, c_p, and V describe the density, specific heat, and velocity of the air stream. In this way, the Stanton number scales the dimensionless temperature gradient at the evaporator surface with the properties of the flow and serves as a modified Nusselt number. It also provides additional insight into the behavior of the vortex generator. Interestingly, the data are nearly constant over the entire range of Reynolds numbers tested for both the enhanced and the baseline specimens as seen in Figure 3.25. The enhancement observed for these flow conditions is approximately 76%. The scatter in the data is due to the compilation of several individual experimental runs under slightly different test conditions.

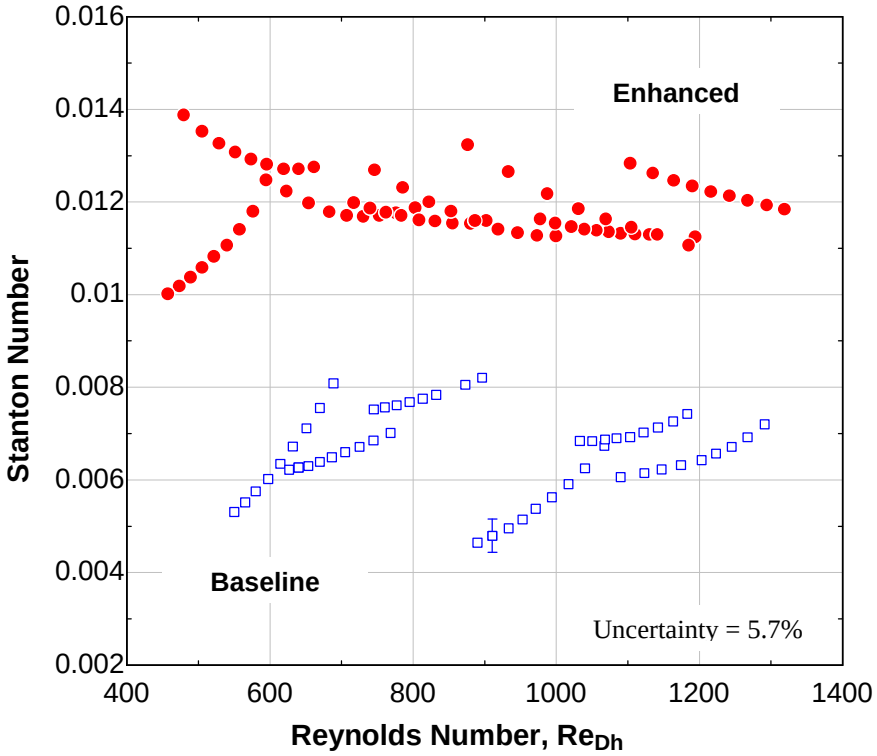

Figure 3.25- A comparison of the Stanton numbers for the baseline and the enhanced data with the fin efficiency taken as unity.

3.3.7 Frost Density

The density of the generated frost can also serve as an important criterion when evaluating heat exchangers because of its integral role in determining the conduction resistance through the frost layer. In short, the denser the generated frost, the smaller the conduction resistance. Therefore, evaporators that promote the generation of a denser frost are usually desired because of their longer associated operational cycle.

Below in Figures 3.26 and 3.27, two different plots of frost density are shown versus the air-side Reynolds number. The density in Figure 3.26 is an average frost density calculated using the total known mass deposition of

the frost, the total surface area, and the thickness of the frost layer. Using this approach, the density of the frost on the enhanced evaporator is noticeably greater than the density of the frost on the baseline evaporator. This fact suggests that the passively generated vortex aids in the production of denser frost. On average, the frost accumulating on the enhanced evaporator is 32 kg/m^3 denser than that on the baseline specimen, which corresponds to a 16.5% to 53.4% increase in frost density. This phenomenon is probably due to the flow behavior in the downwash region behind the vortex generator. Here the rotational flow suppresses the axial growth of frost spires and promotes dendritic branching instead.

In Figure 3.27, the density is calculated from the Hayashi [1977] correlation

$$r_{frost} = 650\exp(0.277 \cdot T_s) \ , \qquad [30]$$

using the frost substrate temperature, T_s, extracted from the log-mean humidity ratio driving potential method and the following equation:

$$\dot{m}_{frost} = \frac{h_o}{c_{p,air}} A_{tot} Le^{-2/3} \Delta\nu_{lm} \ , \qquad [31]$$

where ϖ_{lm} is the log-mean humidity ratio difference. Again it can be seen that for any Reynolds number, the enhanced evaporator exhibits a denser frost than the baseline specimen does. It should also be noted that the two calculated frost densities are similar to within 15-20% over the entire range of examined Reynolds numbers. The higher observed frost densities of the enhanced evaporator are consistent with observations made by Jacobi and B.D. Storey [1997] for vortex generation in a simple channel flow.

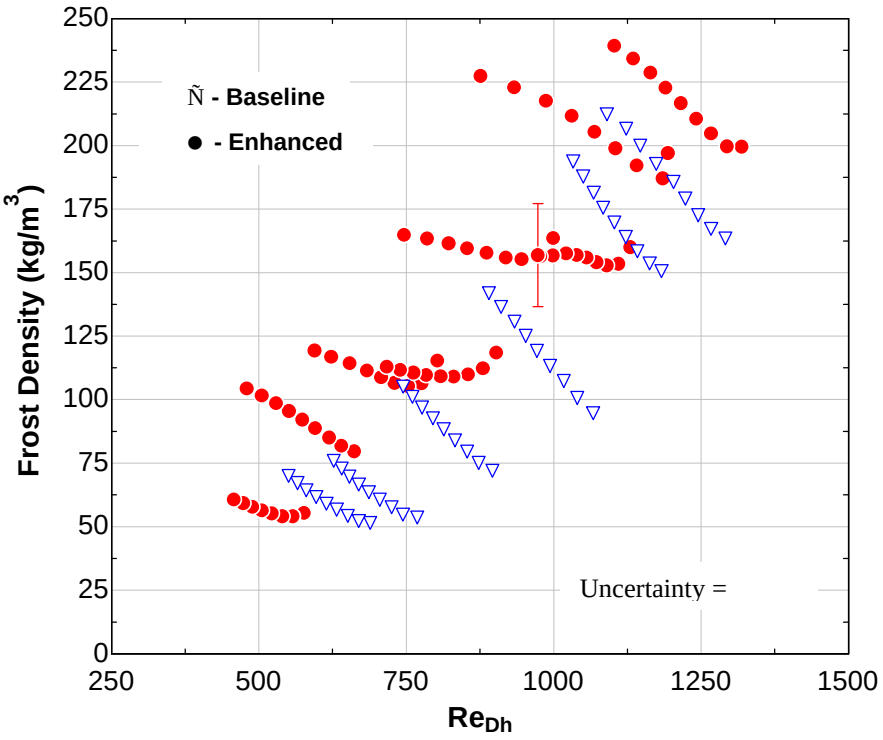

Figure 3.26- Frost density calculated using measured mass deposition rate data

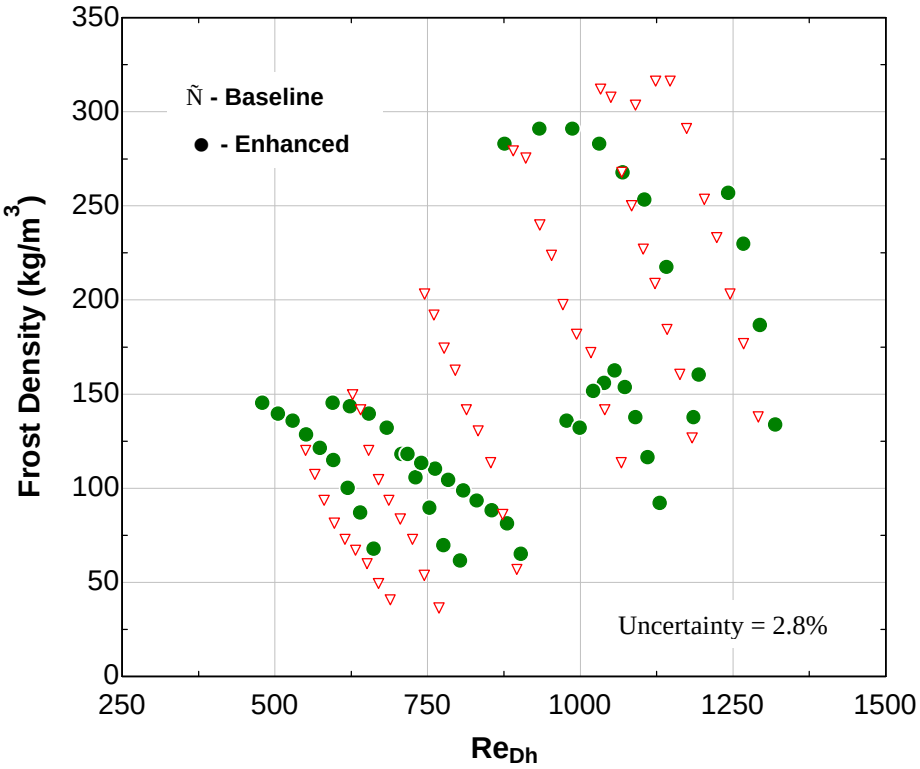

Figure 3.27- Frost density calculated using the Hayashi [1977] correlation

3.3.8 Frost Thickness

The average frost thickness, which is intrinsically related to the frost density, is shown below for the baseline data and the enhanced data. Using Hayashi's [1977] correlation for frost density, the frost thickness is calculated numerically by integrating the mass deposition rate with respect to time. As expected, the baseline data suggest the presence of a thicker, more dendritic frost layer. In fact, on average, the frost layer of the enhanced evaporator is calculated to be 0.36 to 0.76 mm thinner than the frost layer of the baseline evaporator, which corresponds to a 19.8% to 27.7% decrease in frost thickness. These results are shown below in Figures 3.28-3.31.

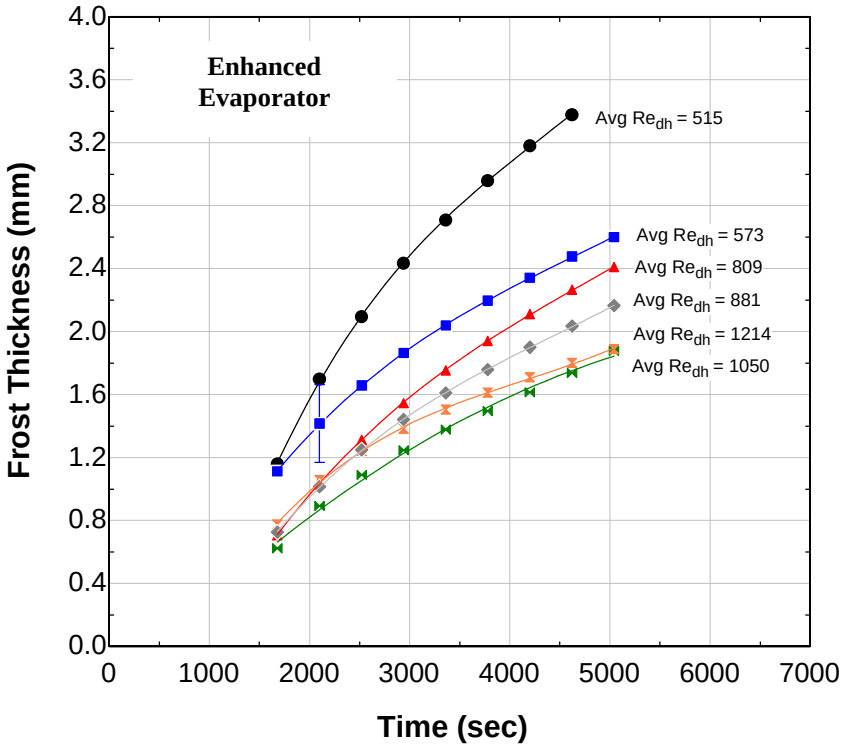

Figure 3.28- Frost thickness profiles for the enhanced data

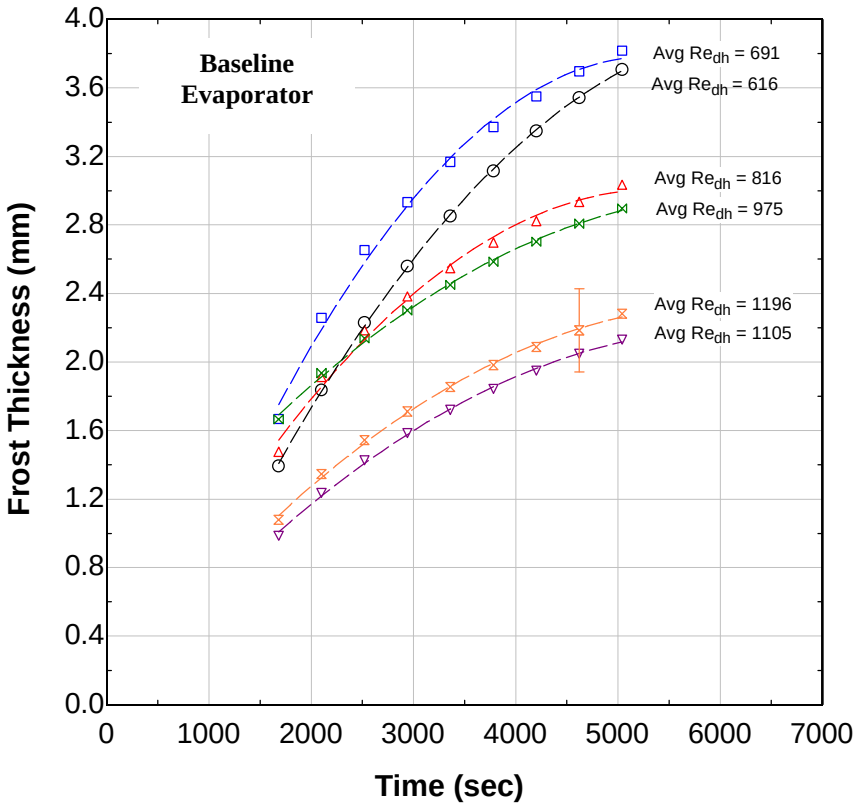

Figure 3.29- Frost thickness profiles for the baseline data

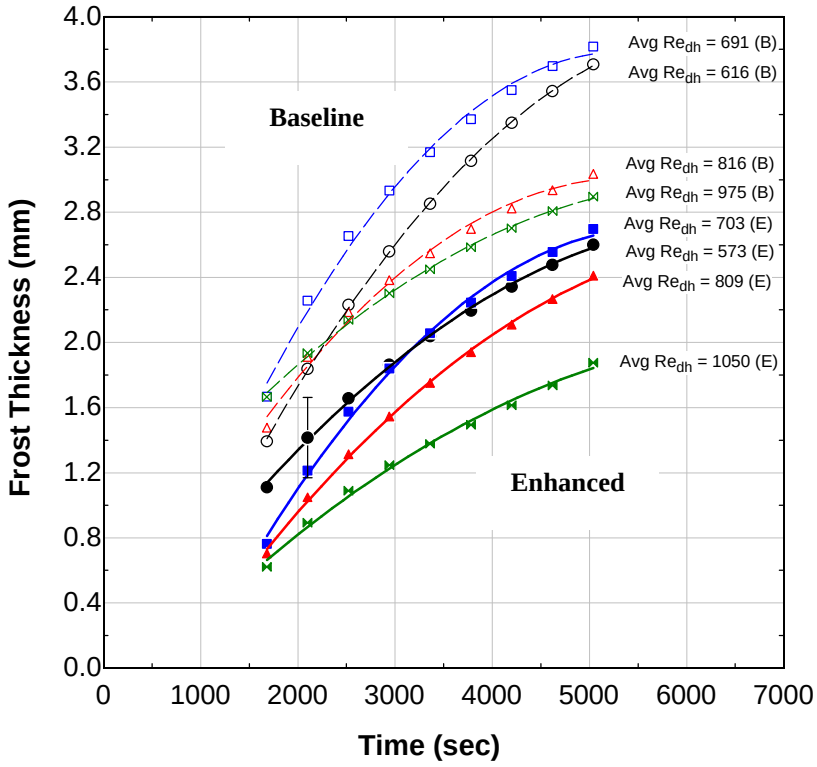

Figure 3.30- A comparison of the frost thickness data reveals a thicker frost layer associated with the baseline case.

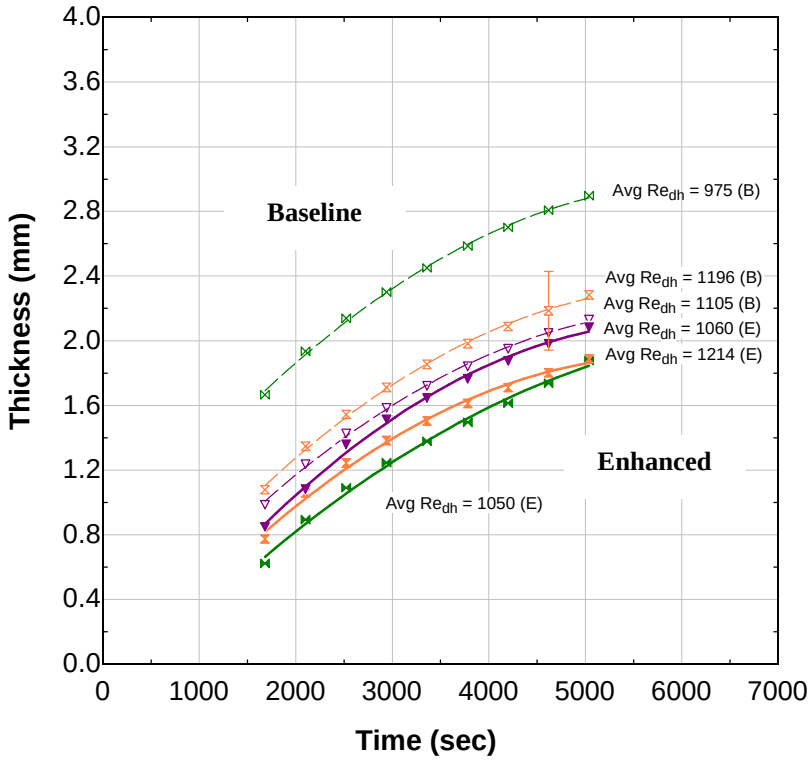

Figure 3.31- A magnification of the frost thickness differences between the baseline data and the enhanced data in the range of higher Reynolds numbers

In order to compare the data of this study to earlier modeling, the work of Storey and Jacobi [1997] for laminar channel flow is adopted, in which the following equations are used:

$$\frac{d_f}{F_p} = \sqrt{\frac{Fo \cdot Bi \cdot \Phi}{Le^{2/3}}} \quad [32]$$

$$Fo = \frac{K \cdot t}{c_{p,air} F_p^{\ 2}} \quad [33]$$

$$Bi = \frac{h \cdot d_f}{k_f} \quad [34]$$

$$\Phi = \frac{r_{v,\infty} - r_{v,s}}{r_a} \quad [35]$$

where F_p is the fin pitch/channel height, Fo is the Fourier number, Bi is the Biot number, and K is an empirical constant determined by Storey and Jacobi to be 0.00087 Wm^2/kgK. Applying these equations to the baseline data for a face velocity of 0.82 m/s, the frost thickness was predicted to be 2.38 cm after 5000 seconds as compared to the measured frost thickness of 3.12 cm inferred using Equation [6] and [14] – [15] at this instance in time- a difference of 23.9%. Similarly, using the baseline environmental data for the case of a face velocity of 1.20 m/s, the frost thickness predicted by Storey and Jacobi's model after 5000 seconds was 2.62 cm compared to "actual" numerically grown frost thickness of 2.38 cm- a difference of only 10.1%. These simple calculations support the idea that numerical integration of mass deposition rate data is a sufficient and satisfactory way to calculate frost thickness.

3.3.9 Maximum Frost Accumulation

The vortex generator configuration was also tested under a "maximum" frost condition which was arbitrarily defined to be the point at which the accumulating frost generates a core pressure drop equal to 62.2 Pa (0.25-in H_20). Passage clearance is now on the order of 1-2mm as observed in Figure 3.32. The maximum frost condition was reached after 81 minutes for the baseline data and after only 57 minutes for the enhanced data. More time was needed for the baseline evaporator to reach the maximum frost condition due to the absence of the vortex generators, which had contributed to the pressure drop in the enhanced data.

The frost structure behind a vortex generator can be seen in Figure 3.33. The view shown is taken looking down a fin in the flow direction directly behind the vortex generator placed at the leading edge. In these images, a "trough" region appears directly behind the delta wing in the downwash region of the vortex. This frost appears to be denser and more compact than the frost on the periphery. This qualitative observation is further corroborated in Figure 3.34, which is a side view of the picture shown in Figure 3.33. Here the dendritic structure of the frost is more clearly seen on either side of the delta wing adjacent to the tubes. These pictures support the data which suggest that denser frost exists downstream of the vortex generator.

As was observed earlier in Configuration A, the vortex generator appears to offer thermal enhancement even under the condition of maximum frost accumulation. This phenomenon was observed again for Configuration C. The thermal benefit, although somewhat diminished, was still evident as shown in Figure 3.35. If the linear

regression analysis performed here were extrapolated to zero tube-side resistance, the reduction in total thermal resistance would still be on the order of 25%.

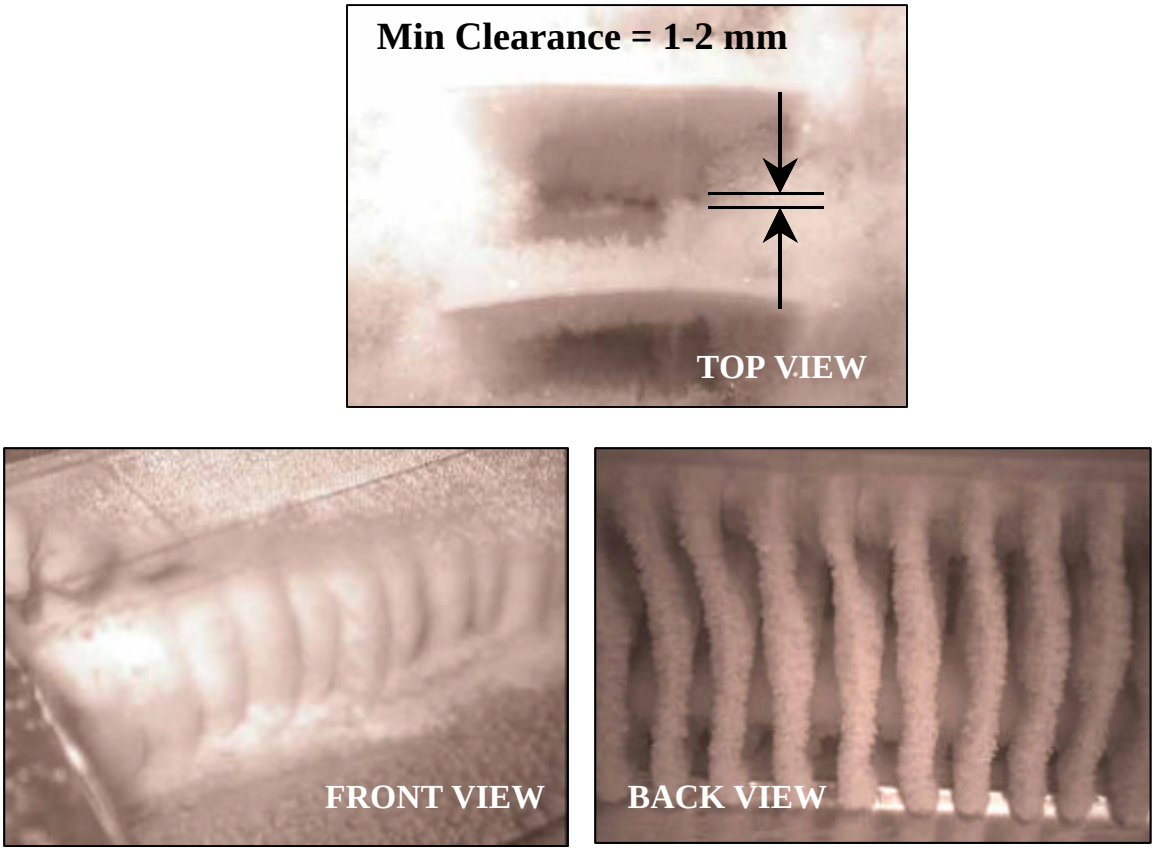

Figure 3.32- Pictures taken after experimentation show the narrowness of the passage during the maximum frost condition.

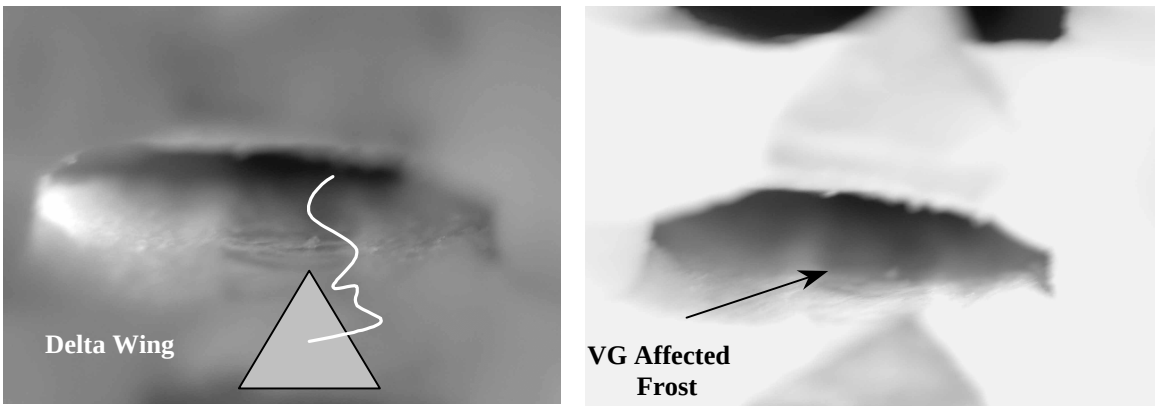

Figure 3.33- A “trough” region behind the vortex generator is apparent in these photographs, suggesting the presence of a shallower, denser frost.

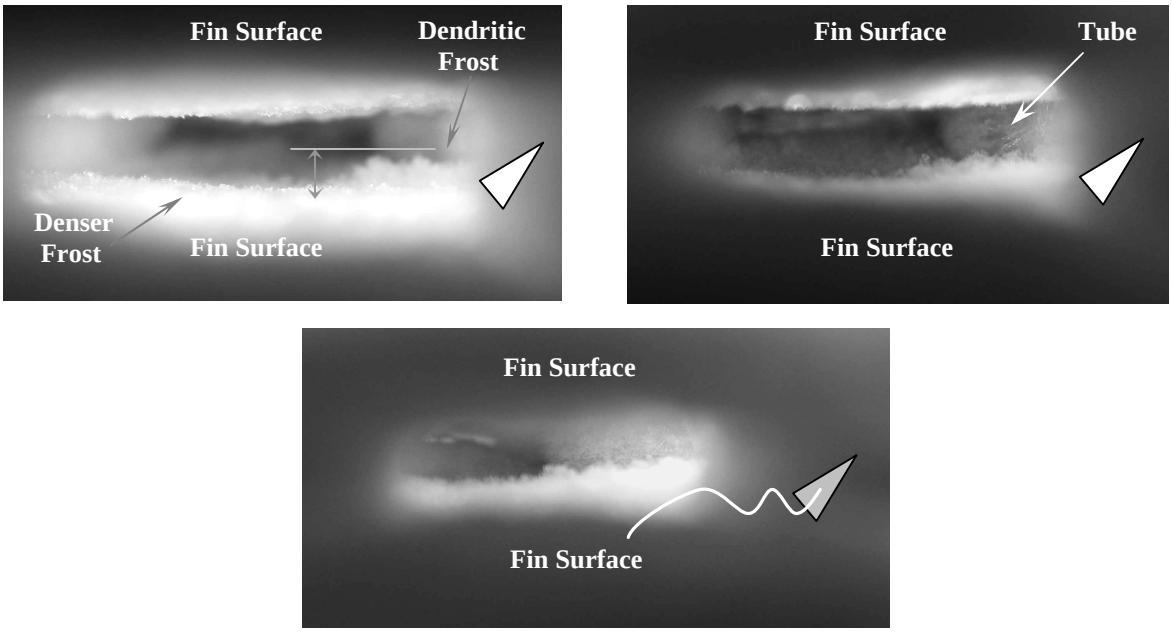

Figure 3.34- The frost was observed to be more dendritic away from the delta wing and closer to the tubes.

The modified volume-goodness factor, Θ, is also applied here to determine if there is a realizable benefit in this elevated core pressure drop range. As can be seen in Figure 3.36, the enhanced evaporator is still everywhere superior to the baseline one and exhibits the same transient decaying behavior as seen under the lightly frosted conditions; however, the realizable benefit is now diminished. Previously, for this same face velocity, the volume-goodness factor had been 4.2-4.8 kg/m^3sec. Now, as can be seen in Figure 3.38, these values have dropped to 3.6-4.2 kg/m^3sec. This graph suggests that the enhanced data are approaching the baseline data with respect to time. The results shown in Figure 3.35 and 3.36 correspond to an average face velocity of 0.95 to 1.06 m/s for the baseline data and 0.85 to 0.96 m/s for the enhanced data.

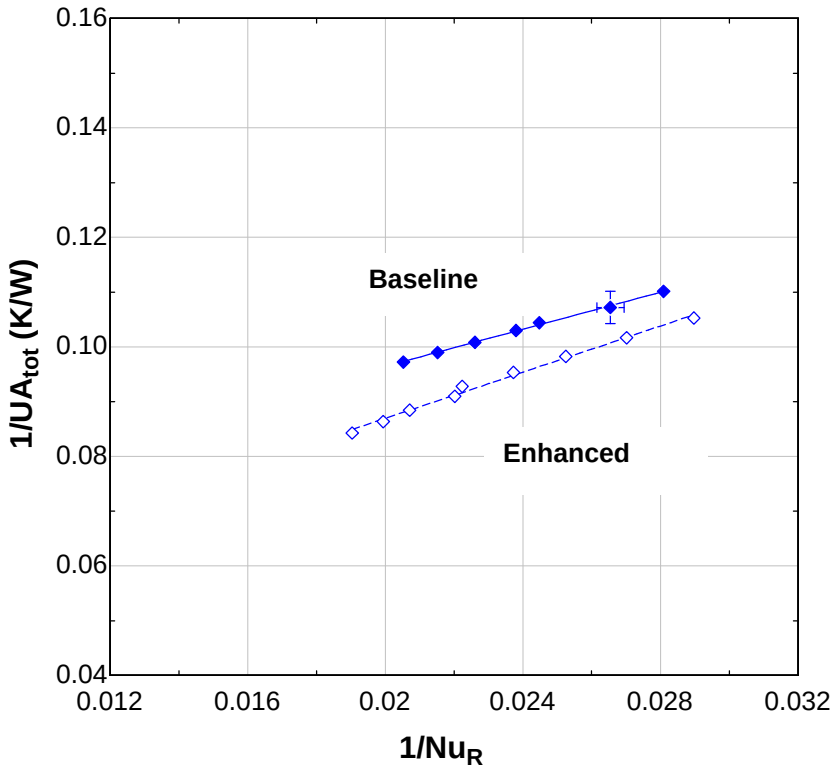

Figure 3.35- A Wilson plot at an average face velocity of 0.95m/s for the maximum frost condition.

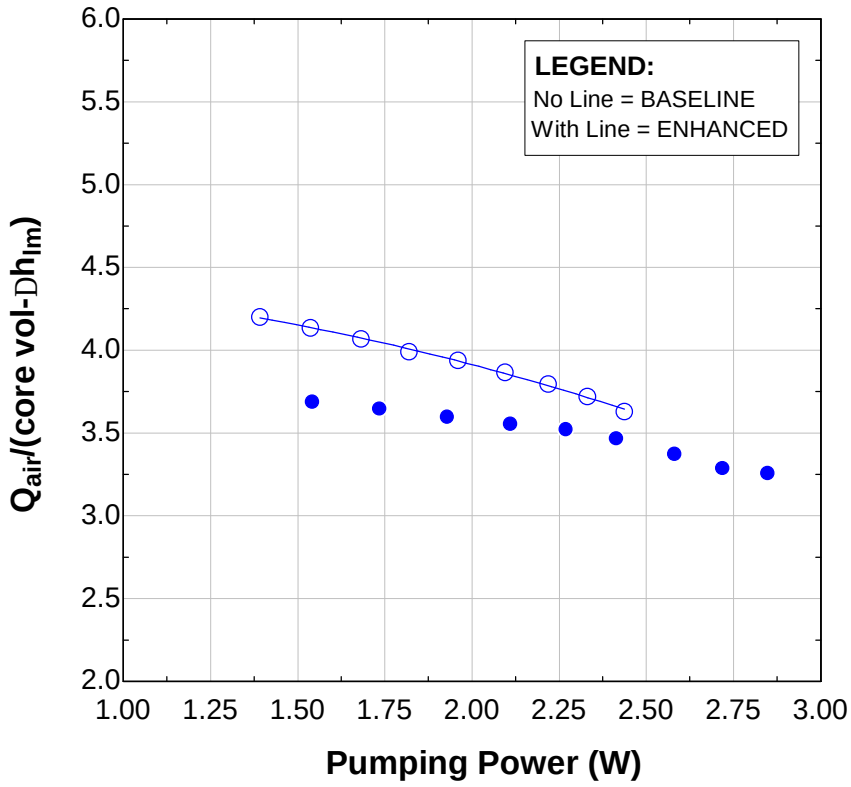

Figure 3.36- The modified volume-goodness factor for the maximum frost condition.

Chapter 4- Conclusions and Recommendations

4.1 Summary and Conclusions

Full-scale predictions of the effect that frost has on heat exchanger performance are a difficult and complicated task because of the local frost property sensitivity to substrate temperature, relative humidity, air flow conditions, and growth history. In this study, a full-scale heat exchanger was tested before and after the addition of delta wing vortex generators. Two types of vortex generator arrays were examined that differed only in the core depth location and the number of the delta wings attached. One array consisted of two rows of delta wings attached both at the leading edge and halfway downstream. The other array was a 4-row, staggered array where the delta wings were attached in an alternating single row, double row arrangement at a core depth interval of 50.8 mm. The tested heat exchanger was a brazed fin-and-tube evaporator with a fin spacing of 8.47 mm and is currently in production for domestic refrigeration. The vortex generators had an aspect ratio of 2.0 and were attached at an angle of attack of 55°. Tests were conducted in a wind tunnel with an environmentally controlled conditioning chamber. The coolant inlet temperature was maintained at –12 to –13 °C for each experiment, and the relative humidity was initially set at 80 % before the incipience of frost. The corresponding air inlet temperature was 10 to 11 °C while the air outlet temperature ranged from –4 to +2 °C. The range of air velocities examined was from 0.52 m/s to 1.2 m/s.

The results from these experiments will be enumerated below for clarity and convenience.

Configuration A (2-row array)

- Reductions of approximately 20% in the total thermal resistance were observed for face velocities of 1.1 m/s and 0.69 m/s. For a face velocity of 0.45m/s, the enhancement fell within the uncertainty of the experiment.
- Tests conducted under maximum frost accumulation exhibited a small thermal enhancement that also fell within the uncertainty of the experiment.

Configuration B (4-row array)

- For Reynolds numbers between 500 and 1200, the air-side thermal resistance was shown to decrease by 35% to 42% with the addition of the delta wings.
- The $\eta \cdot h$ increased by 55% to 84% with the addition of the delta wings. Typical values for the heat transfer coefficient for the enhanced case were 26-51 W/m^2-K and typical values for the baseline case were16-26 W/m^2-K.
- The London area-goodness factor, j/f, was plotted for various air-side Reynolds numbers, and a critical Reynolds number for operation was identified at which the enhanced evaporator first began to outperform the baseline data (i.e. $j/f_{enhanced} > j/f_{baseline}$). This Reynolds number was found to be approximately 700-750. Typical j/f values for the enhanced evaporator were found to lie between 0.10-0.34, and typical j/f factors for the baseline data were 0.05-0.26. [*]
- The modified volume-goodness factor revealed that the enhanced data were everywhere superior to the baseline data with a net enhancement of 16.7% to 32.9%.

[*] Assuming η equals unity.

- The frost density was calculated both from mass deposition rate data and from Hayashi's [1977] correlation. In both cases, the frost densities were on average 32 kg/m^3 greater for the enhanced data, suggesting that vortex-induced flow suppresses dendritic frost growth. This conclusion is further supported by the frost thickness data and is an important discovery because it suggests that frost grown under enhanced conditions possesses a higher thermal conductivity and therefore poses a smaller conduction resistance.
- The frost layer for the baseline data was shown to be on average 0.36 to 0.76 mm thicker than the frost layer for the enhanced data.

Other results suggest that vortex generation remains an effective enhancement technique on an unbrazed evaporator although this fact probably depends on the magnitude of the contact resistance present and therefore constitutes a case-by-case basis. Additionally, thermal enhancement does not appear to be strongly dependent upon the placement of the delta wing within the heat exchanger but rather just upon the number of delta wings present.

4.2 Recommendations for Future Work

Because of the inherent complications associated with full-scale modeling of frost on a heat exchanger, the approach taken in this research, which was to calculate an average frost thickness and then apply that thickness indiscriminately to all fin surfaces, would not generally be amendable to the louvered surface. The approach taken in this study was particularly successful because of the simple construction of the tested evaporator. The inline tubes and plain fin surfaces allowed a frost layer to grow numerically in time without the geometrical complexities of neighboring frost surfaces. As a result, it suggests that a more general model should be developed to handle the complicated geometries with highly interrupted surfaces. This task might be best accomplished by systematically stepping through the evaporator coil and measuring/calculating the coolant temperature in each pass. In this way, a spatially varying frost thickness could be calculated which would better match the physics of frost formation on a domestic refrigerator evaporator.

References

1. Bhatti, M.S. and R.K. Shah, 1987, "Turbulent and Transition Flow Convective Heat Transfer in Ducts," *Handbook of Single-Phase Convective Heat Transfer*, S. Kakac, R.K. Shah, and W. Aung, eds., New York, John Wiley & Sons, p. 4·34.

2. Biswas, G. and H. Chattopadhyay, 1992, "Heat Transfer in a Channel with Built-In Wing-Type Vortex Generators," *International Journal of Heat and Mass Transfer* 35(4), pp. 803-814.

3. Brian, P.L.T., Reid, R.C. and Y.T. Shah, 1970, "Frost Deposition on Cold Surfaces," *Ind. Eng. Chem. Fundamentals* 9(3), pp. 375-380.

4. Brockmeier, U., Guentermann, T.H., and M. Fiebig, 1993, "Performance Evaluation of a Vortex Generator Heat Transfer Surface and Comparison with Different High Performance Surfaces," *International Journal of Heat and Mass Transfer* 36(10), pp. 2575-2587.

5. Carrier, W.H., and S.W. Anderson, 1944, "The Resistance to Heat Flow through Finned Tubing," *Heating, Piping, & Air Conditioning* 16(5), pp. 304-320.

6. Cheng, Chin-Hsiang and Yu-Chieh Cheng, 2001, "Predictions of Frost Growth on a Cold Plate in Atmospheric Air," *Int. Comm. Heat Mass Transfer* 28(7), pp. 953-962.

7. Cheng, Chin-Hsiang and Keng-Hsien Wu, 2003, "Observations of Early-Stage Frost Formation on a Cold Plate in Atmospheric Air Flow," *Journal of Heat Transfer* 125, pp. 95-102.

8. El Sherbini, A.I. and A.M. Jacobi, 2000, "An Experimental Evaluation of the Thermal-Hydraulic Impact of Delta-Wing Vortex Generators in Plain-Fin-and-Tube Heat Exchangers," Air Conditioning and Refrigeration Center, *ACRC Report TR-172*.

9. Fiebig, M., 1998, "Vortices, Generators, and Heat Transfer," *Trans IChemE* 76(A), pp. 108-123.

10. Fiebig, M., Mitra, N.K., and Y. Dong, 1990, "Influence of Punched-Out Delta-Winglet Vortex Generators on Heat Transfer and Drag of Fin-Tubes," Wärme- und Stoffübertragung 25, pp. 33-43.

11. Fiebig, M., Kallweit, P., Mitra, N.K., and S. Tiggelbeck, 1991, "Heat Transfer Enhancement and Drag by Longitudinal Vortex Generators in Channel Flow," *Experimental Thermal and Fluid Science* 4(1), pp. 103-114.

12. Fiebig, M., Valencia, A., and N.K. Mitra, 1994, "Local Heat Transfer and Flow Losses in Fin-and-Tube Heat Exchangers with Vortex Generators: A Comparison of Round and Flat Tubes," *Experimental Thermal and Fluid Science* 8(1), pp. 35-45.

13. Gentry, M.C. and A.M. Jacobi, 1997, "Heat Transfer Enhancement by Delta-Wing Vortex Generators on a Flat Plate: Vortex Interactions with the Boundary Layer," *Experimental Thermal and Fluid Science* 14, pp. 231-242.

14. Gentry, M.C. and A.M. Jacobi, 1998, "Heat Transfer Enhancement Using Tip and Junction Vortices," Air Conditioning and Refrigeration Center, *ACRC Report TR-137*.

15. Hayashi, Y., Auki, A., Adachi, S., and K. Hori, 1977, "Study of Frost Properties Correlating with Frost Formation Types," *Journal of Heat Transfer* 99, pp. 239-245.

16. Inaba, H. and S. Imai, 1996, "Study on Sublimation Phenomenon of Horizontal Frost Layer Exposed to Forced Convection Air Flow and Radiant Heat," *Journal of Heat Transfer* 118, pp. 694-701.

17. Jones, B.W. and J.D. Parker, 1975, "Frost Formation with Varying Environmental Parameters," *Journal of Heat Transfer* 97, pp. 255-257.

18. Kline, S.J. and F.A. McClintock, 1953, "Describing Uncertainties in Single Sample Experiments," *Mechanical Engineering* 75, pp. 3-8.

19. Kwak, K.M., Torii, K., and K. Nishino, 2002, "Heat Transfer and Flow Characteristics of Fin-Tube Bundles with and without Winglet-Type Vortex Generators," *Experiments in Fluids* 33, pp. 696-702.

20. Lee, K.S., Kim, W.S., and T.H. Lee, 1997, "A One-Dimensional Model for Frost Formation on a Cold Flat Surface," *International Journal of Heat and Mass Transfer* 40(18), pp. 4359-4365.

21. Le Gall, R. and J.M. Grillot, 1997, "Modeling of Frost Growth and Densification," *International Journal of Heat and Mass Transfer* 40(13), pp. 3177-3187.

22. Mago, P.J. and S. A. Sherif, 2002, "Modeling the Cooling Process Path of a Dehumidifying Coil under Frosting Conditions," *Journal of Heat Transfer* 124, pp. 1182-1190.

23. Ogawa, K., Tanaka, N., and M. Takeshita, 1993, "Performance Improvement of Plate Fin-and-Tube Heat Exchangers under Frosting Conditions," *ASHRAE Transactions* 99(1), pp. 762-771.

24. Östin, R. and S. Andersson, 1991, "Frost Growth Parameters in a Forced Air Stream," *International Journal of Heat and Mass Transfer* 34(5), pp. 1009-1017.

25. Pohlhamus, E.C., 1966, "A Concept of the Vortex Lift of Sharp-Edge Delta Wings Based on a Leading Edge Suction Analogy," NASA, *TN D-3767*.

26. Rite, R.W. and R.R. Crawford, 1991, "The Effect of Frost Accumulation on the Performance of Domestic Refrigerator-Freezer Finned-Tube Evaporator Coils," *ASHRAE* Transactions 97(2), pp. 428-437.

27. Rite, R.W. and R.R. Crawford, 1991, "A Parametric Study of the Factors Governing the Rate of Frost Accumulation on Domestic Refrigerator-Freezer Finned-Tube Evaporator Coils," *ASHRAE* Transactions 97(2), pp. 438-445.

28. Rohsenow, W.M., Hartnett, J.P., and E.N. Gani′c, 1985, *Handbook of Heat Transfer Applications*, McGraw-Hill, New York.

29. Russell, C.M.B., Jones, T.V., and G.H. Lee, 1982, "Heat Transfer Enhancement Using Vortex Generators," *Heat Transfer, Proc. Seventh Heat Transfer Conference* 3, pp. 283-288.

30. Scheiman, S., 1981, "Considerations for the Installation of Honeycomb and Screens to Reduce Wind-Tunnel Turbulence," *NASA Technical Memorandum 81868*, pp. 1-50.

31. Schneider, H.W., 1978, "Equation of the Growth Rate of Frost Forming on Cooled Surfaces," *International Journal of Heat and Mass Transfer* 21, pp. 1019-1024.

32. Schubauer, G.B. and W.G. Spangenberg, 1960, "Forced Mixing in Boundary Layers," *Journal of Fluid Mechanics* 8, pp. 10-31.

33. Sherif, S.A., Raju, S.P., Padki, M.M., and A.B. Chan, 1993, "A Semi-Empirical Transient Method for Modeling Frost Formation on a Flat Plate," *International Journal of Refrigeration* 16(5), pp. 321-329.

34. Storey, B.D. and A.M. Jacobi, 1997,"Frost Growth in Laminar Channel Flows with Streamwise Vortices," Air Conditioning and Refrigeration Center, *ACRC Report TR-123*.

35. Storey, B.D. and A.M. Jacobi, 1999, "The Effect of Streamwise Vortices on the Frost Growth Rate in Developing Laminar Channel Flows," *International Journal of Heat and Mass Transfer* 42, pp. 3787-3802.

36. Senshu, T., Yasuda, H., Oguni, K., and K. Ishibani, 1990, "Heat Pump Performance under Frosting Conditions: Part I- Heat and Mass Transfer on Cross-Finned Tube Heat Exchangers under Frosting Conditions," *ASHRAE* Transactions 96(1).

37. Tao, Y.X., Besant, R.W., and K.S. Rezkallah, 1993, "A Mathematical Model for Predicting the Densification and Growth of Frost on a Flat Plate," *International Journal of Heat and Mass Transfer* 36(2), pp. 353-363.

38. Wexler, A. and R. Hyland, 1983, "Thermodynamic Properties of Dry Air, Moist Air and Water and SI Psychrometric Charts," *ASHRAE Transactions* 89 (2a), pp. 10-46.

39. White, J.E. and C.J. Cremers, 1981, "Prediction of Growth Parameters of Frost Deposits in Forced Convection," *Journal of Heat Transfer* 103, pp. 3-6.

Appendix A: Minimum Free Flow Area Calculation Methodology

Because the minimum free flow area is intrinsically linked to the hydraulic diameter, airside Reynolds number, and London area-goodness factor, special attention is paid here to its calculation. In a dry heat exchanger of the same geometry as the one tested, the minimum free flow area is calculated using the following equation:

$$A_{\min} = (c)(a) - 2D_o(a) - N_{fin}t_{fin}(c) \ ,$$

where *a* represents the cross-sectional length of the exchanger and *c* represents the height as shown below in the schematic. In this way, the minimum free flow area is simply the frontal area of the heat exchanger minus the area occupied by the tubes and fins.

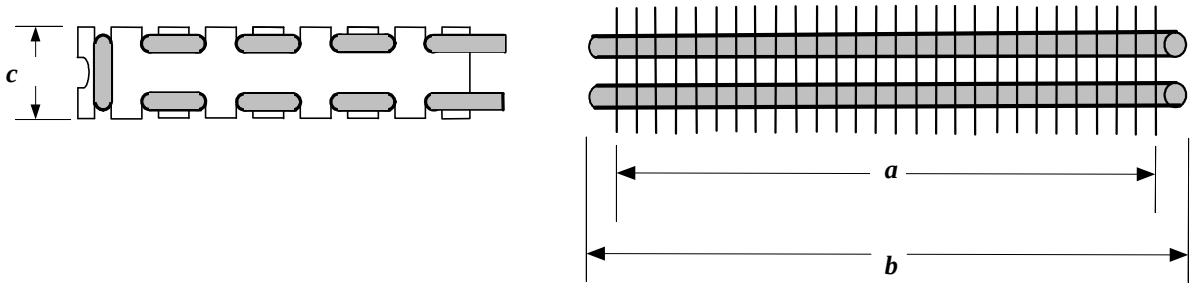

Figure A.1- Schematic of the evaporator dimensions needed in the calculation of minimum free flow area

In a frosted heat exchanger, however, additional terms must be subtracted from the frontal area to account for the flow area blocked by the frost layer. In examining these additional terms, let's look at the two sides of each fin separately. Face 1 will be the side of the fin without the VG, and face 2 will be the side with the attached VG. The approach that was taken in calculating the minimum free flow area was to add the growing frost layer to the fin thickness and then multiply this width term by the fin height subtracting out those lengths on the fin surface that were already accounted for by the tubes and VG. For example, for face 1, the sum of the fin thickness t_{fin} and frost thickness t_{frost} was multiplied by the fin height *c* minus $2D_o$ to avoid double counting the area occupied by the tubes. For face 2, the frost thickness t_{frost} was multiplied by the fin height *c* minus $2D_o$ minus the VG base length L_{VG} in arriving at the area that was physically blocked by the frost. The issue of the frost growing on the tube, however, still needed to be addressed. To correct for these regions (i.e. areas 1-4), a simple approximation was made. Because the frost thickness was known at the time of data collection, the sum of the frost height on the top and the bottom of both tube surfaces could be approximated as $L_{frost} = 4 \cdot t_{frost}$ and subtracted from the fin height *c* along with $2D_o$ (and L_{VG} if applicable) to avoid double counting areas before multiplying it by the frost thickness. These equations are summarized below for the enhanced data and the baseline data respectively:

Face 1

$$A_{min}\ (enhanced) = (c)(a) - 2D_o(a) - [(N_{fin}-1)(t_{fin}+ t_{frost})(c-2D_o-L_{frost})] -$$

Face 2 VG Area

$$[(N_{fin}-1)(t_{frost})(c-2D_o-L_{frost}-L_{VG})] - [(N_{VG})(1/2)(base)(chord)]$$

Both Faces

$$A_{min}\ (baseline) = (c)(a) - 2D_o(a) - [(N_{fin}-1)(t_{fin}+2t_{frost})(c-2D_o-L_{frost})]$$

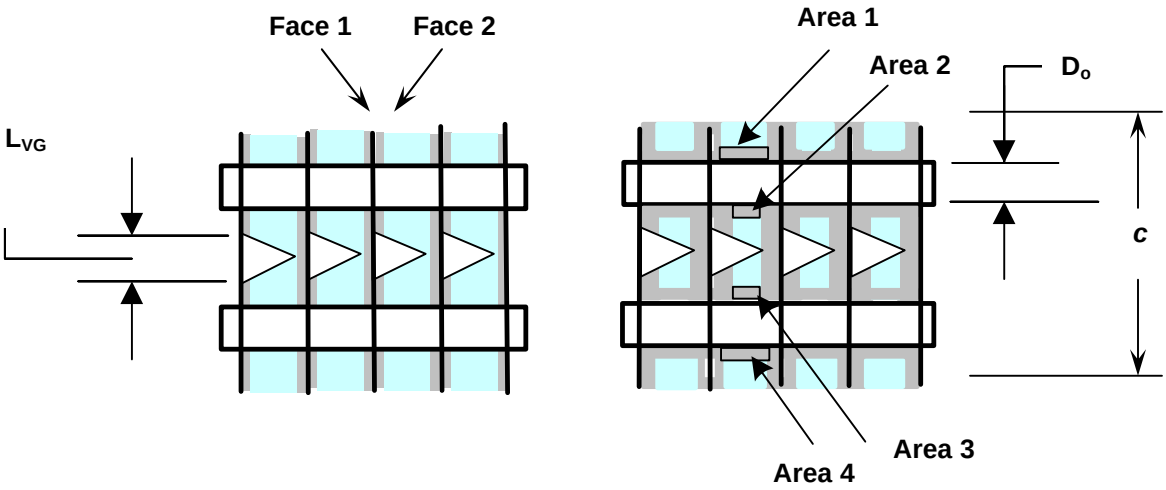

NOTE: $L_{frost} = 4\ t_{frost} = \Sigma$ height of areas 1-4

Figure A.2- Schematic of the passage areas subtracted from the minimum free flow area due to frost accumulation

Appendix B: Experimental Uncertainty Analysis

The uncertainty analysis performed in these tests was done almost exclusively in EES using its built-in uncertainty propagation software. When necessary, uncertainty propagation of a few calculated parameters was done manually according to the method of Kline and McClintock [1953]. These calculations are repeated below for clarity and convenience. All variable uncertainties are shown in Table B.1.

B.1 Uncertainty in Measured Parameters

The random error associated with all measured variables was essentially constant throughout the testing period and known from calibration procedures. Air-side temperature measurements were made using T-type thermocouples calibrated by total immersion in a NesLab isothermal bath against ASTM certified, mercury-in-glass thermometers. Adopting a 95% confidence interval (i.e. two sigma), the uncertainty associated with each thermocouple was estimated to be ±0.1 °C for the range of temperatures tested. The temperature of the coolant was measured using platinum RTDs with a calibration uncertainty of ±0.017°C. The relative humidity was measured using a thin film capacitance-type sensor with a published baseline uncertainty of ±2 % and an additional temperature dependent uncertainty of approximately ±0.5 % for air temperatures around 0 °C. Thus, the net uncertainty in the relative humidity measurement was determined to be 2.06%. A Micro Motion® Coriolis-type flow meter (Model D25) was used to measure the mass flow rate of the circulating coolant with a specified flow rate accuracy of ±0.2%, a zero stability of ±0.002 kg/sec, and a density measurement uncertainty of ±4 kg/m^3. Using the method of Kline and McClintock [1953], the total uncertainty associated with the coolant mass flow rate was found to be approximately 0.42%. An ASME standard orifice plate in the return loop of the wind tunnel was used to infer the mass flow rate of the air stream. The pressure drop across the orifice plate was measured using a Setra® 5-inch water column pressure transducer (Model 239) with an accuracy of 0.073% of the full-scale range. The uncertainty in this pressure measurement amounted to ±0.908 Pa. The pressure drop across the test section was also measured using a Setra® pressure transducer, which had an uncertainty of ±0.182 Pa.

Table B.1 Experimental Test Conditions and Uncertainties

Air inlet temperature, T_{ai}	10 to 11°C	±0.10 °C
Air outlet temperature, T_{ao}	-4 to 2°C	±0.10 °C
Coolant temperature, T_c	-12 to -13°C	±0.017 °C
Frost surface temperature, T_f	*varies*	±0.1 °C
Relative humidity, RH	80%	2.1%
Coolant mass flow, $\dot{m}_c$	~0.175 kg/s	0.4%
Core pressure drop, ΔP_{core}	20-80 Pa	±0.18 Pa
Orifice plate pressure drop, $\Delta P_{orifice}$	50-275 Pa	±0.91 Pa
Specific gravity, SG	1.068	±0.0005
Calculated frost thickness, δ_{frost}	≤ 3.9 mm	±0.25 mm
Frost growth time per measurement	420 sec	±20 sec
Minimum free flow area, A_{min} (dry)	0.0142 m^2	1.8%
Total surface area, A_{tot} (dry)	1.137 m^2	3.0%
Fin surface area, A_{fin} (dry)	0.924 m^2	1.4%
Tube surface area, A_{tube} (dry)	0.213 m^2	2.7%
Hydraulic diameter, D_h (dry)	10.15 mm	3.6%

B.2 Uncertainty in Calculated Parameters

B.2.1 Uncertainty in Hydraulic Diameter (Sample Calculation)

The error in the dry hydraulic diameter was due exclusively to resolution error associated with measuring the geometric dimensions of the heat exchanger. The time-evolving hydraulic diameter was calculated in EES and included additional terms such as those outlined in Appendix A to account for the growing frost layer. Shown below is a sample calculation of the uncertainty associated with the hydraulic diameter under dry conditions (i.e. no frost).

$$D_h = \frac{4\,A_{\min}\,\mathrm{L}}{\mathrm{A_T}}$$

$$W_{D_h} = \sqrt{\left[\left(\frac{\partial \mathrm{D_h}}{\partial A_{\min}} W_{A_{\min}}\right)^2 + \left(\frac{\partial D_h}{\partial L} W_L\right)^2 + \left(\frac{\partial D_h}{\partial A_T} W_{A_T}\right)^2\right]}$$

$$\frac{\partial D_h}{\partial A_{\min}} = \frac{4\,\mathrm{L}}{\mathrm{A_T}} = \frac{4\,(203.2)}{(1{,}136{,}400)} = 7.152E-4\,mm^{-1} \quad \text{with} \quad W_{A_{\min}} = \pm 261\,mm^2$$

$$\frac{\partial D_h}{\partial L} = \frac{4\,A_{\min}}{A_T} = \frac{4\,(14{,}186)}{(1{,}136{,}400)} = 4.993E-2 \quad \text{with} \quad W_L = 1.59mm$$

$$\frac{\partial D_h}{\partial A_T} = \frac{-4\,A_{\min}\,L}{{A_T}^2} = \frac{-4(14{,}186)(203.2)}{(1{,}136{,}400)^2} = 8.928E-6mm^{-1} \quad \text{with} \quad W_{A_T} = 34{,}434mm^2$$

Therefore, we have…

$$W_{D_h} = \sqrt{\left[\left((7.152E-4)(261)\right)^2 + \left((4.993E-2)(1.59)\right)^2 + \left((8.928E-6)(34{,}434)\right)^2\right]} = 0.368mm$$

$$UC_{Dh} = \frac{0.368mm}{10.15mm} \cdot 100 = 3.63\%$$

B.2.2 Uncertainty in Minimum Free Flow Area

The error in the time-evolving minimum free flow area was calculated in EES according to the following equation:

A_{min} (baseline) = (c)(a) – $2D_o$(a)-[(N_{fin}-1)(t_{fin}+2t_{frost})(c-2D_o-L_{frost})]

$$W_{A_{min}} = \sqrt{\left[\left(\frac{\partial A_{min}}{\partial c} W_c\right)^2 + \left(\frac{\partial A_{min}}{\partial a} W_a\right)^2 + \left(\frac{\partial A_{min}}{\partial D_o} W_{D_o}\right)^2 + \left(\frac{\partial A_{min}}{\partial t_{fin}} W_{t_{fin}}\right)^2 + \left(\frac{\partial A_{min}}{\partial t_{frost}} W_{t_{frost}}\right)^2 + \left(\frac{\partial A_{min}}{\partial L_{frost}} W_{L_{frost}}\right)^2\right]}$$

Appendix C: Unbrazed Heat Exchanger Experimentation

This segment of testing was done on mechanically fit (or unbrazed) evaporators of Configuration B and C. These types of evaporators, which are more common commercially, are manufactured by forcing the tubes into the fin material during assembly. There is no metallurgical bonding of the tube to the fin and thus a large contact resistance can exist between the two components. Because the contact resistance is unknown and varies with each frosting cycle, the data that follow will be presented in the form of a Wilson plot, where the total thermal resistance is plotted versus the inverse of the tube-side Nusselt number. In this way, the contact resistance is lumped into the total thermal resistance and does not need to be known. This is important because the frost-defrost cycle of the evaporator can substantially affect the contact resistance.

C.1 Wilson Plot Results

Thermal enhancement is evident for the enhanced evaporator; however, it does not follow the usual trends seen in a Wilson plot due to the varying contact resistance from test to test. For example, in Figure C.1, the greatest enhancement occurs at the lowest velocity- a phenomenon that is counterintuitive and contrary to expectations. One possible explanation for this result is that the repeated frosting and defrosting of these coils continually changes the contact resistance between experimental runs. This does not explain, however, why the baseline data all collapse on one another. The important conclusion from this figure is that vortex generation does appear to be a viable heat transfer enhancement method for certain unbrazed evaporators and is therefore not limited to the brazed heat exchanger. Its applicability, however, will depend on the severity of the contact resistance and thus constitutes a case-by-case decision.

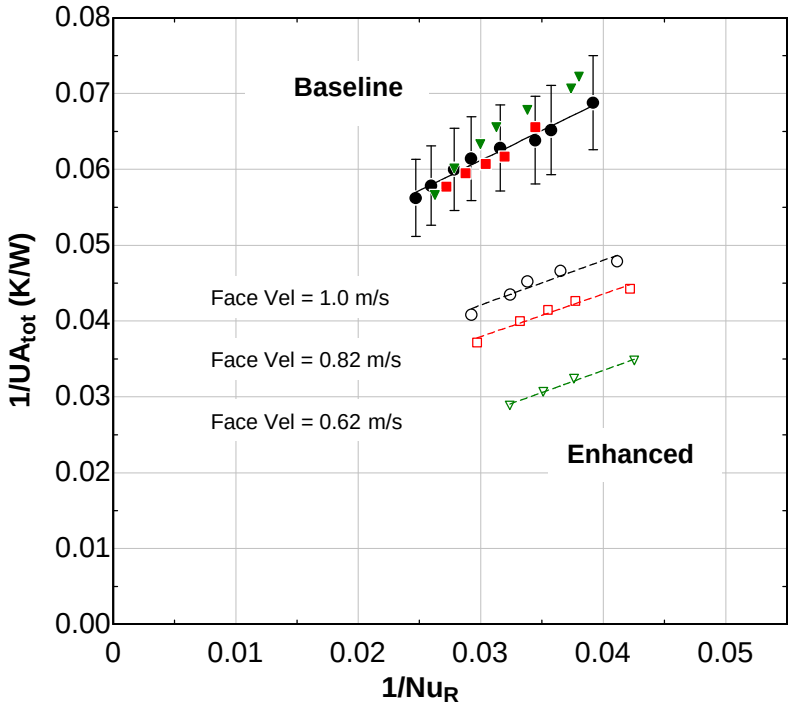

Figure C.1- A Wilson plot of thermal enhancement for an unbrazed evaporator of configuration C with varying contact resistance.

C.2 Configuration Comparisons

Another important discovery made during these tests was that the thermal enhancement does not appear to be a function of the placement of the vortex generator but rather the number of vortex generators present. This is shown below in Figure C.2. For an equal number of vortex generators with different orientations, the change in the overall thermal conductance fell within the uncertainty of the experiment, which was approximately 7.5%. Because of the large contact resistance present in these tests, this conclusion, although true for unbrazed evaporators, should not be extended to brazed evaporators where variations in vortex generator orientation may be important.

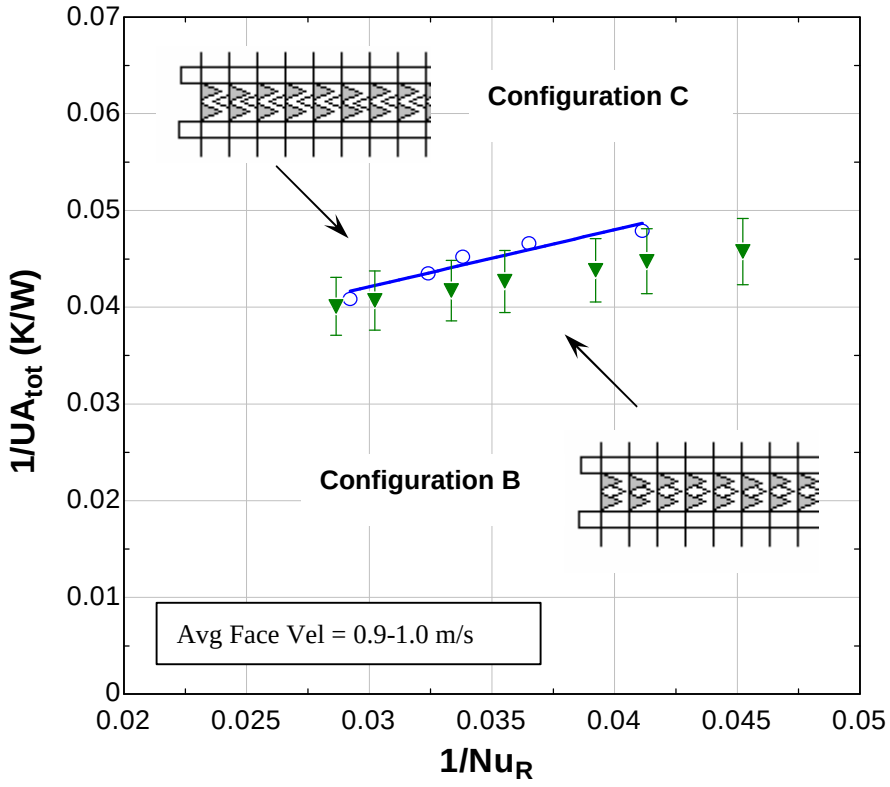

Figure C.2- A Wilson plot comparison of two different vortex generator arrays reveals that the enhancement is not very sensitive to delta wing placement.

Appendix D: EES Data Reduction Code

```
{ACRC Project 121 Data Reduction Algorithm}
{Date:}
{Coolant Setpoint= }
{Coolant Hz= }
{Blower Hz= }
{Pre-heaters= }
{Aft-heaters= }
{Valve= }

{DOWTHERM 4000 PROPERTIES}
FUNCTION rhoRTD(Tsg, volp)
rhoneg25:=(1.5050E-05*volp^3)-(8.6293E-03*volp^2)+(2.3816*volp)+1008.562
rhoneg20:=(2.8380E-05*volp^3)-(1.0215E-02*volp^2)+(2.4242*volp)+1006.621
rhoneg15:=(2.7123E-05*volp^3)-(9.9603E-03*volp^2)+(2.3905*volp)+1005.642
rhoneg10:=(2.0838E-05*volp^3)-(9.0259E-03*volp^2)+(2.3264*volp)+1005.035
rhoneg5:=(2.2790E-05*volp^3)-(9.1960E-03*volp^2)+(2.3114*volp)+1003.632
rho0:=(2.8578E-05*volp^3)-(9.7922E-03*volp^2)+(2.3119*volp)+1001.962
rho5:=(1.3892E-05*volp^3)-(7.7902E-03*volp^2)+(2.2034*volp)+1001.726
rho10:=(6.1192E-06*volp^3)-(6.7028E-03*volp^2)+(2.1350*volp)+1000.835
rho15:=(4.4984E-06*volp^3)-(6.4244E-03*volp^2)+(2.1022*volp)+999.337
rho20:=(2.3385E-05*volp^3)-(8.6731E-03*volp^2)+(2.1718*volp)+996.401
rho25:=(2.9901E-05*volp^3)-(9.4182E-03*volp^2)+(2.1817*volp)+994.163
IF (Tsg>-25) AND (Tsg<=-20) then rhoRTD:=((-25-Tsg)/(20-25))*(rhoneg20-rhoneg25)+rhoneg25 ELSE
IF (Tsg>-20) AND (Tsg<=-15) then rhoRTD:=((-20-Tsg)/(15-20))*(rhoneg15-rhoneg20)+rhoneg20 ELSE
IF (Tsg>-15) AND (Tsg<=-10) then rhoRTD:=((-15-Tsg)/(10-15))*(rhoneg10-rhoneg15)+rhoneg15 ELSE
IF (Tsg>-10) AND (Tsg<=-5) then rhoRTD:=((-10-Tsg)/(5-10))*(rhoneg5-rhoneg10)+rhoneg10 ELSE
IF (Tsg>-5) AND (Tsg<=0) then rhoRTD:=((-5-Tsg)/(0-5))*(rho0-rhoneg5)+rhoneg5 ELSE
IF (Tsg>0) AND (Tsg<=5) then rhoRTD:=((Tsg-0)/(5-0))*(rho5-rho0)+rho0 ELSE
IF (Tsg>5) AND (Tsg<=10) then rhoRTD:=((Tsg-5)/(10-5))*(rho10-rho5)+rho5 ELSE
IF (Tsg>10) AND (Tsg<=15) then rhoRTD:=((Tsg-10)/(15-10))*(rho15-rho10)+rho10 ELSE
IF (Tsg>15) AND (Tsg<=20) then rhoRTD:=((Tsg-15)/(20-15))*(rho20-rho15)+rho15 ELSE
IF (Tsg>20) AND (Tsg<=25) then rhoRTD:=((Tsg-20)/(25-20))*(rho25-rho20)+rho20
ENDIF
ENDIF
ENDIF
ENDIF
ENDIF
ENDIF
ENDIF
ENDIF
ENDIF
END

FUNCTION rhoc(z, i, T[1..z], volp)
rho30:=-(0.0010633*T[i]^2)-0.413564*T[i]+1063.282000
rho31:=-(0.0015727*T[i]^2)-0.430458*T[i]+1070.037000
rho32:=-(0.0015670*T[i]^2)-0.422109*T[i]+1066.851000
rho33:=-(0.0015669*T[i]^2)-0.426382*T[i]+1068.618000
rho34:=-(0.001573*T[i]^2)-0.430460*T[i]+1070.037000
rho35:=-(0.001568*T[i]^2)-0.434384*T[i]+1072.109801
rho36:=-(0.001565*T[i]^2)-0.438654*T[i]+1073.832316
rho37:=-(0.001565*T[i]^2)-0.442654*T[i]+1075.542316
rho38:=-(0.001557*T[i]^2)-0.446567*T[i]+1077.239978
rho39:=-(0.001558*T[i]^2)-0.450309*T[i]+1078.925879
rho40:=-(0.001556*T[i]^2)-0.454129*T[i]+1080.599861
rho41:=-(0.001549*T[i]^2)-0.458023*T[i]+1082.257874
rho42:=-(0.001553*T[i]^2)-0.461799*T[i]+1083.905377
rho43:=-(0.001549*T[i]^2)-0.465556*T[i]+1085.540208
rho44:=-(0.001534*T[i]^2)-0.469038*T[i]+1087.162117
```

```
rho45:=-(0.001537*T[i]^2)-0.472701*T[i]+1088.773268
rho46:=-(0.001532*T[i]^2)-0.476325*T[i]+1090.368766
rho47:=-(0.001522*T[i]^2)-0.479650*T[i]+1091.957844
rho48:=-(0.001522*T[i]^2)-0.483221*T[i]+1093.532294
rho49:=-(0.001522*T[i]^2)-0.486783*T[i]+1095.092177
rho50:=-(0.001532*T[i]^2)-0.490325*T[i]+1096.648766
IF (volp>30) AND (volp<=31 ) then rhoc:=((volp-30)/1)*(rho31-rho30)+rho30 ELSE
IF (volp>31) AND (volp<=32 ) then rhoc:=((volp-31)/1)*(rho32-rho31)+rho31 ELSE
IF (volp>32) AND (volp<=33 ) then rhoc:=((volp-32)/1)*(rho33-rho32)+rho32 ELSE
IF (volp>33) AND (volp<=34 ) then rhoc:=((volp-33)/1)*(rho34-rho33)+rho33 ELSE
IF (volp>34) AND (volp<=35) then rhoc:=((volp-34)/1)*(rho35-rho34)+rho34 ELSE
IF (volp>35) AND (volp<=36) then rhoc:=((volp-35)/1)*(rho36-rho35)+rho35 ELSE
IF (volp>36) AND (volp<=37) then rhoc:=((volp-36)/1)*(rho37-rho36)+rho36 ELSE
IF (volp>37) AND (volp<=38) then rhoc:=((volp-37)/1)*(rho38-rho37)+rho37 ELSE
IF (volp>38) AND (volp<=39) then rhoc:=((volp-38)/1)*(rho39-rho38)+rho38 ELSE
IF (volp>39) AND (volp<=40) then rhoc:=((volp-39)/1)*(rho40-rho39)+rho39 ELSE
IF (volp>40) AND (volp<=41) then rhoc:=((volp-40)/1)*(rho41-rho40)+rho40 ELSE
IF (volp>41) AND (volp<=42) then rhoc:=((volp-41)/1)*(rho42-rho41)+rho41 ELSE
IF (volp>42) AND (volp<=43) then rhoc:=((volp-42)/1)*(rho43-rho42)+rho42 ELSE
IF (volp>43) AND (volp<=44) then rhoc:=((volp-43)/1)*(rho44-rho43)+rho43 ELSE
IF (volp>44) AND (volp<=45) then rhoc:=((volp-44)/1)*(rho45-rho44)+rho44 ELSE
IF (volp>45) AND (volp<=46) then rhoc:=((volp-45)/1)*(rho46-rho45)+rho45 ELSE
IF (volp>46) AND (volp<=47) then rhoc:=((volp-46)/1)*(rho47-rho46)+rho46 ELSE
IF (volp>47) AND (volp<=48) then rhoc:=((volp-47)/1)*(rho48-rho47)+rho47 ELSE
IF (volp>48) AND (volp<=49) then rhoc:=((volp-48)/1)*(rho49-rho48)+rho48 ELSE
IF (volp>49) AND (volp<=50) then rhoc:=((volp-49)/1)*(rho50-rho49)+rho49
ENDIF
ENDIF
ENDIF
ENDIF
ENDIF
ENDIF
ENDIF
ENDIF
ENDIF
ENDIF
ENDIF
ENDIF
ENDIF
ENDIF
ENDIF
ENDIF
ENDIF
ENDIF
END

FUNCTION visc(z, i, T[1..z], volp)
visc30:=(2.59357E-09*T[i]^4)-(1.24527E-07*T[i]^3)+(3.80746E-06*T[i]^2)-(1.46565E-04*T[i])+4.15126E-03
visc31:=(3.3303E-09*T[i]^4)-(1.3655E-07*T[i]^3)+(3.8711E-06*T[i]^2)-(1.5812E-04*T[i])+4.3106E-03
visc32:=(3.4346E-09*T[i]^4)-(1.5706E-07*T[i]^3)+(4.3735E-06*T[i]^2)-(1.6207E-04*T[i])+4.4880E-03
visc33:=(3.7452E-09*T[i]^4)-(1.7381E-07*T[i]^3)+(4.7303E-06*T[i]^2)-(1.6929E-04*T[i])+4.6446E-03
visc34:=(5.2066E-09*T[i]^4)-(1.7178E-07*T[i]^3)+(4.5592E-06*T[i]^2)-(1.8174E-04*T[i])+4.8514E-03
visc35:=(7.0687E-09*T[i]^4)-(1.4965E-07*T[i]^3)+(4.5991E-06*T[i]^2)-(1.9586E-04*T[i])+5.0315E-03
visc36:=(7.6549E-09*T[i]^4)-(1.5947E-07*T[i]^3)+(4.8147E-06*T[i]^2)-(2.0466E-04*T[i])+5.2146E-03
visc37:=(8.2286E-09*T[i]^4)-(1.6897E-07*T[i]^3)+(5.0273E-06*T[i]^2)-(2.1347E-04*T[i])+5.4006E-03
visc38:=(8.8678E-09*T[i]^4)-(1.7749E-07*T[i]^3)+(5.1585E-06*T[i]^2)-(2.2022E-04*T[i])+5.5631E-03
visc39:=(9.5492E-09*T[i]^4)-(1.8521E-07*T[i]^3)+(5.2334E-06*T[i]^2)-(2.2556E-04*T[i])+5.7107E-03
visc40:=(1.0179E-08*T[i]^4)-(1.9301E-07*T[i]^3)+(5.3399E-06*T[i]^2)-(2.3180E-04*T[i])+5.8722E-03
visc41:=(1.0754E-08*T[i]^4)-(2.0096E-07*T[i]^3)+(5.4795E-06*T[i]^2)-(2.3891E-04*T[i])+6.0476E-03
visc42:=(1.1278E-08*T[i]^4)-(2.0898E-07*T[i]^3)+(5.6504E-06*T[i]^2)-(2.4689E-04*T[i])+6.2368E-03
visc43:=(1.1748E-08*T[i]^4)-(2.1715E-07*T[i]^3)+(5.8534E-06*T[i]^2)-(2.5573E-04*T[i])+6.4397E-03
```

```
visc44:=(1.2169E-08*T[i]^4)-(2.2538E-07*T[i]^3)+(6.0875E-06*T[i]^2)-(2.6544E-04*T[i])+6.6562E-03
visc45:=(1.2537E-08*T[i]^4)-(2.3374E-07*T[i]^3)+(6.3534E-06*T[i]^2)-(2.7599E-04*T[i])+6.8861E-03
visc46:=(1.2854E-08*T[i]^4)-(2.4219E-07*T[i]^3)+(6.6503E-06*T[i]^2)-(2.8739E-04*T[i])+7.1294E-03
visc47:=(1.3121E-08*T[i]^4)-(2.5077E-07*T[i]^3)+(6.9777E-06*T[i]^2)-(2.9963E-04*T[i])+7.3861E-03
visc48:=(1.3033E-08*T[i]^4)-(2.5591E-07*T[i]^3)+(7.3122E-06*T[i]^2)-(3.1146E-04*T[i])+7.6351E-03
visc49:=(1.2639E-08*T[i]^4)-(2.5817E-07*T[i]^3)+(7.6572E-06*T[i]^2)-(3.2306E-04*T[i])+7.8795E-03
visc50:=(1.2330E-08*T[i]^4)-(2.6211E-07*T[i]^3)+(8.0434E-06*T[i]^2)-(3.3604E-04*T[i])+8.1464E-03
IF (volp>30) AND (volp<=31) then visc:=((volp-30)/1)*(visc31-visc30)+visc30 ELSE
IF (volp>31) AND (volp<=32) then visc:=((volp-31)/1)*(visc32-visc31)+visc31 ELSE
IF (volp>32) AND (volp<=33) then visc:=((volp-32)/1)*(visc33-visc32)+visc32 ELSE
IF (volp>33) AND (volp<=34) then visc:=((volp-33)/1)*(visc34-visc33)+visc33 ELSE
IF (volp>34) AND (volp<=35) then visc:=((volp-34)/1)*(visc35-visc34)+visc34 ELSE
IF (volp>35) AND (volp<=36) then visc:=((volp-35)/1)*(visc36-visc35)+visc35 ELSE
IF (volp>36) AND (volp<=37) then visc:=((volp-36)/1)*(visc37-visc36)+visc36 ELSE
IF (volp>37) AND (volp<=38) then visc:=((volp-37)/1)*(visc38-visc37)+visc37 ELSE
IF (volp>38) AND (volp<=39) then visc:=((volp-38)/1)*(visc39-visc38)+visc38 ELSE
IF (volp>39) AND (volp<=40) then visc:=((volp-39)/1)*(visc40-visc39)+visc39 ELSE
IF (volp>40) AND (volp<=41) then visc:=((volp-40)/1)*(visc41-visc40)+visc40 ELSE
IF (volp>41) AND (volp<=42) then visc:=((volp-41)/1)*(visc42-visc41)+visc41 ELSE
IF (volp>42) AND (volp<=43) then visc:=((volp-42)/1)*(visc43-visc42)+visc42 ELSE
IF (volp>43) AND (volp<=44) then visc:=((volp-43)/1)*(visc44-visc43)+visc43 ELSE
IF (volp>44) AND (volp<=45) then visc:=((volp-44)/1)*(visc45-visc44)+visc44 ELSE
IF (volp>45) AND (volp<=46) then visc:=((volp-45)/1)*(visc46-visc45)+visc45 ELSE
IF (volp>46) AND (volp<=47) then visc:=((volp-46)/1)*(visc47-visc46)+visc46 ELSE
IF (volp>47) AND (volp<=48) then visc:=((volp-47)/1)*(visc48-visc47)+visc47 ELSE
IF (volp>48) AND (volp<=49) then visc:=((volp-48)/1)*(visc49-visc48)+visc48 ELSE
IF (volp>49) AND (volp<=50) then visc:=((volp-49)/1)*(visc50-visc49)+visc49
ENDIF
ENDIF
ENDIF
ENDIF
ENDIF
ENDIF
ENDIF
ENDIF
ENDIF
ENDIF
ENDIF
ENDIF
ENDIF
ENDIF
ENDIF
ENDIF
ENDIF
ENDIF
ENDIF
END

FUNCTION nuw(z, i, Tm[1..z], volp)
visc30:=(2.59357E-09*Tm[i]^4)-(1.24527E-07*Tm[i]^3)+(3.80746E-06*Tm[i]^2)-(1.46565E-04*Tm[i])+4.15126E-03
visc31:=(3.3303E-09*Tm[i]^4)-(1.3655E-07*Tm[i]^3)+(3.8711E-06*Tm[i]^2)-(1.5812E-04*Tm[i])+4.3106E-03
visc32:=(3.4346E-09*Tm[i]^4)-(1.5706E-07*Tm[i]^3)+(4.3735E-06*Tm[i]^2)-(1.6207E-04*Tm[i])+4.4880E-03
visc33:=(3.7452E-09*Tm[i]^4)-(1.7381E-07*Tm[i]^3)+(4.7303E-06*Tm[i]^2)-(1.6929E-04*Tm[i])+4.6446E-03
visc34:=(5.2066E-09*Tm[i]^4)-(1.7178E-07*Tm[i]^3)+(4.5592E-06*Tm[i]^2)-(1.8174E-04*Tm[i])+4.8514E-03
visc35:=(7.0687E-09*Tm[i]^4)-(1.4965E-07*Tm[i]^3)+(4.5991E-06*Tm[i]^2)-(1.9586E-04*Tm[i])+5.0315E-03
visc36:=(7.6549E-09*Tm[i]^4)-(1.5947E-07*Tm[i]^3)+(4.8147E-06*Tm[i]^2)-(2.0466E-04*Tm[i])+5.2146E-03
visc37:=(8.2286E-09*Tm[i]^4)-(1.6897E-07*Tm[i]^3)+(5.0273E-06*Tm[i]^2)-(2.1347E-04*Tm[i])+5.4006E-03
visc38:=(8.8678E-09*Tm[i]^4)-(1.7749E-07*Tm[i]^3)+(5.1585E-06*Tm[i]^2)-(2.2022E-04*Tm[i])+5.5631E-03
visc39:=(9.5492E-09*Tm[i]^4)-(1.8521E-07*Tm[i]^3)+(5.2334E-06*Tm[i]^2)-(2.2556E-04*Tm[i])+5.7107E-03
visc40:=(1.0179E-08*Tm[i]^4)-(1.9301E-07*Tm[i]^3)+(5.3399E-06*Tm[i]^2)-(2.3180E-04*Tm[i])+5.8722E-03
visc41:=(1.0754E-08*Tm[i]^4)-(2.0096E-07*Tm[i]^3)+(5.4795E-06*Tm[i]^2)-(2.3891E-04*Tm[i])+6.0476E-03
visc42:=(1.1278E-08*Tm[i]^4)-(2.0898E-07*Tm[i]^3)+(5.6504E-06*Tm[i]^2)-(2.4689E-04*Tm[i])+6.2368E-03
```

```
visc43:=(1.1748E-08*Tm[i]^4)-(2.1715E-07*Tm[i]^3)+(5.8534E-06*Tm[i]^2)-(2.5573E-04*Tm[i])+6.4397E-03
visc44:=(1.2169E-08*Tm[i]^4)-(2.2538E-07*Tm[i]^3)+(6.0875E-06*Tm[i]^2)-(2.6544E-04*Tm[i])+6.6562E-03
visc45:=(1.2537E-08*Tm[i]^4)-(2.3374E-07*Tm[i]^3)+(6.3534E-06*Tm[i]^2)-(2.7599E-04*Tm[i])+6.8861E-03
visc46:=(1.2854E-08*Tm[i]^4)-(2.4219E-07*Tm[i]^3)+(6.6503E-06*Tm[i]^2)-(2.8739E-04*Tm[i])+7.1294E-03
visc47:=(1.3121E-08*Tm[i]^4)-(2.5077E-07*Tm[i]^3)+(6.9777E-06*Tm[i]^2)-(2.9963E-04*Tm[i])+7.3861E-03
visc48:=(1.3033E-08*Tm[i]^4)-(2.5591E-07*Tm[i]^3)+(7.3122E-06*Tm[i]^2)-(3.1146E-04*Tm[i])+7.6351E-03
visc49:=(1.2639E-08*Tm[i]^4)-(2.5817E-07*Tm[i]^3)+(7.6572E-06*Tm[i]^2)-(3.2306E-04*Tm[i])+7.8795E-03
visc50:=(1.2330E-08*Tm[i]^4)-(2.6211E-07*Tm[i]^3)+(8.0434E-06*Tm[i]^2)-(3.3604E-04*Tm[i])+8.1464E-03
IF (volp>30) AND (volp<=31) then nuw:=((volp-30)/1)*(visc31-visc30)+visc30 ELSE
IF (volp>31) AND (volp<=32) then nuw:=((volp-31)/1)*(visc32-visc31)+visc31 ELSE
IF (volp>32) AND (volp<=33) then nuw:=((volp-32)/1)*(visc33-visc32)+visc32 ELSE
IF (volp>33) AND (volp<=34) then nuw:=((volp-33)/1)*(visc34-visc33)+visc33 ELSE
IF (volp>34) AND (volp<=35) then nuw:=((volp-34)/1)*(visc35-visc34)+visc34 ELSE
IF (volp>35) AND (volp<=36) then nuw:=((volp-35)/1)*(visc36-visc35)+visc35 ELSE
IF (volp>36) AND (volp<=37) then nuw:=((volp-36)/1)*(visc37-visc36)+visc36 ELSE
IF (volp>37) AND (volp<=38) then nuw:=((volp-37)/1)*(visc38-visc37)+visc37 ELSE
IF (volp>38) AND (volp<=39) then nuw:=((volp-38)/1)*(visc39-visc38)+visc38 ELSE
IF (volp>39) AND (volp<=40) then nuw:=((volp-39)/1)*(visc40-visc39)+visc39 ELSE
IF (volp>40) AND (volp<=41) then nuw:=((volp-40)/1)*(visc41-visc40)+visc40 ELSE
IF (volp>41) AND (volp<=42) then nuw:=((volp-41)/1)*(visc42-visc41)+visc41 ELSE
IF (volp>42) AND (volp<=43) then nuw:=((volp-42)/1)*(visc43-visc42)+visc42 ELSE
IF (volp>43) AND (volp<=44) then nuw:=((volp-43)/1)*(visc44-visc43)+visc43 ELSE
IF (volp>44) AND (volp<=45) then nuw:=((volp-44)/1)*(visc45-visc44)+visc44 ELSE
IF (volp>45) AND (volp<=46) then nuw:=((volp-45)/1)*(visc46-visc45)+visc45 ELSE
IF (volp>46) AND (volp<=47) then nuw:=((volp-46)/1)*(visc47-visc46)+visc46 ELSE
IF (volp>47) AND (volp<=48) then nuw:=((volp-47)/1)*(visc48-visc47)+visc47 ELSE
IF (volp>48) AND (volp<=49) then nuw:=((volp-48)/1)*(visc49-visc48)+visc48 ELSE
IF (volp>49) AND (volp<=50) then nuw:=((volp-49)/1)*(visc50-visc49)+visc49
ENDIF
ENDIF
ENDIF
ENDIF
ENDIF
ENDIF
ENDIF
ENDIF
ENDIF
ENDIF
ENDIF
ENDIF
ENDIF
ENDIF
ENDIF
ENDIF
ENDIF
ENDIF
ENDIF
END

FUNCTION kc(z, i, T[1..z], volp)
k30:=-(2.984E-06*T[i]^2)+(1.158E-03*T[i])+4.237E-01
k31:=-(2.965E-06*T[i]^2)+(1.135E-03*T[i])+4.197E-01
k32:=-(2.849E-06*T[i]^2)+(1.114E-03*T[i])+4.158E-01
k33:=-(2.872E-06*T[i]^2)+(1.093E-03*T[i])+4.119E-01
k34:=-(2.779E-06*T[i]^2)+(1.071E-03*T[i])+4.081E-01
k35:=-(2.242E-06*T[i]^2)+(1.058E-03*T[i])+4.043E-01
k36:=-(2.268E-06*T[i]^2)+(1.037E-03*T[i])+4.005E-01
k37:=-(2.195E-06*T[i]^2)+(1.017E-03*T[i])+3.968E-01
k38:=-(2.117E-06*T[i]^2)+(9.958E-04*T[i])+3.931E-01
k39:=-(2.165E-06*T[i]^2)+(9.764E-04*T[i])+3.895E-01
k40:=-(2.043E-06*T[i]^2)+(9.562E-04*T[i])+3.859E-01
k41:=-(2.030E-06*T[i]^2)+(9.374E-04*T[i])+3.823E-01
```

```
k42:=-(1.996E-06*T[i]^2)+(9.184E-04*T[i])+3.788E-01
k43:=-(1.970E-06*T[i]^2)+(8.980E-04*T[i])+3.753E-01
k44:=-(1.996E-06*T[i]^2)+(8.784E-04*T[i])+3.719E-01
k45:=-(1.996E-06*T[i]^2)+(8.584E-04*T[i])+3.685E-01
k46:=-(1.913E-06*T[i]^2)+(8.415E-04*T[i])+3.652E-01
k47:=-(1.879E-06*T[i]^2)+(8.225E-04*T[i])+3.619E-01
k48:=-(1.727E-06*T[i]^2)+(8.064E-04*T[i])+3.586E-01
k49:=-(1.835E-06*T[i]^2)+(7.870E-04*T[i])+3.553E-01
k50:=-(1.684E-06*T[i]^2)+(7.702E-04*T[i])+3.521E-01
IF (volp>30) AND (volp<=31) then kc:=((volp-30)/1)*(k31-k30)+k30 ELSE
IF (volp>31) AND (volp<=32) then kc:=((volp-31)/1)*(k32-k31)+k31 ELSE
IF (volp>32) AND (volp<=33) then kc:=((volp-32)/1)*(k33-k32)+k32 ELSE
IF (volp>33) AND (volp<=34) then kc:=((volp-33)/1)*(k34-k33)+k33 ELSE
IF (volp>34) AND (volp<=35) then kc:=((volp-34)/1)*(k35-k34)+k34 ELSE
IF (volp>35) AND (volp<=36) then kc:=((volp-35)/1)*(k36-k35)+k35 ELSE
IF (volp>36) AND (volp<=37) then kc:=((volp-36)/1)*(k37-k36)+k36 ELSE
IF (volp>37) AND (volp<=38) then kc:=((volp-37)/1)*(k38-k37)+k37 ELSE
IF (volp>38) AND (volp<=39) then kc:=((volp-38)/1)*(k39-k38)+k38 ELSE
IF (volp>39) AND (volp<=40) then kc:=((volp-39)/1)*(k40-k39)+k39 ELSE
IF (volp>40) AND (volp<=41) then kc:=((volp-40)/1)*(k41-k40)+k40 ELSE
IF (volp>41) AND (volp<=42) then kc:=((volp-41)/1)*(k42-k41)+k41 ELSE
IF (volp>42) AND (volp<=43) then kc:=((volp-42)/1)*(k43-k42)+k42 ELSE
IF (volp>43) AND (volp<=44) then kc:=((volp-43)/1)*(k44-k43)+k43 ELSE
IF (volp>44) AND (volp<=45) then kc:=((volp-44)/1)*(k45-k44)+k44 ELSE
IF (volp>45) AND (volp<=46) then kc:=((volp-45)/1)*(k46-k45)+k45 ELSE
IF (volp>46) AND (volp<=47) then kc:=((volp-46)/1)*(k47-k46)+k46 ELSE
IF (volp>47) AND (volp<=48) then kc:=((volp-47)/1)*(k48-k47)+k47 ELSE
IF (volp>48) AND (volp<=49) then kc:=((volp-48)/1)*(k49-k48)+k48 ELSE
IF (volp>49) AND (volp<=50) then kc:=((volp-49)/1)*(k50-k49)+k49
ENDIF
ENDIF
ENDIF
ENDIF
ENDIF
ENDIF
ENDIF
ENDIF
ENDIF
ENDIF
ENDIF
ENDIF
ENDIF
ENDIF
ENDIF
ENDIF
ENDIF
ENDIF
ENDIF
END

FUNCTION cpc(z, i, T[1..z], volp)
cp30:=(2.88546*T[i])+3571.0910
cp31:=(2.95273*T[i])+3551.909
cp32:=(3.0000*T[i])+3533.0000
cp33:=(3.0527*T[i])+3513.3640
cp34:=(3.1145*T[i])+3493.9090
cp35:=(3.1667*T[i])+3474.3889
cp36:=(3.2233*T[i])+3454.8944
cp37:=(3.2700*T[i])+3435.0167
cp38:=(3.3200*T[i])+3415.1556
cp39:=(3.3667*T[i])+3395.2778
cp40:=(3.4233*T[i])+3375.3389
```

```
cp41:=(3.4767*T[i])+3355.1611
cp42:=(3.5300*T[i])+3334.9833
cp43:=(3.5767*T[i])+3314.6611
cp44:=(3.6467*T[i])+3294.2333
cp45:=(3.7000*T[i])+3273.7222
cp46:=(3.7533*T[i])+3253.1000
cp47:=(3.7867*T[i])+3232.0444
cp48:=(3.8467*T[i])+3211.5667
cp49:=(3.9000*T[i])+3190.7222
cp50:=(3.9533*T[i])+3169.7667
IF (volp>30) AND (volp<=31) then cpc:=((volp-30)/1)*(cp31-cp30)+cp30 ELSE
IF (volp>31) AND (volp<=32) then cpc:=((volp-31)/1)*(cp32-cp31)+cp31 ELSE
IF (volp>32) AND (volp<=33) then cpc:=((volp-32)/1)*(cp33-cp32)+cp32 ELSE
IF (volp>33) AND (volp<=34) then cpc:=((volp-33)/1)*(cp34-cp33)+cp33 ELSE
IF (volp>34) AND (volp<=35) then cpc:=((volp-34)/1)*(cp35-cp34)+cp34 ELSE
IF (volp>35) AND (volp<=36) then cpc:=((volp-35)/1)*(cp36-cp35)+cp35 ELSE
IF (volp>36) AND (volp<=37) then cpc:=((volp-36)/1)*(cp37-cp36)+cp36 ELSE
IF (volp>37) AND (volp<=38) then cpc:=((volp-37)/1)*(cp38-cp37)+cp37 ELSE
IF (volp>38) AND (volp<=39) then cpc:=((volp-38)/1)*(cp39-cp38)+cp38 ELSE
IF (volp>39) AND (volp<=40) then cpc:=((volp-39)/1)*(cp40-cp39)+cp39 ELSE
IF (volp>40) AND (volp<=41) then cpc:=((volp-40)/1)*(cp41-cp40)+cp40 ELSE
IF (volp>41) AND (volp<=42) then cpc:=((volp-41)/1)*(cp42-cp41)+cp41 ELSE
IF (volp>42) AND (volp<=43) then cpc:=((volp-42)/1)*(cp43-cp42)+cp42 ELSE
IF (volp>43) AND (volp<=44) then cpc:=((volp-43)/1)*(cp44-cp43)+cp43 ELSE
IF (volp>44) AND (volp<=45) then cpc:=((volp-44)/1)*(cp45-cp44)+cp44 ELSE
IF (volp>45) AND (volp<=46) then cpc:=((volp-45)/1)*(cp46-cp45)+cp45 ELSE
IF (volp>46) AND (volp<=47) then cpc:=((volp-46)/1)*(cp47-cp46)+cp46 ELSE
IF (volp>47) AND (volp<=48) then cpc:=((volp-47)/1)*(cp48-cp47)+cp47 ELSE
IF (volp>48) AND (volp<=49) then cpc:=((volp-48)/1)*(cp49-cp48)+cp48 ELSE
IF (volp>49) AND (volp<=50) then cpc:=((volp-49)/1)*(cp50-cp49)+cp49
ENDIF
ENDIF
ENDIF
ENDIF
ENDIF
ENDIF
ENDIF
ENDIF
ENDIF
ENDIF
ENDIF
ENDIF
ENDIF
ENDIF
ENDIF
ENDIF
ENDIF
ENDIF
ENDIF
ENDIF
ENDIF
END


{EXCHANGER INPUTS}
A_tube=Atot-A_fin
Dh=0.01022041          {m}                    {<--------- EXCHANGER VARIABLE}
A_fin=0.9207407                               {<--------- EXCHANGER VARIABLE}
Amin=0.0142867                                {<--------- EXCHANGER VARIABLE}
Atot=1.1361809
Lfin=0.2032            {8 inches}
Nfins=55
Ntubes=16
n1=8                   {passes per partition}
```

```
n2=8                    {passes per partition}
t_fin=.127e-3           {m}
frontal_area=0.02322576 {m^2}                          {<--------- EXCHANGER VARIABLE}
La=0.4572                                              {<--------- EXCHANGER VARIABLE}
Lb=0.5175                                              {<--------- EXCHANGER VARIABLE}
Lc=0.0508                                              {<--------- EXCHANGER VARIABLE}
Dout=0.009525           {0.375 inches}
Din=0.00800             {0.315 inches}
do=0.05334              {3.0" = .07620m & 2.1" = .05334m}  {<--------- ORIFICE PLATE BORE DIA.}

{SYSTEM INPUTS}
Pbar=738                {mmHg} {<-------------------INPUT: Barometric Pressure}
Tb=24.5                 {deg C}  {<-------------------INPUT: Barometer Temperature}
specgrav=1.069                 {<-------------------INPUT: Specific Gravity}
Tsg=-11.0                      {<-------------------INPUT: Mean Operating Temperature of coolant}
Tref=15.56                     {<-------------------INPUT: Hygrometer Calibration temperature}

{MEASURED DATA  IS STORED IN AN EES LOOKUP TABLE; THE INDICES REFER TO DIFFERENT INSTANCES IN TIME}
RTD_in[1]=AvgLookup('Data1','RTDin',1,121)                                  {inlet coolant temp, deg C}
RTD_out[1]=AvgLookup('Data1','RTDout',1,121)                                {outlet coolant temp, deg C}
mc[1]=AvgLookup('Data1','mc',1,121)                                         {coolant mass flow rate, kg/s}
T2[1]=AvgLookup('Data1','T2',1,121)                                         {upstream air temp, deg C}
T3[1]=AvgLookup('Data1','T3',1,121)                                         {upstream air temp, deg C}
T4[1]=AvgLookup('Data1','T4',1,121)                                         {upstream air temp, deg C}
T5[1]=AvgLookup('Data1','T5',1,121)                                         {upstream air temp, deg C}
T6[1]=AvgLookup('Data1','T6',1,121)                                         {upstream air temp, deg C}
T7[1]=AvgLookup('Data1','T7',1,121)                                         {upstream air temp, deg C}
Tup[1]=(1/6)*(T2[1]+T3[1]+T4[1]+T5[1]+T6[1]+T7[1])                          {AVG upstream air temp, deg C}
T10[1]=AvgLookup('Data1','T10',1,121)                                       {downstream air temp, deg C}
T11[1]=AvgLookup('Data1','T11',1,121)                                       {downstream air temp, deg C}
T12[1]=AvgLookup('Data1','T12',1,121)                                       {downstream air temp, deg C}
T13[1]=AvgLookup('Data1','T13',1,121)                                       {downstream air temp, deg C}
T14[1]=AvgLookup('Data1','T14',1,121)                                       {downstream air temp, deg C}
T15[1]=AvgLookup('Data1','T15',1,121)                                       {downstream air temp, deg C}
T16[1]=AvgLookup('Data1','T16',1,121)                                       {downstream air temp, deg C}
Tdown[1]=(1/7)*(T10[1]+T11[1]+T12[1]+T13[1]+T14[1]+T15[1]+T16[1])           {AVG downstream air temp, deg C}
T18[1]=AvgLookup('Data1','T18',1,121)                                       {temp @ the orifice plate, deg C}
Porifice[1]=AvgLookup('Data1','Orifice',1,121)*convert(inH2o,kPa)           {pressure drop across orifice plate, kPa}
Pcore[1]=AvgLookup('Data1','Core',1,121)*convert(inH2o,kPa)                 {core pressure drop, kPa}
RH_up[1]=AvgLookup('Data1','RHup',1,121)                                    {upstream relative humidity}
RH_down[1]=AvgLookup('Data1','RHdown',1,121)                                {downstream relative humidity}

RTD_in[2]=AvgLookup('Data1','RTDin',123,243)
RTD_out[2]=AvgLookup('Data1','RTDout',123,243)
mc[2]=AvgLookup('Data1','mc',123,243)
T2[2]=AvgLookup('Data1','T2',123,243)
T3[2]=AvgLookup('Data1','T3',123,243)
T4[2]=AvgLookup('Data1','T4',123,243)
T5[2]=AvgLookup('Data1','T5',123,243)
T6[2]=AvgLookup('Data1','T6',123,243)
T7[2]=AvgLookup('Data1','T7',123,243)
Tup[2]=(1/6)*(T2[2]+T3[2]+T4[2]+T5[2]+T6[2]+T7[2])
T10[2]=AvgLookup('Data1','T10',123,243)
T11[2]=AvgLookup('Data1','T11',123,243)
T12[2]=AvgLookup('Data1','T12',123,243)
T13[2]=AvgLookup('Data1','T13',123,243)
T14[2]=AvgLookup('Data1','T14',123,243)
T15[2]=AvgLookup('Data1','T15',123,243)
T16[2]=AvgLookup('Data1','T16',123,243)
Tdown[2]=(1/7)*(T10[2]+T11[2]+T12[2]+T13[2]+T14[2]+T15[2]+T16[2])
T18[2]=AvgLookup('Data1','T18',123,243)
```

```
Porifice[2]=AvgLookup('Data1','Orifice',123,243)*convert(inH2o,kPa)
Pcore[2]=AvgLookup('Data1','Core',123,243)*convert(inH2o,kPa)
RH_up[2]=AvgLookup('Data1','RHup',123,243)
RH_down[2]=AvgLookup('Data1','RHdown',123,243)

RTD_in[3]=AvgLookup('Data1','RTDin',245,365)
RTD_out[3]=AvgLookup('Data1','RTDout',245,365)
mc[3]=AvgLookup('Data1','mc',245,365)
T2[3]=AvgLookup('Data1','T2',245,365)
T3[3]=AvgLookup('Data1','T3',245,365)
T4[3]=AvgLookup('Data1','T4',245,365)
T5[3]=AvgLookup('Data1','T5',245,365)
T6[3]=AvgLookup('Data1','T6',245,365)
T7[3]=AvgLookup('Data1','T7',245,365)
Tup[3]=(1/6)*(T2[3]+T3[3]+T4[3]+T5[3]+T6[3]+T7[3])
T10[3]=AvgLookup('Data1','T10',245,365)
T11[3]=AvgLookup('Data1','T11',245,365)
T12[3]=AvgLookup('Data1','T12',245,365)
T13[3]=AvgLookup('Data1','T13',245,365)
T14[3]=AvgLookup('Data1','T14',245,365)
T15[3]=AvgLookup('Data1','T15',245,365)
T16[3]=AvgLookup('Data1','T16',245,365)
Tdown[3]=(1/7)*(T10[3]+T11[3]+T12[3]+T13[3]+T14[3]+T15[3]+T16[3])
T18[3]=AvgLookup('Data1','T18',245,365)
Porifice[3]=AvgLookup('Data1','Orifice',245,365)*convert(inH2o,kPa)
Pcore[3]=AvgLookup('Data1','Core',245,365)*convert(inH2o,kPa)
RH_up[3]=AvgLookup('Data1','RHup',245,365)
RH_down[3]=AvgLookup('Data1','RHdown',245,365)

RTD_in[4]=AvgLookup('Data1','RTDin',367,487)
RTD_out[4]=AvgLookup('Data1','RTDout',367,487)
mc[4]=AvgLookup('Data1','mc',367,487)
T2[4]=AvgLookup('Data1','T2',367,487)
T3[4]=AvgLookup('Data1','T3',367,487)
T4[4]=AvgLookup('Data1','T4',367,487)
T5[4]=AvgLookup('Data1','T5',367,487)
T6[4]=AvgLookup('Data1','T6',367,487)
T7[4]=AvgLookup('Data1','T7',367,487)
Tup[4]=(1/6)*(T2[4]+T3[4]+T4[4]+T5[4]+T6[4]+T7[4])
T10[4]=AvgLookup('Data1','T10',367,487)
T11[4]=AvgLookup('Data1','T11',367,487)
T12[4]=AvgLookup('Data1','T12',367,487)
T13[4]=AvgLookup('Data1','T13',367,487)
T14[4]=AvgLookup('Data1','T14',367,487)
T15[4]=AvgLookup('Data1','T15',367,487)
T16[4]=AvgLookup('Data1','T16',367,487)
Tdown[4]=(1/7)*(T10[4]+T11[4]+T12[4]+T13[4]+T14[4]+T15[4]+T16[4])
T18[4]=AvgLookup('Data1','T18',367,487)
Porifice[4]=AvgLookup('Data1','Orifice',367,487)*convert(inH2o,kPa)
Pcore[4]=AvgLookup('Data1','Core',367,487)*convert(inH2o,kPa)
RH_up[4]=AvgLookup('Data1','RHup',367,487)
RH_down[4]=AvgLookup('Data1','RHdown',367,487)

RTD_in[5]=AvgLookup('Data1','RTDin',489,609)
RTD_out[5]=AvgLookup('Data1','RTDout',489,609)
mc[5]=AvgLookup('Data1','mc',489,609)
T2[5]=AvgLookup('Data1','T2',489,609)
T3[5]=AvgLookup('Data1','T3',489,609)
T4[5]=AvgLookup('Data1','T4',489,609)
T5[5]=AvgLookup('Data1','T5',489,609)
T6[5]=AvgLookup('Data1','T6',489,609)
T7[5]=AvgLookup('Data1','T7',489,609)
```

```
Tup[5]=(1/6)*(T2[5]+T3[5]+T4[5]+T5[5]+T6[5]+T7[5])
T10[5]=AvgLookup('Data1','T10',489,609)
T11[5]=AvgLookup('Data1','T11',489,609)
T12[5]=AvgLookup('Data1','T12',489,609)
T13[5]=AvgLookup('Data1','T13',489,609)
T14[5]=AvgLookup('Data1','T14',489,609)
T15[5]=AvgLookup('Data1','T15',489,609)
T16[5]=AvgLookup('Data1','T16',489,609)
Tdown[5]=(1/7)*(T10[5]+T11[5]+T12[5]+T13[5]+T14[5]+T15[5]+T16[5])
T18[5]=AvgLookup('Data1','T18',489,609)
Porifice[5]=AvgLookup('Data1','Orifice',489,609)*convert(inH2o,kPa)
Pcore[5]=AvgLookup('Data1','Core',489,609)*convert(inH2o,kPa)
RH_up[5]=AvgLookup('Data1','RHup',489,609)
RH_down[5]=AvgLookup('Data1','RHdown',489,609)

RTD_in[6]=AvgLookup('Data1','RTDin',611,731)
RTD_out[6]=AvgLookup('Data1','RTDout',611,731)
mc[6]=AvgLookup('Data1','mc',611,731)
T2[6]=AvgLookup('Data1','T2',611,731)
T3[6]=AvgLookup('Data1','T3',611,731)
T4[6]=AvgLookup('Data1','T4',611,731)
T5[6]=AvgLookup('Data1','T5',611,731)
T6[6]=AvgLookup('Data1','T6',611,731)
T7[6]=AvgLookup('Data1','T7',611,731)
Tup[6]=(1/6)*(T2[6]+T3[6]+T4[6]+T5[6]+T6[6]+T7[6])
T10[6]=AvgLookup('Data1','T10',611,731)
T11[6]=AvgLookup('Data1','T11',611,731)
T12[6]=AvgLookup('Data1','T12',611,731)
T13[6]=AvgLookup('Data1','T13',611,731)
T14[6]=AvgLookup('Data1','T14',611,731)
T15[6]=AvgLookup('Data1','T15',611,731)
T16[6]=AvgLookup('Data1','T16',611,731)
Tdown[6]=(1/7)*(T10[6]+T11[6]+T12[6]+T13[6]+T14[6]+T15[6]+T16[6])
T18[6]=AvgLookup('Data1','T18',611,731)
Porifice[6]=AvgLookup('Data1','Orifice',611,731)*convert(inH2o,kPa)
Pcore[6]=AvgLookup('Data1','Core',611,731)*convert(inH2o,kPa)
RH_up[6]=AvgLookup('Data1','RHup',611,731)
RH_down[6]=AvgLookup('Data1','RHdown',611,731)

RTD_in[7]=AvgLookup('Data1','RTDin',733,853)
RTD_out[7]=AvgLookup('Data1','RTDout',733,853)
mc[7]=AvgLookup('Data1','mc',733,853)
T2[7]=AvgLookup('Data1','T2',733,853)
T3[7]=AvgLookup('Data1','T3',733,853)
T4[7]=AvgLookup('Data1','T4',733,853)
T5[7]=AvgLookup('Data1','T5',733,853)
T6[7]=AvgLookup('Data1','T6',733,853)
T7[7]=AvgLookup('Data1','T7',733,853)
Tup[7]=(1/6)*(T2[7]+T3[7]+T4[7]+T5[7]+T6[7]+T7[7])
T10[7]=AvgLookup('Data1','T10',733,853)
T11[7]=AvgLookup('Data1','T11',733,853)
T12[7]=AvgLookup('Data1','T12',733,853)
T13[7]=AvgLookup('Data1','T13',733,853)
T14[7]=AvgLookup('Data1','T14',733,853)
T15[7]=AvgLookup('Data1','T15',733,853)
T16[7]=AvgLookup('Data1','T16',733,853)
Tdown[7]=(1/7)*(T10[7]+T11[7]+T12[7]+T13[7]+T14[7]+T15[7]+T16[7])
T18[7]=AvgLookup('Data1','T18',733,853)
Porifice[7]=AvgLookup('Data1','Orifice',733,853)*convert(inH2o,kPa)
Pcore[7]=AvgLookup('Data1','Core',733,853)*convert(inH2o,kPa)
RH_up[7]=AvgLookup('Data1','RHup',733,853)
RH_down[7]=AvgLookup('Data1','RHdown',733,853)
```

```
RTD_in[8]=AvgLookup('Data1','RTDin',855,975)
RTD_out[8]=AvgLookup('Data1','RTDout',855,975)
mc[8]=AvgLookup('Data1','mc',855,975)
T2[8]=AvgLookup('Data1','T2',855,975)
T3[8]=AvgLookup('Data1','T3',855,975)
T4[8]=AvgLookup('Data1','T4',855,975)
T5[8]=AvgLookup('Data1','T5',855,975)
T6[8]=AvgLookup('Data1','T6',855,975)
T7[8]=AvgLookup('Data1','T7',855,975)
Tup[8]=(1/6)*(T2[8]+T3[8]+T4[8]+T5[8]+T6[8]+T7[8])
T10[8]=AvgLookup('Data1','T10',855,975)
T11[8]=AvgLookup('Data1','T11',855,975)
T12[8]=AvgLookup('Data1','T12',855,975)
T13[8]=AvgLookup('Data1','T13',855,975)
T14[8]=AvgLookup('Data1','T14',855,975)
T15[8]=AvgLookup('Data1','T15',855,975)
T16[8]=AvgLookup('Data1','T16',855,975)
Tdown[8]=(1/7)*(T10[8]+T11[8]+T12[8]+T13[8]+T14[8]+T15[8]+T16[8])
T18[8]=AvgLookup('Data1','T18',855,975)
Porifice[8]=AvgLookup('Data1','Orifice',855,975)*convert(inH2o,kPa)
Pcore[8]=AvgLookup('Data1','Core',855,975)*convert(inH2o,kPa)
RH_up[8]=AvgLookup('Data1','RHup',855,975)
RH_down[8]=AvgLookup('Data1','RHdown',855,975)

RTD_in[9]=AvgLookup('Data1','RTDin',977,1097)
RTD_out[9]=AvgLookup('Data1','RTDout',977,1097)
mc[9]=AvgLookup('Data1','mc',977,1097)
T2[9]=AvgLookup('Data1','T2',977,1097)
T3[9]=AvgLookup('Data1','T3',977,1097)
T4[9]=AvgLookup('Data1','T4',977,1097)
T5[9]=AvgLookup('Data1','T5',977,1097)
T6[9]=AvgLookup('Data1','T6',977,1097)
T7[9]=AvgLookup('Data1','T7',977,1097)
Tup[9]=(1/6)*(T2[9]+T3[9]+T4[9]+T5[9]+T6[9]+T7[9])
T10[9]=AvgLookup('Data1','T10',977,1097)
T11[9]=AvgLookup('Data1','T11',977,1097)
T12[9]=AvgLookup('Data1','T12',977,1097)
T13[9]=AvgLookup('Data1','T13',977,1097)
T14[9]=AvgLookup('Data1','T14',977,1097)
T15[9]=AvgLookup('Data1','T15',977,1097)
T16[9]=AvgLookup('Data1','T16',977,1097)
Tdown[9]=(1/7)*(T10[9]+T11[9]+T12[9]+T13[9]+T14[9]+T15[9]+T16[9])
T18[9]=AvgLookup('Data1','T18',977,1097)
Porifice[9]=AvgLookup('Data1','Orifice',977,1097)*convert(inH2o,kPa)
Pcore[9]=AvgLookup('Data1','Core',977,1097)*convert(inH2o,kPa)
RH_up[9]=AvgLookup('Data1','RHup',977,1097)
RH_down[9]=AvgLookup('Data1','RHdown',977,1097)

RTD_in[10]=AvgLookup('Data1','RTDin',1099,1219)
RTD_out[10]=AvgLookup('Data1','RTDout',1099,1219)
mc[10]=AvgLookup('Data1','mc',1099,1219)
T2[10]=AvgLookup('Data1','T2',1099,1219)
T3[10]=AvgLookup('Data1','T3',1099,1219)
T4[10]=AvgLookup('Data1','T4',1099,1219)
T5[10]=AvgLookup('Data1','T5',1099,1219)
T6[10]=AvgLookup('Data1','T6',1099,1219)
T7[10]=AvgLookup('Data1','T7',1099,1219)
Tup[10]=(1/6)*(T2[10]+T3[10]+T4[10]+T5[10]+T6[10]+T7[10])
T10[10]=AvgLookup('Data1','T10',1099,1219)
T11[10]=AvgLookup('Data1','T11',1099,1219)
T12[10]=AvgLookup('Data1','T12',1099,1219)
```

```
T13[10]=AvgLookup('Data1','T13',1099,1219)
T14[10]=AvgLookup('Data1','T14',1099,1219)
T15[10]=AvgLookup('Data1','T15',1099,1219)
T16[10]=AvgLookup('Data1','T16',1099,1219)
Tdown[10]=(1/7)*(T10[10]+T11[10]+T12[10]+T13[10]+T14[10]+T15[10]+T16[10])
T18[10]=AvgLookup('Data1','T18',1099,1219)
Porifice[10]=AvgLookup('Data1','Orifice',1099,1219)*convert(inH2o,kPa)
Pcore[10]=AvgLookup('Data1','Core',1099,1219)*convert(inH2o,kPa)
RH_up[10]=AvgLookup('Data1','RHup',1099,1219)
RH_down[10]=AvgLookup('Data1','RHdown',1099,1219)

{======================PROGRAM CONSTANTS==============================}

{==============Calculation of DOWTHERM4000 Concentration=============}
rhoH2O=DENSITY(Steam,T=Tref,P=Patm)
rhoH2O=(1/specgrav)*rhoRTD(Tref,volp)
wgtp=(0.9997082*volp)+2.2537408

{=============Calculation of Barometric Pressure w/ Corrections=============}
Ptemp=(((1+0.0000184*Tb)/(1+0.0001818*Tb))-1)*(Pbar)+Pbar
Pgrav=(-0.000508)*Ptemp+Ptemp
Psea=Pgrav+19.03
Patm=Psea*convert(mmHg,kPa)
Pair2=Patm
Dpvc=0.15875                          {m}
d1=Dpvc                               {m}
beta=do/d1
Ao=pi*(1/4)*((do)^2)

{================Ablimation Program Constants=========================}
Rgas=0.4615199                        {specific gas constant for water, kJ/kg/K}
a0=0.199798E4
a1=0.18035706E1
a2=0.36400463E-3
a3=-0.14677622E-5
a4=0.28726608E-8
a5=-0.17508262E-11
b0=-0.647595E3
b1=0.274292
b2=0.2910583E-2
b3=0.1083437E-5
b4=0.107E-5
{=============================================================================}

{ITERATIVE EQUATIONS}
Z=9
Dab=0.00002185          {binary diffusion coefficient of water into air, m^2/sec}
Tfrost[1]=-6.30         {The frost surface temperature is found by iteration. The temperature is}
Tfrost[2]=-5.50         {determined below in the FROST RESISTANCE subroutine by changing this}
Tfrost[3]=-4.80         {temp until WaS = WaS2. In this way, the log-mean humidity ratio driving}
Tfrost[4]=-4.6          {potential satisfies the heat-and-mass transfer analogy.}
Tfrost[5]=-4.3
Tfrost[6]=-3.85
Tfrost[7]=-3.6
Tfrost[8]=-3.1
Tfrost[9]=-3.05
eta_f=1.0               {The fin efficiency is assumed here to be unity for convenience. A subroutine}
R_contact=0             {based on the sector method, however, is attached at the end of this program.}



Duplicate i=1,Z
```

```
{==================Ablimation Energy Calculation Subroutine=====================}

tube_mean[i]=0.5*(Tavg[i]+RTD_avg[i])
Ttube[i]=tube_mean[i]+273.15
b_prime[i]=(0.70E-8)-((0.147184E-8)*EXP(1734.29/Ttube[i]))
c_prime[i]=(0.104E-14)-((0.335297E-17)*EXP(3645.09/Ttube[i]))
d_b_prime[i]=(0.147184E-8)*(1734.29/(Ttube[i]^2))*(EXP(1734.29/Ttube[i]))
pice[i]=(0.66136)*(EXP(0.09575*tube_mean[i]))*1000 {saturation pressure of the vapor over the ice surface}

hg[i]=((a0)+(a1*Ttube[i])+(a2*(Ttube[i]^2))+(a3*(Ttube[i]^3))+(a4*(Ttube[i]^4))+(a5*(Ttube[i]^5))-
(Rgas*(Ttube[i]^2)*d_b_prime[i]*pice[i]))*1000
hi[i]=(b0+(b1*Ttube[i])+(b2*(Ttube[i]^2))+(b3*(Ttube[i]^3))+(b4*pice[i]))*1000
hfrost[i]=hg[i]-hi[i]                          {latent heat of ablimation, J/kg}
{hfrost=2833000}                               {typical latent heat of ablimation, J/kg}

{====================Coolant Input Parameters================================}
RTD_avg[i]=(RTD_in[i]+RTD_out[i])/2            {deg C}
T[i]=RTD_avg[i]
Tm[i]=tube_mean[i]
nuc[i]=visc(z, i, T[1..z], volp)               {Pa-s}
rhoc[i]=rhoc(z, i, T[1..z], volp)              {kg/m^3}
cpc[i]=cpc(z, i, T[1..z], volp)                {J/kg-C}
kc[i]=kc(z, i, T[1..z], volp)                  {W/(m-K)}
nuw[i]=nuw(z, i, Tm[1..z], volp)               {Evaluated @ tube mean temp}
ReD[i]=(4*mc[i])/(Din*pi*nuc[i])
Pr[i]=(cpc[i]*nuc[i])/kc[i]


{Air Flow Parameters}
cpa[i]=CP(AirH2O,T=Tavg[i],P=Pair1[i],R=RH[i])*1000
Tavg[i]=(Tup[i]+Tdown[i])/2
Pair1[i]=Patm+Pcore[i]
RH[i]=0.5*(RH_up[i]+RH_down[i])

rhoaO[i]=DENSITY(AirH2O,T=T18[i],P=Pair2,R=RH_down[i])      {using EES}
rhoaO2[i]=((Pair2*1000)/(287*converttemp('C','K',T18[i])))  {using IDEAL GAS}
nuaO[i]=VISCOSITY(AirH2O,T=T18[i],P=Pair2,R=RH_down[i])
rhoaD[i]=DENSITY(AirH2O,T=Tdown[i],P=Pair2,R=RH_down[i])
nuaD[i]=VISCOSITY(AirH2O,T=Tdown[i],P=Pair2,R=RH_down[i])
rhoaU[i]=DENSITY(AirH2O,T=Tup[i],P=Pair1[i],R=RH_up[i])
nuaU[i]=VISCOSITY(AirH2O,T=Tup[i],P=Pair1[i],R=RH_up[i])
rhoaAVG[i]=DENSITY(AirH2O,T=Tavg[i],P=Pair1[i],R=RH[i])
WaU[i]=HUMRAT(AirH2O,T=Tup[i],P=Pair1[i],R=RH_up[i])
WaD[i]=HUMRAT(AirH2O,T=Tdown[i],P=Pair2,R=RH_down[i])
mwU[i]=WaU[i]/(1+WaU[i])                       {convert humidity ratio to mass fraction}
mwD[i]=WaD[i]/(1+WaD[i])                       {convert humidity ratio to mass fraction}
mfrost[i]=ma[i]*(mwU[i]-mwD[i])                {frost disposition rate on heat exhanger}


{=============================================================================}
{DATA REDUCTION CALCULATIONS}
{Air Flow Calculations}
face_vel[i]=ma[i]/(rhoaU[i]*frontal_area)
Vmax[i]=ma[i]/(rhoaAVG[i]*Amin[i])
Re[i]=(4*ma[i])/(Dpvc*pi*nuaO[i])
Redh[i]=(Vmax[i]*Dh[i]*rhoaU[i])/(nuaU[i])
CE[i]=(1/((1-beta^4)^0.5))*(0.5959+(0.0312*beta^2.1)-(0.184*beta^8)+((2.286*beta^4)/(1000*d1*(1-beta^4)))-
((0.8560*beta^3)/(1000*d1))+(91.71*(beta^2.5)*(Re[i]^(-0.75))))
vol_air[i]=CE[i]*Ao*(((2*Porifice[i]*1000)/rhoaO[i])^(0.5))
ma[i]=vol_air[i]*rhoaO[i]
{Energy Balance Calculations}
```

```
Qc[i]=mc[i]*cpc[i]*(RTD_out[i]-RTD_in[i])
ha1[i]=ENTHALPY(AirH2O,T=Tup[i],P=Pair1[i],R=RH_up[i])
ha2[i]=ENTHALPY(AirH2O,T=Tdown[i],P=Pair2,R=RH_down[i])
Qa[i]=ma[i]*cpa[i]*(Tup[i]-Tdown[i])+(mfrost[i]*hfrost[i])
Qa2[i]=(ma[i]*(ha1[i]-ha2[i])*1000)
energy_bal[i]=(abs(Average(Qc[i],Qa[i])-Qc[i])/(Average(Qc[i],Qa[i])))

{Heat Transfer Calculations}
hai[i]=ENTHALPY(AirH2O,T=Tup[i],P=Pair1[i],R=RH_up[i])
hasat[i]=ENTHALPY(AirH2O,T=Tri[i],P=Pair2,R=1)
ham[i]=ENTHALPY(AirH2O,T=Trm2[i],P=Pair1[i],R=1)

Tao1b[i]=TEMPERATURE(AirH2O,h=hao1[i],P=Pair2,R=RH_down[i])
Tao2b[i]=TEMPERATURE(AirH2O,h=hao2[i],P=Pair2,R=RH_down[i])

q1b[i]=ma[i]*(hai[i]-hao1[i])*1000
q1b[i]=Cr[i]*(Trm2[i]-Tri[i])
q2b[i]=ma[i]*(hai[i]-hao2[i])*1000
q2b[i]=Cr[i]*(Tro[i]-Trm2[i])
Ca[i]=ma[i]*cpa[i]
Cr[i]=mc[i]*cpc[i]
Tri[i]=RTD_in[i]
Tro[i]=RTD_out[i]
Ca[i]=Ca1b[i]+Ca2b[i]
q1b[i]=eta1b[i]*ma[i]*(hai[i]-hasat[i])*1000
q2b[i]=eta2b[i]*ma[i]*(hai[i]-ham[i])*1000

Rc1b[i]=Ca1b[i]/Cr[i]
eta1b[i]=((((1-etap1b[i]*Rc1b[i])/(1-etap1b[i]))^(n1))-1)/(((((1-etap1b[i]*Rc1b[i])/(1-etap1b[i]))^(n1))-Rc1b[i])
etap1b[i]=(1-EXP(-G1b[i]*Rc1b[i]))/Rc1b[i]
NTUp1b[i]=-LN(1-G1b[i])

Rc2b[i]=Ca2b[i]/Cr[i]
eta2b[i]=(1-((1-(etap2b[i]*(1+Rc2b[i])))^(n2)))/(1+Rc2b[i])
etap2b[i]=(1-EXP(-G2b[i]*Rc2b[i]))/Rc2b[i]
NTUp2b[i]=-LN(1-G2b[i])

NTUp1b[i]=NTUp2b[i]
NTUp1b[i]=(UApb[i]/Ca1b[i])
NTUp2b[i]=(UApb[i]/Ca2b[i])
UAtot[i]=Ntubes*UApb[i]

NuR_gnielinski[i]=((f[i]/8)*(ReD[i]-1000)*Pr[i])/(1+12.7*((f[i]/8)^.5)*((Pr[i]^(2/3))-1))
{Gnielinski correlation, p. 445 DeWitt (Uses Darcy factor)}
{For  Re > 2300  AND  0.5 < Pr < 2000 }

f[i]=(1/((1.5635*LN(ReD[i]/7))^2))*(4)
{Colebrook correlation; within 1% of PKN}
{For Re  > 4000}

{Other Friction Factor Correlations}
{f2[i]=1/((0.79*LN(ReD[i])-1.64)^2)}
{Petukhov or Filonenko correlation; p. 424 DeWitt}
{For Re  > 3000-10000; within 1.8% of PKN}
{f3[i]=(0.00128+0.1143*(ReD[i]^(-0.311)))*(4)}
{Kakac, Shah, & Aung correlation; within +1.2% and -2% of PKN}
{For Re  >  4000}

x[i]=1/NuR_gnielinski[i]
y[i]=1/UAtot[i]
END
{=============================================================================}
```

```
{FROST RESISTANCE}
{Dab=(1.97E-5)*(1/P)*((T/256)^1.685)}        {Appendix A, p.947 Mills}
{Dab=1.87E-10*((T^2.072)/P)}                 {Marrero & Mason, 1972}
{Dab=0.00002185}                             {typical binary diffusion coefficient of water into air, m^2/s}

Duplicate o=1,Z
Le[o]=ka[o]/(rhoa[o]*cpa[o]*Dab)
mfrost[o]=((heff[o]/cpa[o])*AT[o]*((Le[o])^(-2/3))*deltaW[o])
deltaW[o]=((WaU[o]-WaS[o])-(WaD[o]-WaS[o]))/(ln((WaU[o]-WaS[o])/(WaD[o]-WaS[o])))
WaS2[o]=HUMRAT(AirH2O,T=Tfrost[o],P=Pair1[o],R=1)
{used iteratively to determine Tfrost by forcing WaS2[o] = WaS[o]}
WaDIFF[o]=WaS2[o]-WaS[o]
WaERROR[o]=(WaDIFF[o]/WaS[o])*100
{measures the rel. % error in the extracted Tfrost temperature}
rho_frost[o]=650*EXP(0.277*Tfrost[o])                                   {Hayashi, 1977}
rho_frostavg[o]=mfrost_total[o]/(frost_thick[o]*Atot)
k_frost[o]=0.132+((3.13E-4)*rho_frostavg[o])+((1.6E-7)*(rho_frostavg[o]^2))        {Lee et al., 1997}

END

mfrost_total[0]=0.16969     {<------- INPUT: Total Frost Deposition (kg) after the initial 30min grow period}
frost_thick[0]=0.001666     {<------- INPUT: Frost Thickness (m) after the initial 30 min grow period}
time=7*60
Duplicate i=1,Z
frost_thick[i]=((mfrost[i]/(AT[i]*rho_frost[i]))*time)+frost_thick[i-1]
mfrost_total[i]=(mfrost[i]*time)+mfrost_total[i-1]
END

Duplicate o=1,Z
Rf_fin[o]=(frost_thick[o])/(k_frost[o]*A_fin[o])
Rf_tube[o]= (LN((frost_thick[o]+(Dout/2))/(Dout/2)))/(2*pi*La*Ntubes*k_frost[o])
R_frost2[o]=1/((1/Rf_fin[o])+(1/Rf_tube[o]))
Rf_percent[o]=R_frost2[o]/(1/UAtot[o])

Amin[o]=(Lc*La)-(2*Dout*La)-(Nfins*(t_fin+2*frost_thick[o])*(Lc-2*Dout-4*frost_thick[0]))
{The last two terms subtracted from Lc represent the sum of 2 tube diameters and the total initial frost thickness
present on the tubes after 30min of growth.}
{These terms are subtracted to avoid "double counting" those areas already occupied by the frost layer “growing”
numerically in time off of the fin surface.}
A_tube[o]=pi*(Dout+2*frost_thick[o])*(La-(Nfins*t_fin))*Ntubes
A_fin[o]=2*Nfins*((Lc*Lfin)-(16*pi*(Dout/2)^2)-(16*0.00508*0.007874)-(0.018*0.00335)+ (Lc*(2*frost_thick[o] +t_fin)))
{The constant terms subtracted here account for the geometry and shape of the fin at the leading edge.}
AT[o]=A_fin[o]+A_tube[o]
Dh[o]=(4*Amin[o]*Lfin)/AT[o]
END

{=============================================================================}
{Chi-Squared Regression Analysis}
{EQUATION FORM:  y = k0 + k1*x}
v=1
S=5
wgt=1.1
min_energy=MIN(energy_bal[v..S])
max_energy=MAX(energy_bal[v..S])
wgtfactor[1]=1-(wgt*energy_bal[1])
wgtfactor[2]=1-(wgt*energy_bal[2])
wgtfactor[3]=1-(wgt*energy_bal[3])
wgtfactor[4]=1-(wgt*energy_bal[4])
wgtfactor[5]=1-(wgt*energy_bal[5])
wgtfactor[6]=1-(wgt*energy_bal[6])
wgtfactor[7]=1-(wgt*energy_bal[7])
wgtfactor[8]=1-(wgt*energy_bal[8])
```

```
wgtfactor[9]=1-(wgt*energy_bal[9])

{Weight-Averaged Regression Analysis}
K0_numer=(sum((x[i]*(wgtfactor[i])),i=v,S))*(sum((x[i]*(wgtfactor[i])*y[i]),i=v,S))-
(sum((x[i]*x[i]*(wgtfactor[i])),i=v,S))*(sum(((wgtfactor[i])*y[i]),i=v,S))
K1_numer=(sum((x[i]*(wgtfactor[i])),i=v,S))*(sum((y[i]*(wgtfactor[i])),i=v,S))-((S-
v+1)*(sum((x[i]*y[i]*(wgtfactor[i])*(wgtfactor[i])),i=v,S)))
Kdenom=((sum((x[i]*(wgtfactor[i])),i=v,S))^2)-((S-v+1)*(sum((x[i]*x[i]*(wgtfactor[i])*(wgtfactor[i])),i=v,S)))
K0=K0_numer/Kdenom
K1=K1_numer/Kdenom

{Linear Regression Analysis}
C0_numer=((sum(x[i],i=v,S))*(sum((x[i]*y[i]),i=v,S))-(sum((x[i]*x[i]),i=v,S))*(sum(y[i],i=v,S)))
C1_numer=(sum(x[i],i=v,S))*(sum(y[i],i=v,S))-((S-v+1)*(sum((x[i]*y[i]),i=v,S)))
Cdenom=(((sum(x[i],i=v,S))^2)-((S-v+1)*(sum((x[i]*x[i]),i=v,S))))
C0=C0_numer/Cdenom
C1=C1_numer/Cdenom

{=============================================================================}
{Thermal Resistances}
{Brazed Evaporator}
Duplicate o=1,Z                                  {NOTE: Reference ARI Standard 410}
R_fin[o]=1/(eta_f*heff[o]*A_fin[o])
R_tube[o]=1/(A_tube[o]*heff[o])
R_as[o]=(1/((1/(R_fin[o]))+(1/R_tube[o])))

R_frost[o]=1/((1/(Rf_fin[o]+R_contact))+(1/Rf_tube[o]))
RasTOTAL[o]=R_as[o]+R_frost[o]
(Rwall_cond[o]+R_as[o]+R_frost[o])=C0            {<------------------C0 =  Wilson Plot  y-intercept}
NuR[o]=(C1*(1/Rr_conv[o]))                       {<------------------C1 =  Wilson Plot  slope}

Rtot1[o]=(Rr_conv[o]+Rwall_cond[o]+R_frost[o]+R_as[o])
Rtot2[o]=1/(UAtot[o])
Rtot1[o]=Rtot2[o]

kalum[o]=k_('Aluminum', tube_mean[o])                              {W/m-K}
Rwall_cond[o]= (LN(Dout/Din))/(2*pi*Lb*Ntubes*kalum[o])

Stanton_no[o]=(heff[o]/(G[o]*cpa[o]))
sigma[o]=Amin[o]/(frontal_area)
G[o]=ma[o]/Amin[o]
Pr_air[o]=(cpa[o]*nua[o])/ka[o]
nua[o]=VISCOSITY(AirH2O,T=Tavg[o],P=Pair1[o],R=RH[o])
ka[o]=CONDUCTIVITY(AirH2O,T=Tavg[o],P=Pair1[o],R=RH[o])
rhoa[o]=DENSITY(AirH2O,T=Tavg[o],P=Pair1[o],R=RH[o])
j[o]=Stanton_no[o]*(Pr_air[o]^(2/3))

ff[o]=(((2*Pcore[o]*1000*rhoa[o])/(G[o]^2))*(Amin[o]/AT[o]))-((1+sigma[o]^2)*((rhoaU[o]/rhoaD[o])-
1)*(Amin[o]/AT[o])*(rhoa[o]/rhoaU[o]))

entrance_effect[o]=((1+sigma[o]^2)*((rhoaU[o]/rhoaD[o])-1)*(Amin[o]/AT[o])*(rhoa[o]/rhoaU[o]))

{Performance Evaluation Criteria}
hr1[o]=ENTHALPY(AirH2O,T=Tri[o],P=Pair1[o],R=1)
hr2[o]=ENTHALPY(AirH2O,T=Tro[o],P=Pair2,R=1)
hlm[o]=((hai[o]-hr2[o])-(hao2[o]-hr1[o]))/LN((hai[o]-hr2[o])/(hao2[o]-hr1[o]))
London_Area[o]=j[o]/ff[o]
PEC[o]=Qa[o]/(vol_air[o]*Pcore[o]*1000)
PEC2[o]=Qa[o]/(frontal_area*Lfin*hlm[o]*1000)
pumppower[o]=(vol_air[o]*Pcore[o])*1000
{Emery & Siegel, 1990}
dw[o]=WaD[o]-WaS[o]
```

```
h_ratio[o]=1.00-(1.118E3)*dw[o]+(8.14E5*dw[o]^2)-(2.11E8*dw[o]^3)
p_ratio[o]=1.00+10.24*(mfrost_total[o]/AT[o])+79.55*(mfrost_total[o]/AT[o])^2

END


{=============================================================================}
{Fin Efficiency Calculations}
{Exact soln for eta_f (circular) by Kern and Kraus '72, ARI-410; see Hong & Webb '96}
{
ri=Dout/2                                                    {tube radius}
kalum=k_('Aluminum', tube_mean[o])                           {W/m-K}
m^2=(2*heff/(kalum*t_fin))
N=12                                                         {# of sectors per zone}
L=.0254/2                                                    {Sectors w/ const L edge}
W=.0254/2                                                    {Sectors w/ const W edge}
{--Sector Method--}
Duplicate j=1,N
ro[j]=W*((((2*j-1)/(2*N))^2)*((L/W)^2)+1)^.5                 {For const L edge zones}
S[j]=.5*(ro[j]^2-ri^2)*(arctan(j*L/(N*W))-arctan((j-1)*L/(N*W)))   {For const L edge zones}
NUMER[j]=bessel_k1(m*ri)*bessel_i1(m*ro[j])-bessel_i1(m*ri)*bessel_k1(m*ro[j])
DENOM[j]=bessel_k0(m*ri)*bessel_i1(m*ro[j])+bessel_i0(m*ri)*bessel_k1(m*ro[j])
eta_fin[j]=(2*ri/(m*(ro[j]^2-ri^2)))*(NUMER[j]/DENOM[j])
End

{--Summation of Sectors--}
S1to6=sum(S[j],j=1,6)
S_sum=sum(S[j],j=1,N)
eta_f=(6*(sum(eta_fin[j]*S[j],j=1,N))+2*(sum(eta_fin[j]*S[j],j=7,N)))/((8*S_sum)-(2*S1to6))
}
{=============================================================================}
{                                                            }
{               END OF PROGRAM                               }
{                                                            }
```